MITOCHONDRIAL DYNAMICS AND OPTICAL CONFORMATION CHANGES IN DSRED AS STUDIED BY FOURIER IMAGING CORRELATION SPECTROSCOPY

by

ERIC NICOLAS SENNING

A DISSERTATION

Presented to the Department of Chemistry
and the Graduate School of the University of Oregon
in partial fulfillment of the requirements
for the degree of
Doctor of Philosophy

September 2009

University of Oregon Graduate School

Confirmation of Approval and Acceptance of Dissertation prepared by:

Eric Senning

Title:

"Mitochondrial Dynamics and Optical Conformation Changes in DsRed as Studied by Fourier Imaging Correlation Spectroscopy "

This dissertation has been accepted and approved in partial fulfillment of the requirements for the Doctor of Philosophy degree in the Department of Chemistry by:

Tom Stevens, Chairperson, Chemistry
Andrew Marcus, Advisor, Chemistry
Peter von Hippel, Member, Chemistry
Marina Guenza, Member, Chemistry
John Toner, Outside Member, Physics

and Richard Linton, Vice President for Research and Graduate Studies/Dean of the Graduate School for the University of Oregon.

September 5, 2009

Original approval signatures are on file with the Graduate School and the University of Oregon Libraries.

An Abstract of the Dissertation of

Eric Nicolas Senning for the degree of Doctor of Philosophy

in the Department of Chemistry to be taken September 2009

Title: MITOCHONDRIAL DYNAMICS AND OPTICAL CONFORMATION CHANGES IN DSRED AS STUDIED BY FOURIER IMAGING CORRELATION SPECTROSCOPY

Approved: _____
Dr. Andrew H. Marcus

Novel experiments that probe the dynamics of intracellular species, including the center-of-mass displacements and internal conformational transitions of biological macromolecules, have the potential to reveal the complex biochemical mechanisms operating within the cell. This work presents the implementation and development of Fourier imaging correlation spectroscopy (FICS), a phase-selective approach to fluorescence spectroscopy that measures the collective coordinate fluctuations of fluorescently labeled microscopic particles. In FICS experiments, a spatially modulated optical grating excites a fluorescently labeled sample. Phase-synchronous detection of the fluorescence, with respect to the phase of the exciting optical grating, can be used to monitor the fluctuations of partially averaged spatial coordinates. These data are then analyzed by two-point and four-point time correlation functions to provide a statistically

meaningful understanding of the dynamics under observation. FICS represents a unique route to elevate signal levels, while acquiring detailed information about molecular coordinate trajectories.

Mitochondria of mammalian cells are known to associate with cytoskeletal proteins, and their motions are affected by the stability of microtubules and microfilaments. Within the cell it is possible to fluorescently label the mitochondria and study its dynamic behavior with FICS. The dynamics of *S. cerevisiae* yeast mitochondria are characterized at four discrete length scales (ranging from $0.6 - 1.19\ \mu\mathrm{m}$) and provide detailed information about the influence of specific cytoskeletal elements. Using the microtubule and microfilament destabilizing agents, Nocodazole and Latrunculin A, it is determined that microfilaments are required for normal yeast mitochondrial motion while microtubules have no effect. Experiments with specific actin mutants revealed that actin is responsible for enhanced mobility on length scales greater than $0.6\ \mu\mathrm{m}$.

The versatility of FICS expands when individual molecules are labeled with fluorescent chromophores. In recent experiments on the tetrameric fluorescent protein DsRed, polarization-modulated FICS (PM-FICS) is demonstrated to separate conformational dynamics from molecular translational dynamics. The optical switching pathways of DsRed, a tetrameric complex of fluorescent protein subunits, are examined. An analysis of PM-FICS coordinate trajectories, in terms of 2D spectra and joint probability distributions, provides detailed information about the transition pathways between distinct dipole-coupled DsRed conformations.

This dissertation includes co-authored and previously published material.

CURRICULUM VITAE

NAME OF AUTHOR: Eric Nicolas Senning

PLACE OF BIRTH: Zürich, Switzerland

DATE OF BIRTH: October 23, 1978

GRADUATE AND UNDERGRADUATE SCHOOLS ATTENDED:

University of Oregon, Eugene
Colorado College, Colorado Springs

DEGREES AWARDED:

Doctor of Philosophy in Chemistry, 2009, University of Oregon
Bachelor of Arts *cum laude* in Biochemistry, 2001, Colorado College

AREAS OF SPECIAL INTEREST:

Biophysics
Physical Chemistry
Fluorescence Spectroscopy and Microscopy

PROFESSIONAL EXPERIENCE:

Research Assistant, Department of Chemistry, University of Oregon, 2003-2009

Teaching Assistant, Department of Chemistry, University of Oregon, 2002-2003 and 2007-2009

Research Assistant, Center of Environmental Biotechnology, University of Tennessee and Oak Ridge National Labs, 2000

GRANTS, AWARDS AND HONORS:

James Bernard Travel Award, University of Oregon, 2009

Phi Beta Kappa, 2001

Research Stipend, Oak Ridge Science Semester, 2000

E.V. Lindeman Research Grant, Colorado College, 2000

PUBLICATIONS:

Eric Senning, Geoffrey Lott, Michael Fink and Andrew Marcus, "II. Kinetic Pathways of Switching Optical Conformations in DsRed by 2D Fourier Imaging Correlation Spectroscopy," J. Phys. Chem. B **113**, 6854 (2009).

Geoffrey Lott, Eric Senning, Michael Fink and Andrew Marcus, "I. Conformational Dynamics of Biological Macromolecules by Polarization-Modulated Fourier Imaging Correlation Spectroscopy," J. Phys. Chem. B **113**, 6847 (2009).

Eric Senning, Geoffrey Lott and Andrew Marcus, "Fourier Imaging Correlation Spectroscopy for Cellular Structure-Function," Methods in Cell Biology **90**, 117 (2008).

Morgan Goulding, Julie Canman, Eric Senning, Andrew Marcus and Bruce Bowerman, "Control of nuclear centration in the C. elegans zygote by receptor-independent Galpha signaling and myosin II," JCB **178**, 1177 (2007).

ACKNOWLEDGMENTS

I wish to thank the many people that I've had the pleasure of meeting and interacting with during the course of completing my graduate work at the University of Oregon. First and foremost, I was very fortunate to have Dr. Andrew H. Marcus as my advisor. It has been inspirational to work alongside him and share in his dedication and passion for scientific research. Our research group was also an incredible resource for ideas and help, who's past and present members include: Dr. Michael Fink, Dr. Kenneth Adair, Geoff Lott, Aurelia Honerkamp-Smith, Dr. Patrick Tekavec and Dr. Michelle Knowles.

I owe a debt of gratitude to the Institute of Moleculuar Biology at the University of Oregon, specifically the labs of Dr. Tom Stevens and Dr. George Sprague for the use of their facilities and help with yeast cultures. I also wish to acknowledge the lab of Dr. S. James Remington for the generous supply of fluorescent DsRed protein. The experiments would not have been possible without the efforts made by Clifford Dax from the TSA electronics shop. His expertise was essential to the success of this work. As committee members, Dr. Marina Guenza, Dr. Peter von Hippel and Dr. John Toner also provided helpful discussions and insight throughout my graduate career.

I am thankful for my family's support, which has always been a comfort as I continued on my path to become a researcher, and I am most grateful to my wife Erin for her words of encouragement on many, many occasions.

This work was supported in part by the National Institutes of Health and the National Science Foundation.

TABLE OF CONTENTS

LIST OF FIGURES

Figure Page

Figure Page

LIST OF TABLES

Table Page

CHAPTER I

INTRODUCTION

The intracellular space of the eukaryotic cell can be characterized as a heterogeneous environment by the sheer variety of its many components. It is crowded with the molecules, macromolecules and organelles that maintain its proper function. The protein component alone can account for densities over 200 mg/ml. Despite this high degree of viscosity, the interior of the cell is also an extremely dynamic environment. Smaller messenger molecules rely on diffusive processes to arrive at their designated target sites, and larger macromolecules and organelles resort to means of transport assisted by the forces generated through molecular motors. Nevertheless, movement is in many cases also constrained by the variety of structures present in the cell. The dynamics of intracellular species therefore often defy any simple attempt at modeling their translational behavior, which further complicates the interaction picture of proteins, macromolecules and organelles.

Being that it is of fundamental importance to comprehend how components of the cell negotiate their way around the cytosolic environment, the advent of fluorescence microscopy brought our understanding of cell function to a new level. No longer limited

by methods that exploit the birefringent character of a handful of cellular components or stains that preferentially accumulate in a certain cellular compartment, researchers could now target a fluorescent probe to any desired component in the cell. This expanded upon the variety of cellular processes one could track and follow and breached the barrier to studying the dynamics of single molecules in the cell.

Fluorescence Microscopy on Small Cellular Components

As researchers extend their studies to shorter time scales and smaller objects, the demands placed on fluorescence microscopy expose certain limitations to this method. At the forfront of technological developments are improved sensors and cameras to increase the signal collected in fluorescence experiments. Along with better fluorescent labels, these advancements contribute towards the ultimate prize of being able to observe the intracellular behavior of single molecules. In the realm of imaging with a CCD camera, there are ensemble-averaged (high signal) methods, such as Fluorescence Recovery After Photobleach (FRAP), which record the bulk behavior of many fluorescently tagged objects. The advantage of tracking a single object in the cell is that one may ascribe a distribution to the object's movement, which is essential to fully characterizing its translational dynamics (Figure 1.1).

There are, however, numerous obstacles to observing the dynamics of a single entity with a CCD camera. First and foremost, due to the heterogeneous constitution of the cell interior, there is a strong auto-fluorescence contribution to the collected signal,

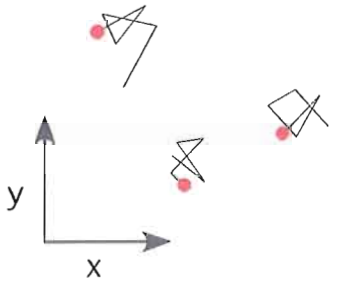

Figure 1.1. Direct imaging of microscopic particles with a CCD camera. With each segment representing the displacement of a particle in the time frame between exposures, the distribution in the dynamic behavior for each particle can be captured with this method.

which drops the signal to noise level considerably. Secondly, the fluorescent light collected over the course of the experiment diminishes as the fluorescent tags photobleach. Therefore, the number of frames (i) captured by a CCD camera may be approximated by

$$iCCD \sim \Omega / \varepsilon , \tag{1.1}$$

where Ω denotes the average number of photons a fluorescent object emits before its fluorophores are degraded, and ε is the threshold number of photons that a set of pixels in the CCD need to detect before discerning the object from the background [1]. The success of any CCD fluorescence microscopy tracking experiment is contingent on technological advances in camera sensitivity and fluorophore lifetime. In addition to the technological limitations of CCD fluorescence microscopy, there is the potential for damage to the cell because of the high photon flux or reactive oxygen species generated

by the fluorophore [2, 3]. This is especially true if short time scale dynamics are investigated with high intensity excitation light.

Improving Signal to Noise through Measurements of Sub-Ensembles

Since the development of Fluorescence Correlation Spectroscopy (FCS) over 30 years ago, it has been implemented to study translational diffusion, molecular aggregation and chemical rate kinetics in the cell [4, 5]. FCS monitors the variation in number of fluorescent particles occupying a small laser excited volume (Figure 1.2). The fluctuation of the fluorescence emission collected on a single element detector is then proportional to the diffusion of the fluorescent molecules as these move into and out of the laser excitation field.

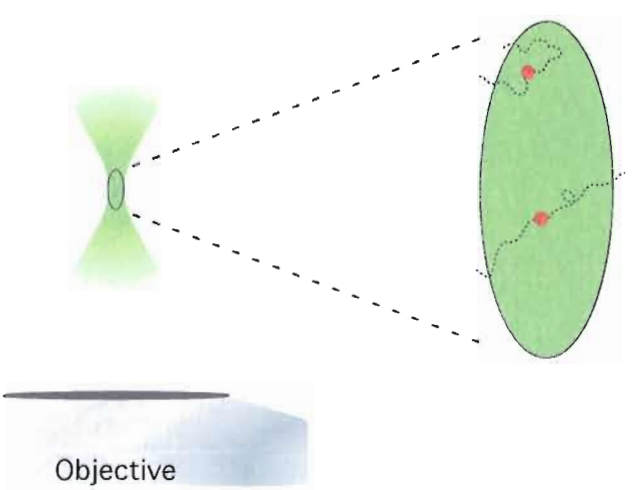

Figure 1.2. Rendering of an FCS experiment. Two particles travel into the excitation volume at the focal point in the sample and cause a fluctuation in the emitted fluorescence. The zoomed in portion to the right shows the random path of each fluorescent particle as it travels through the excitation volume.

A distinct advantage of FCS over CCD fluorescence microscopy methods is that the efficiency of signal acquisition is increased by a factor proportional to the number of molecules in the laser excitation volume,

$$iFCS \sim N * \Omega / \varepsilon \tag{1.2}$$

In Equation 1.2, N denotes the number of molecules excited by the laser light. Although this method is an improvement over the efficiency of CCD fluorescence microscopy, the data derived from FCS relies on a model dependent interpretation. The laser excitation volume through which the fluorescent molecule diffuses must be carefully calibrated before any assessment of translational dynamics is made. Furthermore, only a small number of fluorescent molecules may occupy the excitation volume at any one time since a large number of molecules in the excitation volume will lower the sensitivity to a molecular fluctuation. As with direct imaging experiments, one may increase the signal from the sample volume with higher intensity excitation light so as to gain improved temporal resolution; however, this can also have the undesirable effect of driving the optical behavior of the chromophore into a non-linear regime and further complicate any interpretation of the data. This non-linear phenomena has been observed in the spectral properties of several fluorescent proteins commonly used in FCS [6, 7].

Length Scale Dependence of Movement and Fourier Imaging Correlation Spectroscopy

A significant aspect of observing the translational motion of objects in cells is that the cellular environment may be described as a complex fluid. In the cell, this complexity arises from the diversity in subcellular structures from large membranous organelles to various protein filaments, such as actin and microtubules, to small metabolic compounds. These structures act on the dynamical behavior of objects in a length scale dependent manner; objects having to traverse larger length-scales will be impacted by the larger subcelluar constituents, such as the organelles, while the short-length scale dynamics may remain unaffected. The overall dynamic behavior inside the cell is thus determined by the cellular components imparting different degrees of mobility relevant to length scale. In fact, a length scale dependent analysis of movement would define a distribution akin to the aforementioned distribution of jumps observed in CCD imaging techniques.

The constraints imposed by the limited efficiency of CCD fluorescence microscopy and the complications imposed by the model dependent interpretation of FCS data led to the development of Fourier imaging correlation spectroscopy (FICS). This method expands on the concept of observing fluorescence fluctuations as is done in the FCS experiment; however, by incorporating a means to account for length scale, FICS is able to circumvent a model dependent interpretation of the signal. Being able to isolate a single length-scale in a FICS experiment is also advantageous to the experimenter because it improves the signal in the measurement. As was the case with FCS, the signal strength in FICS is still proportional to $\sim N * \Omega / \varepsilon$; however, the signal is acquired over a

much larger region than the small excitation volume of the FCS experiment. In FICS, the molecular fluctuation in the experiment is observed as a fluctuation in the total fluorescence due to changes in overlap of a fluorescently labeled particle subensemble and a laser excitation profile,

$$I_f(\phi_G,t)=\int_{-\infty}^{\infty} I_L(\mathbf{r},\phi_G)c(\mathbf{r},t)d\mathbf{r}\,. \tag{1.3}$$

Here, $I_f(\phi_G,t)$ is the total intensity at the detector; $c(\mathbf{r},t)$ is the spatial configuration of the ensemble, and a repeating excitation profile is defined as $I_L(\mathbf{r},\phi_G)\propto 1+\cos(\mathbf{k}_G\cdot\mathbf{r}+\phi_G)$ with wave vector $\mathbf{k}_G$. Since the excitation profile extends throughout the field of view, the fluorescence intensity is collected from a vast number of labeled particles. This particular aspect of FICS permits the use of a low power excitation intensity and reduces the risk of inducing non-linear optical behavior, photobleaching of the fluorescent particles and exposure of the cell to photoreactive molecules.

Measuring Dynamic Behavior

Although it is now clear that conducting a fluorescence microscopy experiment one length-scale at a time can significantly improve the signal collected during the experiment, it is worth considering how this signal informs us on a system's dynamic behavior. The FICS fluctuation detected in the fluorescently labeled subensemble must

relate to a familiar form of dynamic characterization such as the dynamic variables one observes in direct observations made with CCD methods.

A direct approach to ascertain the dynamics of a point particle is to track its time-dependent behavior. Barring any limitations to the dynamic range of the experimental set-up, a complete dynamic picture of a small particle is possible by recording its trajectory from the shortest time intervals to the longest time intervals. Particle displacements collected as $\Delta r_i = r_i(t+\tau) - r_i(t)$, where r_i is the position of the i^{th} particle and τ is the time interval, may then be presented as a time-dependent distribution function known as the van Hove function,

$$G_s(r,\tau) = \frac{1}{N}\left\langle \sum_{i=1}^{N} \delta[\mathbf{r} + \mathbf{r}_i(t) - \mathbf{r}_i(t+\tau)] \right\rangle. \tag{1.4}$$

Here, $G_s(r,\tau)$ accounts for only the self-displacement of individual particles and the function tells us the time-dependent conditional probability density that a particle suffers a displacement $r = |\mathbf{r}(t+\tau) - \mathbf{r}(t)|$ during a time interval τ [8]. The usefulness of expressing the particle displacements as a probability distribution is apparent when we consider how it relates to the random movement of a particle.

If the distribution function $G_s(r,t)$ is made up of particle displacements characterized by diffusive motion, then the central limit approximation for the distribution will give it a Gaussian profile,

$$G_s(\mathbf{R},t) = \left[\frac{2\pi}{3}\left\langle \Delta R^2(t) \right\rangle\right]^{-3/2} \exp\left[\frac{-3R^2}{2\left\langle \Delta R^2(t) \right\rangle}\right]. \tag{1.5}$$

In this expression, the mean-square displacement is given as $\langle \Delta R^2(t) \rangle$. Under circumstances where the particle can travel along an uninterrupted path for extended periods of time, the mean-square displacement will scale as $\sim t^2$ [9]. This type of motion would appear to be ballistic, but if it were observed in the cell, a possible underlying mechanism would be the active transport of a particle to a target location. Because particles in a liquid have any motion damped by the surrounding medium, a mean free path inside the cell is very short. The thermally driven, hopping movement of particles would then be characterized as Brownian, where

$$\langle \Delta R^2(t) \rangle = 6Dt. \tag{1.6}$$

Dynamics of Brownian systems are very simple to model since the diffusion coefficient, D, can be approximated by the Stokes-Einstein equation,

$$D \approx \frac{k_B T}{6\pi\eta a}, \tag{1.7}$$

where k_B is Boltzmann's constant, T is temperature, η is the viscosity of the surroundings and a is the hydrodynamic radius of the particle. Temporal scaling of the mean-square displacement is subject to a power law relation with real, physical meaning. Exponents of t in $\langle \Delta R^2(t) \rangle$ may range from 2 to 1 and, in the sub-diffusive case, less

than 1.[1] The temporal scaling of the mean-square displacement therefore happens to be a useful dynamic variable for characterizing time-dependent behavior, and the fluctuation measurement of a particle ensemble in FICS relates back to this variable.

Length-Scale Dependent Measurements of a Sub-Ensemble's Dynamics with FICS

As we return our attention to the FICS signal generated by overlapping an excitation grating profile with our subensemble of particles as presented in equation 1.3, it should be made clear that our subensemble is given as a microscopic density $c(\mathbf{r},t)=\frac{1}{V}\sum_{i=1}^{N}A_i\,\delta\left[\mathbf{r}-\mathbf{r}_i(t)\right]$, where V is the volume, A_i is the absorption and emission efficiency of the fluorescent particle and δ is the Dirac delta function. The particle density becomes non-zero in the vicinity of a fluorescent particle. On completing the integration of Equation 1.3, the resultant expression for the fluorescence is a Fourier component of our microscopic density,

$$I_f(\phi_G,t)=I_0\langle c\rangle+I_0\left|\hat{c}_{k_G}(t)\right|\cos\left[\gamma_{k_G}(t)+\phi_G\right], \tag{1.8}$$

[1] The change from a temporal scaling power of 2 to 1 is a consequence of the velocity autocorrelation function going to zero in the time interval that successive particle displacements are recorded.
$\left\langle \Delta R^2(t)\right\rangle=\int_0^t dt_2\int_0^{t_2}dt_1\left\langle \mathbf{V}(t_1)\cdot\mathbf{V}(t_2)\right\rangle \xrightarrow[t\to\infty]{} 2t\int_0^{\infty}d\tau\left\langle \mathbf{V}(0)\cdot\mathbf{V}(\tau)\right\rangle$, where the second integral is proportional to the diffusion coefficient for times that are long compared to the velocity-correlation time [9].

where $\langle c \rangle$ is the mean concentration, $\left|\hat{c}_{k_G}(t)\right|$ and $\gamma_{k_G}(t)$ are the amplitude and phase of the Fourier component $\hat{c}_{k_G}(t) = \left(\frac{1}{2\pi}\right)^{3/2} \int_{\infty}^{\infty} c(\mathbf{r},t) e^{-i\mathbf{k}_G \cdot \mathbf{r}} d\mathbf{r}$ and $\vec{k}_G = \left|2\pi / d_G\right| \hat{i}$ is the wave-vector defined by the separation of the fringes, d_G, in the excitation profile. Because ϕ_G is an experimental parameter that is removed from the signal, we are able to retrieve $\hat{c}_{k_G}(t)$ and identify each data point in a FICS experiment as a phase-selective measurement. The advantage of making phase-selective measurements is developed in chapter II, but a simple analysis of the translational dynamics is also accomplished by generating a time autocorrelation of the Fourier component,

$$F_s(k_G,\tau) = \left\langle \hat{c}_{k_G}(t) \hat{c}^*_{k_G}(t+\tau) \right\rangle \tag{1.9}$$

where τ is the time lag of the autocorrelation function. The time correlation function $F_s(k_G,\tau)$ is a statistically averaged distribution function related to the van Hove function by its Fourier transform,

$$F_s(k_G,\tau) = \int d^3R G_s(\mathbf{R},\tau) e^{i\mathbf{k}_G \cdot \mathbf{R}}. \tag{1.10}$$

The intermediate scattering function, $F_s(k_G,\tau)$, is thus able to reconnect with dynamic variables such as $G_s(\mathbf{R},\tau)$, which we previously identified through conventional

trajectory charting methods used in CCD fluorescence microscopy. Moreover, if the central limit theorem holds for our particular subensemble of fluorescent particles, then

$$F_s\left(k_G,\tau\right)=\exp\left(-k_G^2\left\langle\Delta R^2\left(t\right)\right\rangle/6\right) \tag{1.11}$$

gives us a relation to characterize the temporal scaling of the mean-square displacement.

Phase-Selective Measurements with FICS

The aforementioned relation of the FICS obervable, $\hat{c}_{k_G}\left(t\right)$, to a time evolving function such as the mean-square displacement establishes that FICS is an effective tool for studying translational dynamics. The phase-selective nature of the Fourier component extends the sensitivity of FICS to smaller length-scales than defined by the laser excitation pattern, and in chapter II we review in detail the treatment of the measurement that makes this approximation possible. Chapter II contains co-authored material from previously published research. A formidable advantage of the phase-selectivity in FICS emerges with experiments on single molecules labeled with two fluorophores. This variant of FICS is termed polarization modulated FICS (PM-FICS), and it is able to separate the signal component imparted through translational dynamics from that which arises due to optical changes caused by conformational fluctuations.

Live Cell Studies of Mitochondrial Dynamics with FICS

In the biological context, we anticipate labeled particles to exhibit more complicated behavior than simple Brownian motion. Previous FICS research on mitochondria of osteosarcoma cells identified a strong dependence on actin microfilaments and microtubules for the normal dynamic state of the organelle [10]. Using the model organism *S. cerevisiae*, which is commonly known as baker's yeast, the time dependent movement of mitochondria as dependent on the cytoskeleton is characterized and discussed in chapter III. Since the temporal scaling behavior of $\langle \Delta R^2(t) \rangle$ is a recognized method for understanding intracellular movement, the framework of our investigation into mitochondrial dynamics is set up around this variable [11, 12]. In addition to characterizing the dynamics of mitochondria under conditions where a drastic change to cytoskeletal function is made, the study probes how slight perturbations to the cytoskeleton may influence the movement of this organelle. Both cytoskeletal inhibiting drugs and mutant genetic strains are implemented in this analysis of how mitochondrial dynamics depend on the integrity of the cytoskeleton.

Optical Conformation Fluctuations of DsRed

After outlining a method in chapter II to separate dynamics due to translational fluctuations in the PM-FICS signal from internal depolarization fluctuations, dynamics of the tetrameric fluorescent protein DsRed are studied and discussed in chapter IV. Chapter

IV contains co-authored work that appears in previously published journal articles. In an analogy to 2D NMR spectra, we generate 2D optical spectra with the phase-selective signals derived from PM-FICS measurements on DsRed. By moving to higher four point correlation functions, the PM-FICS optical anisotropy signal due to Forster energy transfer events between two chromophores can lead us to putative models of molecular inter-conversion between different DsRed conformational states. This chapter exemplifies the potency of PM-FICS as a new, optical method to study intra-molecular dynamics with applications ranging from live cell biology to microscopic dynamics occurring at the glass transition.

CHAPTER II

FOURIER IMAGING CORRELATION SPECTROSCOPY FOR CELLULAR STRUCTURE-FUNCTION

This chapter is an overview of the experimental method pertaining to FICS and is essential to an understanding of what follows in the experiments discussed in chapters III and IV. Credit for the construction and implementation of a PM-FICS instrument to study the fluorescent protein DsRed goes to M. Fink, K. Adair and G. Lott. The results from their experiments made a more rigorous analysis of DsRed in chapter IV possible.

The subject of this chapter introduces the reader to the underlying principles of how Fourier imaging correlation spectroscopy (FICS) is able to extract dynamic information from a fluorescently labeled microscopic sample. After introducing the mathematical concepts at work in a FICS experiment, the design and implementation of a FICS instrument is presented along with results from two experiments. The first experiment exemplifies the use of FICS in larger subcellular structures such as the mitochondria, and a more detailed analysis of the results in this experiment is dealt with in chapter III. The second experimental setup to be presented here for single molecule

studies is termed polarization-modulated FICS (PM-FICS). While many of the underlying principles remain the same, the extension of FICS experiments into the single molecule domain requires a polarization sensitive detection scheme and corresponding change to the interpretation of the signal.

Background

In densely crowded macromolecular suspensions, molecular motions are often temporally and spatially correlated. In living cells, molecular motions are further complicated by a dispersion of molecular sizes and shapes, cell compartmental organization, and the influence of cytoskeletal-related proteins. Experiments that optically probe the motions of intracellular species can quantify such motions and thus shed light on the underlying mechanisms of intracellular transport. Similarly, experiments that determine center-of-mass motions and internal conformational transitions of biological macromolecules have the potential to examine mechanisms of biochemical activity in living cells.

Single-molecule imaging (SMI) experiments [1], which observe the fluorescence fluctuations of individual labeled macromolecules, and fluorescence correlation spectroscopy (FCS) [2], which measures fluctuations from many molecules in a tightly focused laser spot, are established methods to study the dynamics of intracellular species. The SMI observables are the nanometer center-of-mass displacements of individual molecules, with temporal and spatial resolution determined by the S/N. In contrast, FCS

achieves a high dynamic range by spatially integrating the emission from many molecules, which are illuminated by a tightly focused laser beam. Although precise information about molecular coordinates is "blurred" by the spatial integration of the measurement, the S/N ratio is enhanced by the factor N, corresponding to the number of molecules within the observation volume. Thus, SMI and FCS exemplify two very different parameterizations to the problem of balancing S/N and the acquisition of detailed molecular coordinate information.

To improve on the capabilities of low signal *in vivo* measurements, it is useful to develop new ways to adjust the balance between S/N and the level of signal averaging over microscopic coordinates. This chapter reviews FICS [3-8], a phase-selective approach to fluorescence fluctuation spectroscopy that is based on the principle that fluctuations in partially averaged microscopic coordinates can be monitored through variations of an optical signal phase. Unlike SMI and FCS, FICS obtains its signal from a relatively large sample volume, so that it does not share with these methods the advantage of spatial localization. The advantages of FICS are *i*) that it boosts its S/N ($\propto \sqrt{\text{signal}}$) well above SMI values by observing a comparatively large number of fluorescent species ($N \sim 10^6$), thus facilitating studies in living cells; and *ii*) that its signal represents a partial average over microscopic coordinates that retains significant detail about particle trajectories. In particular, the information provided by FICS is suitable to study temporal and spatial correlations of particle motions, in addition to conformational transitions of biological macromolecules.

Theoretical Descriptions of Fourier Imaging Correlation Spectroscopy

FICS has been used to study the motions of mitochondrial membranes in living cells [9, 10]. More recently, the FICS method was extended to perform low signal measurements of the diffusion of fluorescent proteins in dilute viscous solutions [3]. The theoretical principles of these measurements, including their applications to polarization resolved studies of intra-molecular conformational transitions [4], are described below.

FICS for Studies of Intracellular Dynamics of Organelles. Illustrated in Figure 2.1A are two laser beams crossed at the sample plane of a fluorescence microscope to create a spatially modulated intensity grating. The laser resonantly excites chromophore labels in the sample, and the backward emitted fluorescence is separated from the excitation light and focused onto a detector. Figures 2.1B and 2.1C schematically depict the overlap of the intensity grating with a population of biological cells, for which N intracellular compartments are fluorescently labeled (indicated by interconnected gray disks). The average separation between the fluorescent sites must be large enough to roughly match the optical fringe spacing ($d_G \simeq 0.5 - 5\ \mu\text{m}$), which can be adjusted by changing the angle between the intersecting laser beams. Typically, the beam waist ($w \simeq 35 - 100\ \mu\text{m}$) spans at least ten optical fringes, so that the illuminated sample encompasses a large volume $V \simeq 1{,}500 - 80{,}000$ fl. Since $w \gg d_G$, we approximate the intensity profile as an infinite plane wave, $I_L(\mathbf{r},\phi_G) = I_0\left[1+\cos\left(\mathbf{k}_G \cdot \mathbf{r} + \phi_G\right)\right]$, where I_0 is a constant intensity, $\mathbf{k}_G$ is the wave vector of the optical grating, and ϕ_G is the grating phase.

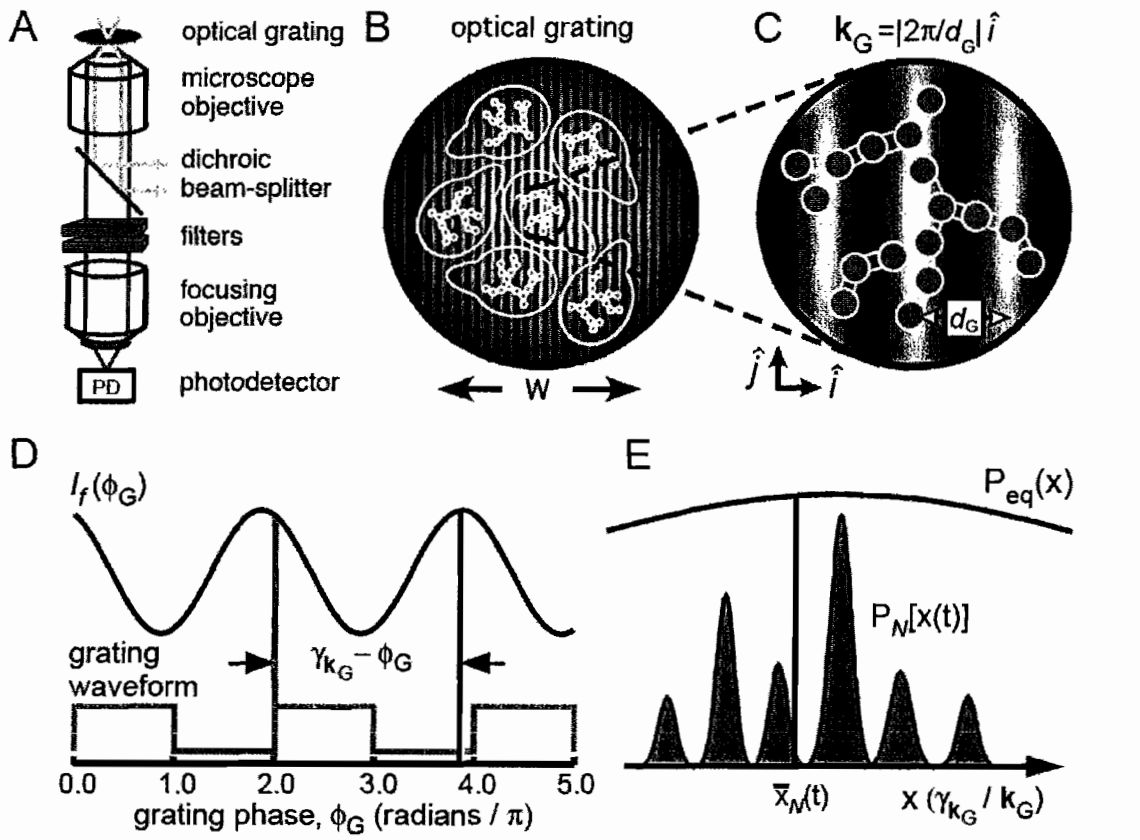

Figure 2.1. Schematic diagram of the optical layout for FICS experiments, performed on fluorescently labeled yeast mitochondria. (A) The sample is placed at the focal plane of a fluorescence microscope. The excitation beams (light gray lines) are sent to a focusing objective using a dichroic beam-splitter, and create a spatially modulated intensity grating at the sample. The spatially integrated fluorescence (dark gray lines) is collected by the same objective and focused onto a photo-detector. (B) Condensed view of the focused laser spot with beam waist ~ 50 μm. (C) Fluorescently labeled mitochondrial filaments, represented as N interconnected gray disks, are excited by the optical grating with fringe spacing d_G. Signal fluctuations occur as mitochondrial filaments move relative to one another. (D) Schematic of the total fluorescence intensity I_f as a function of the grating phase ϕ_G. The modulated component of the signal has phase γ_{k_G}. (E) The signal phase is proportional to the mean position $\bar{x}_N(t)$ of the sampled particle distribution $P_N[x(t)]$. The sampled distribution is a time-dependent subset of the equilibrium distribution $P_{eq}(x)$.

The fluorescence intensity I_f is proportional to the spatial overlap of the fluorescent particle sites with the optical grating intensity profile

$$I_f(\phi_G,t)=\int_{-\infty}^{\infty} I_L(\mathbf{r},\phi_G)c(\mathbf{r},t)d^3\mathbf{r}. \tag{1.3}$$

In Equation 1.3 the local particle concentration is $c(\mathbf{r},t)=\frac{1}{V}\sum_{i=1}^{N} A_i\,\delta\left[\mathbf{r}-\mathbf{r}_i(t)\right]$, where the constants A_i represent the absorption / emission efficiencies of the individual sites, and $\delta(x)$ is the Dirac delta function. After carrying out the spatial integration of Equation 1.3, the fluorescence intensity takes the form [3]

$$I_f(\phi_G,t)=I_0\langle c\rangle+I_0\left|\hat{c}_{k_G}(t)\right|\cos\left[\gamma_{k_G}(t)+\phi_G\right], \tag{1.8}$$

where $\langle c\rangle=\frac{1}{V}\sum_{i=1}^{N} A_i$ is the mean concentration, and $\left|\hat{c}_{k_G}(t)\right|$ and $\gamma_{k_G}(t)$ are, respectively, the amplitude and the phase of the spatial Fourier component of the local particle concentration:

$$\hat{c}_{k_G}(t)=\left(\tfrac{1}{2\pi}\right)^{3/2}\int_{-\infty}^{\infty} c(\mathbf{r},t)e^{-i\mathbf{k}_G\cdot\mathbf{r}}d\mathbf{r}=\sum_{i=1}^{N} A_i\exp\left[i\mathbf{k}_G\cdot\mathbf{r}_i(t)\right]. \tag{2.1}$$

Equation 2.1 shows that the signal consists of two parts; a stationary (dc) background, proportional to *N*, and a ϕ_G-dependent (ac) term with amplitude $\left|\hat{c}_{k_G}(t)\right| \propto \sqrt{N}$. Figure 2.1D illustrates how the phase of the modulated fluorescence intensity is shifted by an amount $\gamma_{k_G}(t)$ relative to the phase of the optical grating. The FICS apparatus applies a sweep to the phase $\phi_G(t') = \omega_G t' + \phi_0$ at the carrier frequency $\omega_G/2\pi$ = 10 MHz. The period of the modulation is much longer than the fluorescence lifetime, but short in comparison to the center-of-mass coordinate fluctuations. Phase-sensitive detection and low-pass filtering techniques are used to determine the 'in-phase' $\left[X_{k_G}(t) \propto \left|\hat{c}_{k_G}(t)\right|\cos\gamma_{k_G}(t)\right]$ and the 'in-quadrature' $\left[Y_{k_G}(t) \propto \left|\hat{c}_{k_G}(t)\right|\sin\gamma_{k_G}(t)\right]$ signal components. These two quadratures fully characterize the complex signal $X_{k_G}(t) + iY_{k_G}(t) = \hat{c}_{k_G}(t)$, which is equivalently specified by the amplitude $\left|\hat{c}_{k_G}(t)\right|$ and the phase $\gamma_{k_G}(t)$. It is important to note that the precision to which the signals are determined depends on the S/N ($\propto \sqrt{N}$) of a particular measurement. Because the signal is spatially integrated over a sample with $N \approx 10^6$, the enhancement of the S/N in comparison to single-particle measurements is about a thousand-fold.

Equation 2.1 shows that the time-dependence of $\hat{c}_{k_G}(t)$ arises due to particle coordinate fluctuations, which are projected onto the fringes of the optical grating. Since the grating wave vector $\mathbf{k}_G$ points in the $\hat{i}$-direction, only the *x*-components of the coordinates contribute to the signal. The *N* coordinates $\{x_1(t), x_2(t), ..., x_N(t)\}$ fluctuate

continuously about their mean values according to $x_i(t) = \delta x_i(t) + \langle x_i \rangle$. In Figure 2.1E, we schematically represent a hypothetical continuous distribution $P_{eq}(x)$ that describes the equilibrium probability of observing a randomly selected particle with coordinate x, mean $\langle x \rangle_{eq} = \int_{-\infty}^{\infty} x P_{eq}(x) dx = 0$ and variance $\sigma_{eq}^2 = \int_{-\infty}^{\infty} x^2 P_{eq}(x) dx$. At a given instant, the FICS signal samples the Fourier transform $\hat{c}_{k_G}(t)$ of a subset $P_N[x(t)] = c(x,t) = \frac{1}{N}\sum_{i=1}^{N} A_i \delta[x - x_i(t)]$ of the equilibrium distribution. According to the central limit theorem, the sampled distribution has mean value $\bar{x}_N(t) = \sum_{i=1}^{N} x_i(t) P_N[x_i(t)]$ and variance $\sigma_N^2 = [\delta \bar{x}_N(t)]^2 = \sum_{i=1}^{N} x_i^2(t) P_N[x_i(t)] \propto \sigma_{eq}^2 / N$, which is narrowed relative to the equilibrium distribution by the factor N^{-1}. According to Equation 2.1, the FICS signal is a characteristic function of $P_N[x(t)]$: $\hat{c}_{k_G}(t) = \sum_{i=1}^{N} A_i e^{ik_G x_i(t)} = \sum_{i=1}^{N} P_N[x_i(t)] e^{ik_G x_i(t)}$. Using the theory of cumulants [11], the FICS signal can be Taylor expanded in terms of the raw moments of $P_N[x(t)]$:

$$\hat{c}_{k_G}(t) = \sum_{m=0}^{\infty} \frac{(ik_G)^m}{m!} \mu'_m, \text{ where } \mu'_m(t) = \int_{-\infty}^{\infty} x^m(t) P_N[x(t)] dx(t). \tag{2.2}$$

Alternatively, an expansion of the logarithm of $\hat{c}_{k_G}(t)$ defines the cumulants:

$$\ln \hat{c}_{k_G}(t) = \sum_{m=1}^{\infty} \frac{(ik_G)^m}{m!} \kappa_m(t). \tag{2.3}$$

A term-by-term comparison between Equations 2.2 and 2.3 leads to $\kappa_1(t) = \mu_1'(t) = \bar{x}_N(t)$, and $\kappa_2 = \mu_2' - \mu_1'^2 = \left\langle \left[x_N(t) - \bar{x}_N(t) \right]^2 \right\rangle = \left[\delta \bar{x}_N(t) \right]^2$. A good approximation of $\hat{c}_{k_G}(t)$ is given by the cumulant expansion of Equation 2.3, truncated at $m = 2$.

$$\hat{c}_{k_G}(t) \simeq \exp\left\{ ik_G \bar{x}_N(t) - \frac{1}{2} k_G^2 \left[\delta \bar{x}_N(t) \right]^2 \right\}. \tag{2.4}$$

Equation 2.4 shows that the measured phase and the amplitude of $\hat{c}_{k_G}(t)$ can be assigned to physical meanings: $\gamma_{k_G}(t) = k_G \bar{x}_N(t)$ and $\left| \hat{c}_{k_G}(t) \right| = \exp\left\{ -\frac{1}{2} k_G^2 \left[\delta \bar{x}_N(t) \right]^2 \right\}$, respectively. In this way, the FICS observable determines the size N of the sampled distribution {through the relationship $\left[\delta \bar{x}_N(t) \right]^2 \propto N^{-1}$}, and its mean value (illustrated in Figure 2.1E).

Polarization-Modulated FICS for Studies of Biomolecular Dynamics. In the above discussion, the number of fluorescent molecules that decorate each particle site is large ($\geq 10^3$), so that the system is optically isotropic. When the individual sites correspond to isolated fluorescent molecules, then the system has a continuously fluctuating steady-

state anisotropy. If the polarizations of the exciting laser and the detected emission are specified, the FICS signal can contain information about molecular anisotropy fluctuations, in addition to center-of-mass motions. As discussed further below, the anisotropy fluctuations can reflect conformational transitions of appropriately labeled macromolecules.

In polarization-modulated FICS, two orthogonal elliptically polarized laser beams are used to create the optical grating (Figure 2.2A). The crossed beams simultaneously generate a linear polarization grating and an intensity interference pattern at the sample

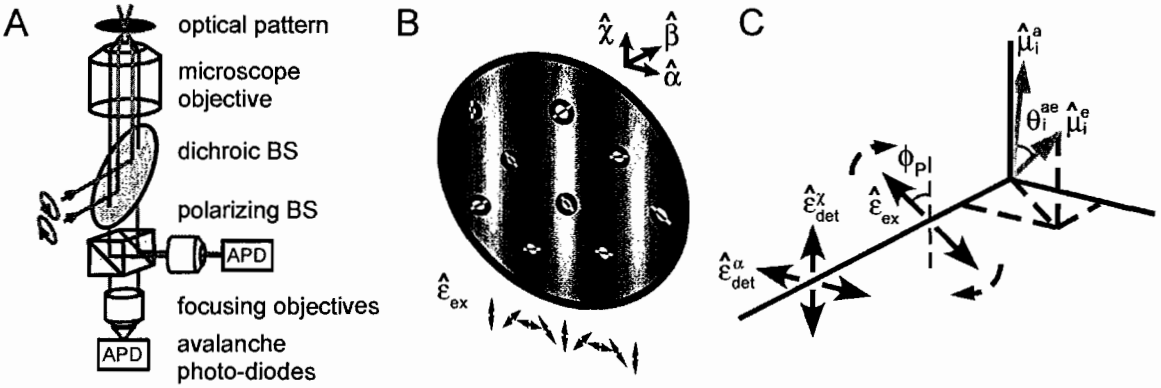

Figure 2.2. (A) Schematic diagram of the optical layout for FICS experiments, performed on fluorescent proteins in dilute viscous solution. Two orthogonal, elliptically polarized laser beams are crossed at the sample plane of a fluorescence microscope. The spatially and temporally integrated fluorescence is split using a polarizing beam-splitter (BS), and detected in parallel using two synchronized photon-counting detectors. (B) At the sample, the superposition of the two laser beams creates (simultaneously) a spatially modulated intensity interference pattern and a plane polarization grating. Molecular chromophores are depicted as white circles bisected by line segments, indicating the orientations of transition dipoles. (C) Each optical chromophore is characterized by its absorption and emission dipole moments ($\hat{\mu}_i^a$ and $\hat{\mu}_i^e$, respectively), and its depolarization angle θ_i^{ae}. The two polarized emission signals are each projected onto orthogonal laboratory frame axes (labeled $\hat{\alpha}$ and $\hat{\chi}$).

(Figure 2.2B). The signal fluctuations arise from combined projections of the molecular center-of-mass coordinates onto the intensity grating, and the transition dipole orientational coordinates onto the polarization grating. The polarized fluorescence is separated into laboratory frame orthogonal directions using a polarizing beam splitter, and both signals are phase-synchronously detected.

The plane-polarized fluorescence intensity from the *i*th molecule $A_i^{\alpha,\chi}\left(\theta_i^{ae},\phi_P\right)$ is proportional to $\left\langle\left|\hat{\varepsilon}_{ex}\left(\phi_P\right)\cdot\hat{\mu}_i^a\right|^2\left|\hat{\varepsilon}_{det}^{\alpha,\chi}\cdot\hat{\mu}_i^e\right|^2\right\rangle$, where $\hat{\mu}_i^a$ and $\hat{\mu}_i^e$ are the absorption and emission transition dipole moments, respectively, and the angle brackets $\langle ... \rangle$ indicate an orientational average over the distribution of absorption dipoles [12]. As illustrated in Figure 2.2C, the laboratory frame detection electric field directions are given by $\hat{\varepsilon}_{det}^{\alpha}$ and $\hat{\varepsilon}_{det}^{\chi}$, and the rotating excitation field direction is given by $\hat{\varepsilon}_{ex}\left(\phi_P\right)=\sin\phi_P\hat{\alpha}+\cos\phi_P\hat{\chi}$. Assuming an isotropic distribution of absorption dipole moments, the orientational average leads to the following first-order approximations to the polarized, steady-state intensities [13]

$$A_i^{\alpha}\left(\theta_i^{ae},\phi_G\right)\simeq\left|\hat{\mu}_i^a\right|^2\left|\hat{\mu}_i^e\right|^2\left[\frac{17}{72}+\frac{23}{360}\cos\left(2\theta_i^{ae}\right)-\frac{1}{9}\cos\left(2\theta_i^{ae}-\phi_G\right)+\frac{1}{45}\cos\left(2\theta_i^{ae}+\phi_G\right)\right.$$
$$\left.-\frac{1}{72}\cos\left(\phi_G\right)-\frac{1}{48}\cos\left(2\theta_i^{ae}-2\phi_G\right)+\frac{1}{720}\cos\left(2\theta_i^{ae}+2\phi_G\right)\right], \tag{2.5}$$

and

$$A_i^{\chi}\left(\theta_i^{ae},\phi_G\right)\approx\left|\hat{\mu}_i^{a}\right|^2\left|\hat{\mu}_i^{e}\right|^2\left[\frac{17}{36}-\frac{23}{180}\cos\left(2\theta_i^{ae}\right)+\frac{2}{9}\cos\left(2\theta_i^{ae}-\phi_G\right)-\frac{2}{45}\cos\left(2\theta_i^{ae}+\phi_G\right)\right.$$

$$\left.-\frac{1}{36}\cos\left(\phi_G\right)+\frac{1}{24}\cos\left(2\theta_i^{ae}-2\phi_G\right)-\frac{1}{360}\cos\left(2\theta_i^{ae}+2\phi_G\right)\right]. \tag{2.6}$$

In Equations 2.5 and 2.6, θ_i^{ae} is the angle that subtends the absorption and emission dipole moments, and the excitation polarization angle is expressed in terms of the phase of the intensity grating $\phi_G = 2\phi_P$. Equations 2.5 and 2.6 also assume that the time scale of rotational diffusion is much longer than the fluorescence lifetime, which is typically a few nanoseconds.

The total fluorescence from the N molecules is obtained from the spatial integration of Equation 1.3. In this case, the local concentration of excited molecules is polarization-dependent, *i.e.* $c^{\alpha,\chi}\left(\mathbf{r},\theta^{ae}\right)=\frac{1}{V}\sum_{i=1}^{N}A_i^{\alpha,\chi}\left(\theta_i^{ae},\phi_G\right)\delta\left(\theta^{ae}-\theta_i^{ae}\right)\delta\left(\mathbf{r}-\mathbf{r}_i\right)$. The total fluorescence is given by [3]

$$I_f^{\alpha,\chi}\left(k_G,\phi_G,t\right)=\frac{I_0}{V}\sum_{i=1}^{N}A_i^{\alpha,\chi}\left[\theta_i^{ae}\left(t\right),\phi_G\right]\left\{1+\cos\left[k_G x_i\left(t\right)+\phi_G\right]\right\}. \tag{2.7}$$

The phase $\phi_G\left(t'\right)=\Omega t'+\phi_{G0}$ is swept at the carrier frequency $\Omega/2\pi$ = 10 MHz. The period of the modulation is much longer than the fluorescence lifetime and the rotational reorientation time, but short in comparison to the center-of-mass and conformational fluctuations of interest.

Substitution of Equations 2.5 and 2.6 into Equation 2.7, and retaining only the terms that are third-order in ϕ_G leads to

$$I_f^{\alpha}\left(k_{\mathrm{G}},\phi_G\right) \propto \frac{1}{6}\cos\left(k_{\mathrm{G}}x_n + 3\phi_G\right) + \frac{1}{4}\cos\left(k_{\mathrm{G}}x_n - 2\theta_n^{ae} + 3\phi_G\right) - \frac{1}{60}\cos\left(k_{\mathrm{G}}x_n + 2\theta_n^{ae} + 3\phi_G\right) \tag{2.8}$$

and

$$I_f^{\chi}\left(k_{\mathrm{G}},\phi_G\right) \propto \frac{1}{3}\cos\left(k_{\mathrm{G}}x_n + 3\phi_G\right) - \frac{1}{2}\cos\left(k_{\mathrm{G}}x_n - 2\theta_n^{ae} + 3\phi_G\right) + \frac{1}{30}\cos\left(k_{\mathrm{G}}x_n + 2\theta_n^{ae} + 3\phi_G\right) \tag{2.9}$$

Using phase sensitive detection techniques described in reference [3], the above signals are demodulated at three times the carrier frequency. One thus determines the in-phase [$X_{k_{\mathrm{G}}}^{\alpha,\chi} = I_f^{\alpha,\chi}\left(k_{\mathrm{G}}, 3\phi_G = 0\right)$] and in-quadrature [$Y_{k_{\mathrm{G}}}^{\alpha,\chi} = I_f^{\alpha,\chi}\left(k_{\mathrm{G}}, 3\phi_G = \pi/2\right)$] projections of the polarized fluorescence. These components are combined according to $Z_{k_{\mathrm{G}}}^{\alpha,\chi} = X_{k_{\mathrm{G}}}^{\alpha,\chi} + iY_{k_{\mathrm{G}}}^{\alpha,\chi}$ to obtain the complex-valued signals

$$Z_{k_G}^{\alpha} \propto \frac{1}{6}\exp i\left(k_{\mathrm{G}}x_n\right) + \frac{1}{4}\exp i\left(k_{\mathrm{G}}x_n - 2\theta_n^{ae}\right) - \frac{1}{60}\exp i\left(k_{\mathrm{G}}x_n - 2\theta_n^{ae}\right) \tag{2.10}$$

and

$$Z_{k_G}^{\chi} \propto \frac{1}{3}\exp i\left(k_{\mathrm{G}}x_n\right) - \frac{1}{2}\exp i\left(k_{\mathrm{G}}x_n - 2\theta_n^{ae}\right) + \frac{1}{30}\exp i\left(k_{\mathrm{G}}x_n - 2\theta_n^{ae}\right). \tag{2.11}$$

Because the final terms of Equations 2.10 and 2.11 are small in comparison to the leading terms, the complex signals are well approximated by

$$Z_{k_G}^{\chi}(t) \simeq \frac{I_0}{V}\sum_{i=1}^{N}\left|\hat{\mu}_i^a\right|^2\left|\hat{\mu}_i^e\right|^2\left\{\tfrac{1}{3}\exp i\left[k_G x_i(t)\right]-\tfrac{1}{2}\exp i\left[k_G x_i(t)-2\theta_i^{ae}(t)\right]\right\}, \tag{2.12}$$

and

$$Z_{k_G}^{\alpha}(t) \simeq \frac{I_0}{V}\sum_{i=1}^{N}\left|\hat{\mu}_i^a\right|^2\left|\hat{\mu}_i^e\right|^2\left\{\tfrac{1}{6}\exp i\left[k_G x_i(t)\right]+\tfrac{1}{4}\exp i\left[k_G x_i(t)-2\theta_i^{ae}(t)\right]\right\}. \tag{2.13}$$

Equations 2.12 and 2.13 are combined to isolate the local number density fluctuation $Z_{k_G}^{ND}(t) \equiv Z_{k_G}^{\chi}(t)+2Z_{k_G}^{\alpha}(t) \propto \frac{I_0}{V}\sum_{i=1}^{N}\left|\hat{\mu}_i^a\right|^2\left|\hat{\mu}_i^e\right|^2\exp i\left[k_G x_i(t)\right]$, and the anisotropy density fluctuation $Z_{k_G}^{AD}(t) \equiv Z_{k_G}^{\chi}(t)-2Z_{k_G}^{\alpha}(t) \propto \frac{I_0}{V}\sum_{i=1}^{N}\left|\hat{\mu}_i^a\right|^2\left|\hat{\mu}_i^e\right|^2\exp i\left[k_G x_i(t)-2\theta_i^{ae}(t)\right]$. The number density fluctuation is identical to the local concentration defined by Equation 2.1, which is well approximated by the truncated cumulant of Equation 2.4. A similar treatment of the anisotropy density leads to the approximation

$$Z_{\mathbf{k}_G}^{AD}(t) \simeq \exp\left\{i\left[k_G\bar{x}_N(t)+2\bar{\theta}_N^{ae}(t)\right]-\frac{1}{2}\left[k_G\delta\bar{x}_N(t)+2\delta\bar{\theta}_N^{ae}(t)\right]^2\right\}, \tag{2.14}$$

where the mean depolarization angle of the sampled distribution is given by $\bar{\theta}_N^{ae}(t)=\sum_{i=1}^{N}\theta_i^{ae}(t)P_N\left[\theta_i^{ae}(t)\right]$, and the variance is $\left[\delta\bar{\theta}_N^{ae}(t)\right]^2=\sum_{i=1}^{N}\left[\theta_i^{ae}(t)\right]^2P_N\left[\theta_i^{ae}(t)\right]$.

The argument of Equation 2.14 generally contains coupling terms that are proportional to $k_G^2\left[\delta\overline{x}_N(t)\right]^2\left[\delta\overline{\theta}_N^{ae}(t)\right]^2$. Such terms vanish if molecular center-of-mass positions are statistically uncorrelated with the depolarization angles. In this case, the anisotropy density fluctuation can be approximated by $Z_{\mathbf{k}_G}^{AD}(t)=Z_{\mathbf{k}_G}^{ND}(t)Z^{A}(t)$, where the anisotropy fluctuation is $Z^{A}(t)\propto\sum_{i=1}^{N}\left|\hat{\mu}_i^a\right|^2\left|\hat{\mu}_i^e\right|^2\exp i\left[2\theta_i^{ae}(t)\right]$. While both the number density and the anisotropy density fluctuations are $\mathbf{k}_G$-dependent, the anisotropy fluctuations are independent of the length scale probed.

Time-Dependent Coordinate Fluctuations, Measured by FICS. As discussed above, the FICS observables contain information about the mean and variance of the sampled distributions of fluctuating particle coordinates. Figure 2.3 illustrates schematically the relationships between hypothetical sampled distributions and their mean values, as a function of time. In Fig. 2.3A, the underlying particle distribution of center-of-mass coordinates $P_N\left[x(t)\right]$ is shown as the sum of N discreet features. A sampled distribution at one instant in time (shaded dark gray, solid outline) is compared to a sampled distribution at a later time (shaded light gray, dashed outline). If the particles can diffuse freely, then the equilibrium distribution $P_{eq}(x)$ is smooth and continuous, as shown. As

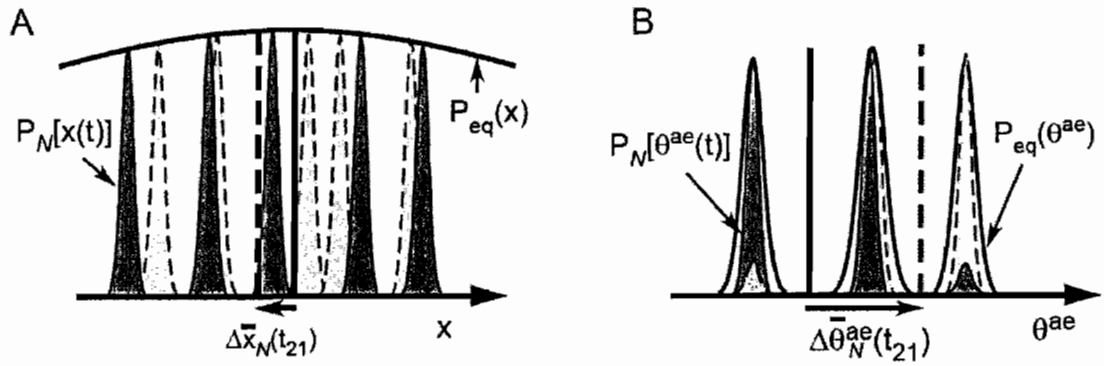

Figure 2.3. Schematic illustration of the time-dependent mean coordinate fluctuations sampled using FICS. (A) A hypothetical sampled distribution of molecular center-of-mass coordinates $P_N\left[x(t)\right]$ is depicted as a sum of $N = 5$ discreet features. The sampled distributions are shown for two distinct times, which are distinguished by dark and light gray shading. As the molecular center-of-mass coordinates fluctuate, the mean sampled coordinate $\bar{x}_N(t)$ (indicated by solid and dashed vertical lines) explores the continuous equilibrium distribution. (B) A hypothetical sampled distribution of molecular depolarization angle coordinates $P_N\left[\theta^{ae}(t)\right]$ is depicted as a sum of $N = 3$ discreet features. As in (A), dark and light gray shaded distributions indicate two distinct times. Transitions between distinct conformational states give rise to time-dependent shifts in the sampled depolarization angle coordinate $\bar{\theta}^{ae}_N(t)$ (indicated by solid and dashed vertical lines).

individual particles undergo center-of-mass displacements, the mean sampled coordinate $\bar{x}_N(t)$ (indicated by a solid and dashed vertical line) fluctuates among the possible values specified by the equilibrium distribution. By comparing FICS measurements performed at distinct times, the mean coordinate displacement $\Delta\bar{x}_N(t_{21}) = \bar{x}_N(t_2) - \bar{x}_N(t_1)$ is determined, where $t_{21} = t_2 - t_1$ is the time interval separating successive measurements. In Figure 2.3B, a hypothetical equilibrium distribution of molecular depolarization angles $P_{eq}\left(\theta^{ae}\right)$ is shown. For certain biological macromolecules, in which two coupled chromophore labels have well-defined relative orientations, the value of the

depolarization angle can reflect the internal conformation of the macromolecule. In such cases, the equilibrium distribution $P_{eq}\left(\theta^{ae}\right)$ describes the discreet set of possible conformations. The example of Figure 2.3B shows this distribution with three possible conformational states. Underlying sampled distributions $P_N\left[\theta^{ae}(t)\right]$ (shaded dark and light gray) and their corresponding mean values $\overline{\theta}_N^{ae}(t)$ (vertical solid and dashed lines) are shown for two distinct times. Comparison between successive FICS measurements allows for the determination of the mean depolarization angle displacement $\Delta\overline{\theta}_N^{ae}(t_{21})$.

Two-Point Time-Correlation Functions and Distributions. A convenient characterization of the fluctuations in equilibrium systems is given by the two-point time-correlation function (2P-TCF) $\left\langle Z^*(0)Z(t_{21})\right\rangle = \lim_{\tau\to\infty}\frac{1}{\tau}\int_0^{\tau} Z^*(t')Z(t_{21}+t')dt'$, where the angle brackets indicate the integration over time, and $t_{21} = t_2 - t_1 \geq 0$ is the time interval separating two successive measurements. The cumulant approximations of Equations 2.4 and 2.14 suggest that the number density and anisotropy density 2P-TCFs can be written, respectively,

$$C_{ND}^{(2)}(t_{21}) = \left\langle Z_{\mathbf{k}_G}^{ND*}(0)Z_{\mathbf{k}_G}^{ND}(t_{21})\right\rangle = \left\langle e^{-\frac{1}{2}k_G^2\delta\Delta\overline{x}_N^2(t_{21})}\right\rangle\left\langle e^{ik_G\Delta\overline{x}_N(t_{21})}\right\rangle, \tag{2.15}$$

and

$$C_{AD}^{(2)}(t_{21}) = \left\langle Z_{\mathbf{k}_G}^{AD*}(0)Z_{\mathbf{k}_G}^{AD}(t_{21})\right\rangle = C_{ND}^{(2)}(t_{21})\,C_A^{(2)}(t_{21}), \tag{2.16}$$

where the second term on the right side of Equation 2.16 is the anisotropy 2P-TCF:

$$C_A^{(2)}(t_{21}) = \left\langle Z^{A*}(0) Z^A(t_{21}) \right\rangle = \left\langle e^{-2\delta\Delta\bar{\theta}_N^{qe2}(t_{21})} \right\rangle \left\langle e^{i2\Delta\bar{\theta}_N^{qe}(t_{21})} \right\rangle. \tag{2.17}$$

Equation 2.15 defines the mean center-of-mass displacement $\Delta\bar{x}_N(t_{21}) = \bar{x}_N(t_{21}) - \bar{x}_N(0)$ of the sampled distribution during the time interval t_{21}, and the variance of the displacement distribution $\delta\Delta\bar{x}_N^2(t_{21}) = \left[\Delta\bar{x}_N(t_{21})\right]^2$. Similar definitions hold for the mean depolarization displacement and its variance given in Equation 2.15. Equations 2.15 – 2.17 assume statistical independence between the means and variances of the sampled distributions. The 2P-TCFs are generally complex-valued, with phase factors that depend on the mean coordinate displacements, and amplitudes that depend on the variances. These functions decay, on average, on a time scale for which the magnitude of the phase displacement exceeds $\sim \pi/4$. The number density 2P-TCF described by Equation 2.15 is known as the self-part of the intermediate scattering function employed in liquid state theory [14]. For a system of freely diffusing non-interacting molecules, this expression can be further simplified using the Gaussian model for single particle motion. Since the observation time scale is large compared to the relaxation time of the velocity autocorrelation function of molecular displacements, we may treat $\Delta\bar{x}_N(t_{21})$ as a Gaussian random variable. Equation 2.15 is then well approximated by $C_{ND}^{(2)}(t_{21}) \propto \exp\left[-k_G^2 D_S t_{21}\right]$, where D_S is the self-diffusion coefficient. Equation 2.16 suggests that we may isolate the anisotropy 2P-TCF by experimentally determining the

ratio $C_{AD}^{(2)}(t_{21})/C_{ND}^{(2)}(t_{21})$. For systems in which particle displacements are highly correlated, deviations of $C_{ND}^{(2)}(t_{21})$ from the Gaussian model behavior is a quantitative measure of the time and length scales over which correlations are important.

While 2P-TCFs convey the average time scales of molecular parameter displacements, more detailed information about the weights and magnitudes of the sampled displacements are contained in two-point distribution functions (2P-DFs). For example, the distribution $P_N^{(2)}\left[\Delta\bar{x}_N(t_{21})\right]$ is defined such that $P_N^{(2)}\left[\Delta\bar{x}_N(t_{21})\right]d\Delta\bar{x}_N$ is the probability of sampling N molecules whose mean center-of-mass has undergone a displacement in the range $\Delta\bar{x}_N$ and $\Delta\bar{x}_N + d\Delta\bar{x}_N$, during the time interval t_{21}. This distribution can be constructed by sampling pair-wise products of the form $Z_{\mathbf{k}_G}^{ND*}(0)Z_{\mathbf{k}_G}^{ND}(t_{21}) = e^{-\frac{1}{2}k_G^2\delta\Delta\bar{x}_N^2(t_{21})}e^{ik_G\Delta\bar{x}_N(t_{21})}$. From such two-point products are assembled histograms of the realizations of $\Delta\bar{x}_N(t_{21})$, weighted by the sampled inverse variance ($\propto N$). Referring to the central limit theorem, if $\Delta\bar{x}_N(t)$ behaves as a Gaussian random variable, the distribution $P_N^{(2)}\left[\Delta\bar{x}_N(t_{21})\right]$ is expected to be Gaussian and centered at $\langle\Delta\bar{x}_N\rangle = 0$. Furthermore, the variance of the sampled distribution is expected to scale linearly with time according to $\delta\Delta\bar{x}_N^2(t_{21}) = 2D_S t_{21}$, in analogy to the self-part of the van Hove correlation function [14].

The joint distribution $P_N^{(2)}\left[\Delta\bar{x}_N(t_{21});\Delta\bar{\theta}_N^{ae}(t_{21})\right]$ is related to the probability of sampling N molecules with mean depolarization angle $\Delta\bar{\theta}_N^{ae}(t_{21})$ *and* mean displacement

$\Delta\bar{x}_N(t_{21})$, during the time interval t_{21}. The joint distribution is constructed by sampling products of the anisotropy density according to: $Z^{AD*}_{\mathbf{k}_G}(0)Z^{AD}_{\mathbf{k}_G}(t_{21}) = e^{-\frac{1}{2}k_G^2\delta\Delta\bar{x}_N^2(t_{21})}e^{-2\delta\Delta\bar{\theta}_N^{ae2}(t_{21})}$ $\times e^{ik_G\Delta\bar{x}_N(t_{21})}e^{i2\Delta\bar{\theta}_N^{ae}(t_{21})} = Z^{ND*}_{\mathbf{k}_G}(0)Z^{ND}_{\mathbf{k}_G}(t_{21})\,Z^{A*}(0)Z^{A}(t_{21})$. The factorization between the parameters $\Delta\bar{x}_N(t_{21})$ and $\Delta\bar{\theta}_N^{ae}(t_{21})$ implies that $P_N^{(2)}\left[\Delta\bar{x}_N(t_{21});\Delta\bar{\theta}_N^{ae}(t_{21})\right]$ $= P_N^{(2)}\left[\Delta\bar{x}_N(t_{21})\right]P_N^{(2)}\left[\Delta\bar{\theta}_N^{ae}(t_{21})\right]$, so that the 2P-DF for the anisotropy fluctuations can be isolated from the ratio $P_N^{(2)}\left[\Delta\bar{\theta}_N^{ae}(t_{21})\right] = P_N^{(2)}\left[\Delta\bar{x}_N(t_{21});\Delta\bar{\theta}_N^{ae}(t_{21})\right]/P_N^{(2)}\left[\Delta\bar{x}_N(t_{21})\right]$.

FICS Optical Layout

Figure 2.4 shows a schematic diagram of a typical FICS apparatus. Further instrumental details are described by Fink, et al. [3]. A plane polarized, continuous wave laser beam is split into two beam paths with orthogonal plane polarization components at the entrance of a Mach-Zehnder interferometer (MZI). Within each arm of the MZI are placed an acousto-optic Bragg cell (labeled AO1 and AO2) and a variable wave plate polarization compensator. The AOs impart a time varying phase shift to their respective beams, while the variable wave plates are used to independently adjust the polarization states each beam. The two beams are brought together at the exit of the MZI, with 50% of the output used to generate the excitation grating at the sample, and the remaining light used to generate a reference signal for phase-synchronous detection and mechanical noise reduction. In order to routinely change the fringe spacing produced at the sample, the two input beams are sent through a second Sagnac interferometer. The counter-propagating

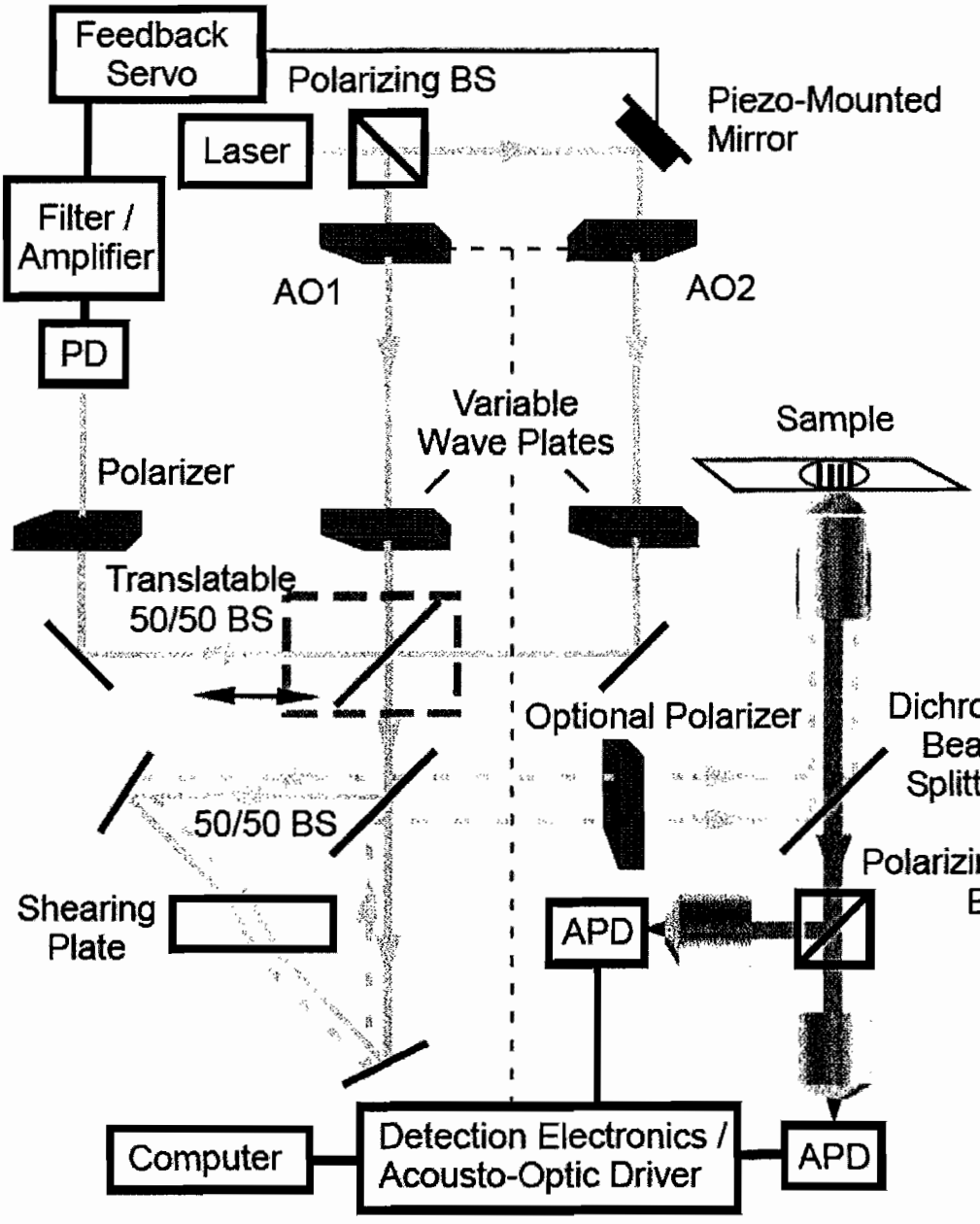

Figure 2.4. Schematic diagram of the FICS optical layout (described in text). (Abbreviations have the following meanings: APD, avalanche photo-diode; PD, photo-diode; BS, beam-splitter; AO, acousto-optic Bragg cell.) See [3] for further details.

beams travel through a shear plate, which has the effect of laterally separating the two beams. By manually adjusting the orientation of the shear plate, the incident angle of the beams at the sample can be changed, which determines the fringe spacing.

The precision of FICS measurements is limited by mechanical instabilities of the interferometers, which introduce noise in the interference pattern at the sample. To reduce mechanical noise, an active-feedback system is used to lock the phase of the optical grating in the sample (relative to that of the reference waveform) to within ~1/100 of the fringe spacing. A feedback signal, which is generated by comparing the phase of the modulated excitation intensity to that of the reference waveform, is used (via a Piezo-mounted optical mirror) to minimize the relative phase error (RPE). When the feedback circuit is engaged, fluctuations of the RPE occurs on millisecond time scales with $\langle RPE^2 \rangle^{1/2} \sim 3.9$ nm. In this case, $(3.9 \text{ nm} / d_G) \cdot 2\pi$ is the upper boundary to the precision that FICS phase measurements are sensitive.

Examples of FICS Applications

Translational Fluctuations of Mitochondria in Living Cells. FICS experiments were conducted to study mitochondrial transport in human osteosarcoma cells [5, 15], and in the budding yeast, *S. cerevisiae.* Presented below is an example for the case of yeast. MATa strains were selected for their sensitivity to alpha factor, which shifts these cells into the mating phase of the cell cycle. Mitochondria were visualized by transforming cells using the plasmid pRS316, containing DsRed.T1 fused to the COX4 leader

sequence. Cells were cultured to log phase in SD media, before treating them with 100 μM alpha factor for two hours. Cells were depleted of microfilaments by treatment with Latrunculin-A at 200 μM for a 10-minute incubation period. Samples were mounted onto a thin 3% agarose pad using SD media and 10 μM alpha factor, and sealed using valap to fuse the edges of a coverslip to the glass slide. Microtubules and/or actin microfilments were visualized by antibody staining with rat anti-α-tubulin (YOL 1/2 from clontech) or Alexa-phalloidin-542, followed with a 3.7% paraformaldehyde fixative treatment [16]. Studies of the effects of cytoskeletal inhibiting drugs on mitochondrial motility were carried out at 25°C.

To characterize the dependence of mitochondrial dynamics on cytoskeletal proteins in mating *S. cerevisiae*, cells were cultured to log phase before incubating them in 100 μM alpha factor for a period of two hours. In Figure 2.5 are shown fluorescence micrographs of typical specimens. For healthy yeast cells, mitochondrial structure is similar to that in higher organisms arrested in G1; a single interconnected network of tubular filaments constituting the reticulum morphology [15, 17] (see Figure 2.5A, left inset). The right inset of Figure 2.5A shows that the actin cytoskeleton in healthy cells is extensive and concentrated near the cell tip. Prominent features such as actin cables and patches are evident. For cells treated with the actin destabilizing agent Latrunculin-A, the mitochondrial reticulum morphology is disrupted, resulting in a population of intermediate size mitochondrial compartments (Figure 2.5B, left inset). No trace of f-actin is detected in Lat-A treated cells (Figure 2.5B, right inset).

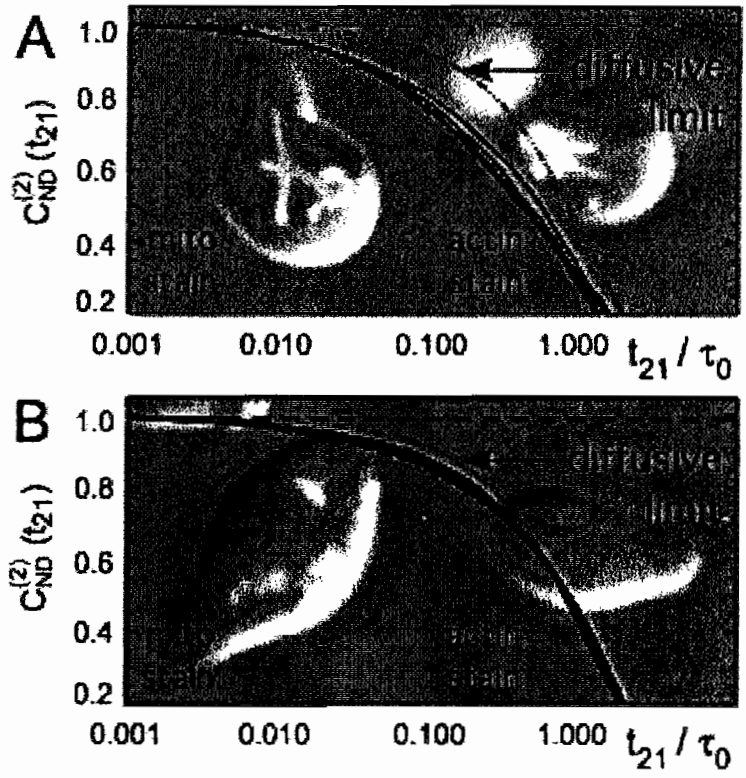

Figure 2.5. d_G-dependent two-point time-correlation functions (2P-TCFs), $C^{(2)}_{ND}(t_{21})$, for mitochondria in mating yeast cells under varying cytoskeletal conditions. The time-axes are plotted in reduced time units, t_{21}/τ_0, with $\tau_0 = \left(k_G^2 D_0\right)^{-1}$ and $D_0 = 1.8 \times 10^{-4}$ μm^2 s^{-1}. The insets show fluorescence micrographs of typical specimens on which FICS experiments were conducted. (A) The mitochondria of healthy cells appear in the reticulum morphology with an extensive actin cytotoskeleton. (B) Cells treated with Latrunculin-A appear with mitochondria disrupted into smaller compartments, and the depletion of actin microfilaments. Each panel shows decays of $C^{(2)}_{ND}(t_{21})$ for measurements performed at four different length scales: d_G = 0.6 μm, 0.79 μm, 1.03 μm, and 1.19 μm. In panel (A), the 2P-TCFs decay with increasing rate for decreasing values of d_G. In panel (B), the 2P-TCFs appear to decay independent of the value of d_G. In both panels, the dashed-dotted curves show the expected decay of a purely diffusive system with functional form $\exp\left(-t_{21}/\tau_0\right)$.

Figure 2.5 shows the decays of the 2P-TCFs $C_{ND}^{(2)}(t_{21})$ for mitochondrial displacements as a function of the reduced time variable t_{21}/τ_0, with $\tau_0 = \left(k_G^2 D_0\right)^{-1}$ and $D_0 = 1.8 \times 10^{-4}\,\mu m^2\,s^{-1}$. By plotting our data in this way, the 2P-TCFs are rescaled to eliminate length scale dependent contributions from random diffusion. For a system of independent Brownian particles, the 2P-TCFs measured at different length scales would all fall upon a single universal curve of the form $\exp\left(-t_{21}/\tau_0\right)$. We may thus compare the length scale dependent differences in mitochondrial mobility due to the influence of cytoskeletal proteins. In panel (A) we plot the 2P-TCFs for healthy cells, and in panel (B) we plot those for cells depleted of microfilaments. From the results shown in panel (A), we see that the TCF's do not lie on a single universal curve, indicating that mitochondria in healthy cells exhibit a length-scale dependent mobility beyond the effects of simple diffusion. The TCF corresponding to $d_G = 1.19\ \mu m$ appears to decay more slowly than for those with $d_G = 0.60\ \mu m$ and $d_G = 0.79\ \mu m$, suggesting a trend of decreasing mobility with increasing length-scales. For cells depleted of microfilaments (B), the length scale dependence of the 2P-TCFs vanishes almost completely. These data are compared to the single exponential decay $\exp\left(-t_{21}/\tau_0\right)$, corresponding to a simple diffusive limit, with time constant τ_0 approximating the $1/e$ time of the data shown in panel (B). We further compare this diffusive limit to data for healthy cells, shown in panel (A). It is noteworthy that the value used for D_0 is the same as that previously obtained in similar experiments conducted on G1 arrested osteosarcoma cells, which were treated with microfilament and

microtubule destabilizing agents [5]. This suggests that the intracellular environment experienced by mitochondria in the absence of microtubules and microfilaments is quite similar for yeast as for osteosarcoma cells.

Translational / Conformational Fluctuations of the Fluorescent Protein DsRed in Solution. FICS has been applied to study center-of-mass diffusion [3], and slow polarization fluctuations resulting from the conformational transitions of DsRed, a multicolored fluorescent protein derived from the coral *Discosoma sp* [4, 13]. Fluorescent proteins are widely used in biotechnological applications as reporters of gene expression and other singular events of cell activity [18]. It has been hypothesized that fluorescent proteins from reef-building corals function in an adaptive mechanism to optically interact and to regulate the symbiotic relationship between corals and photosynthetic algae [19]. It is therefore interesting to examine in some detail the conformational transitions that affect the protein's ability to transfer optical excitation energy and to undergo fluorescence efficiently. DsRed has an exceptionally high extinction coefficient ($\varepsilon = 3 \times 10^5$ cm^{-1} M^{-1}, $\lambda_{ex} \sim 532$ nm), orange-red emission that is easily separated from excitation light, and a high fluorescence quantum yield ($q_f = 0.79$) [20].

In the following are presented FICS measurements of slow (~ 8 s) anisotropy fluctuations resulting from changes in the incoherent dipolar coupling between the adjacent chromophore sites of DsRed, which is a tetrameric complex of fluorescent protein subunits [21]. The cylinder-shaped subunits of the complex each contain an optical chromophore, with relative orientation of the transition dipole moments rigidly

fixed. The DsRed molecules are free to diffuse in 95% glycerol / water solution. On the time scale of the fluorescence lifetime ($\tau_f \simeq 3.2$ ns) [22], rotational diffusion is very slow ($\tau_R \geq 100$ ns), so that the rate of fluorescence depolarization is not affected by molecular rotation. However, fluorescence depolarization is strongly influenced by intra-molecular energy transfer [22]. Because the relative distances and orientations between adjacent transition dipoles are small, an excited chromophore site can transfer its energy to one of its unexcited neighbors by a Förster dipole-dipole mechanism. When two sites in the DsRed complex are coupled, the excited state polarization rotates by the angle θ^{ae}, which subtends the absorption dipole moment of the initially excited chromophore and the emission dipole moment of the emitting chromophore. Similar to the behavior of the green fluorescent protein (GFP), the individual fluorescent protein subunits of DsRed can undergo so-called 'flickering' transitions between 'bright' and 'dark' states [23, 24]. A locally resonant site (*i.e.*, a 'bright' site) can reversibly interconvert to a non-resonant ('dark') site. As local sites flicker between 'bright' and 'dark' states, the populations of distinct pair-wise coupled conformations are also expected to fluctuate, leading to fluctuations of the polarized fluorescence.

In Figure 2.6 are shown experimental trajectories of $Z_{\mathbf{k}_G}^{ND}(t)$ and $Z_{\mathbf{k}_G}^{AD}(t)$, constructed from the polarized signals, with $d_G = 2.12$ μm. These data represent the final 100 seconds of an acquisition performed at a sampling rate of 1 kHz, and over a duration of 512 s. In the left column are shown the real and imaginary parts of the number density fluctuation; the top panel shows an expanded time axis, corresponding to a 1 s interval. In the right column are shown the real and imaginary parts of the

anisotropy density fluctuations. Both $Z_{\mathbf{k}_G}^{ND}(t)$ and $Z_{\mathbf{k}_G}^{AD}(t)$ exhibit rapid sub-second fluctuations, while the anisotropy density contains at least one additional, slow variation on the time scale of a few seconds.

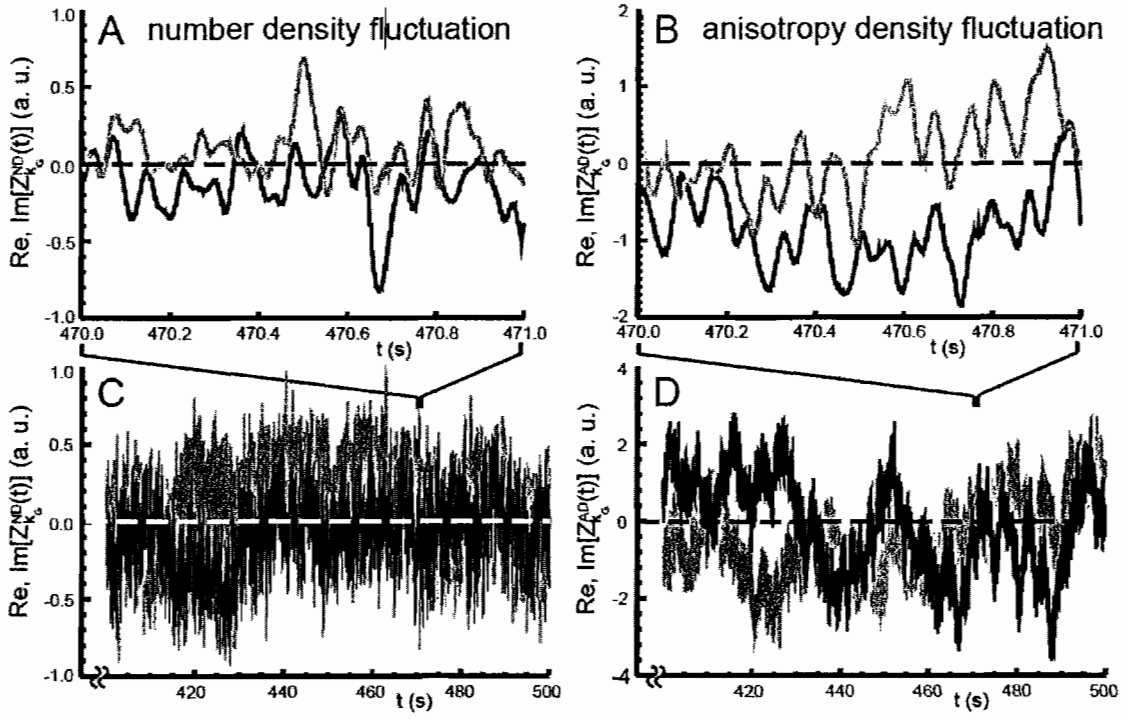

Figure 2.6. Experimental trajectories of the number density fluctuation $Z_{\mathbf{k}_G}^{ND}(t)$ and the anisotropy density fluctuation $Z_{\mathbf{k}_G}^{AD}(t)$, constructed from demodulated polarized fluorescence signals, with $d_G = 2.12\ \mu\text{m}$. These measurements were recorded from a 10 nM solution of DsRed in 95% glycerol / water, at a frequency of 1 kHz, and over an acquisition period of 512 s. In panels (C) and (D), the final 100 seconds of the data run are shown. In panels (A) and (B), the time axis is expanded to show the variation over a 1 second time window. In each panel, the two signal quadratures, $\phi_G = 0,\ \pi/2$, are plotted in black and gray, respectively.

From the experimental trajectories are calculated the normalized TP-TCFs $C_{ND}^{(2)}(t_{21})$ and $C_{AD}^{(2)}(t_{21})$, defined by Equations 2.13 and 2.14, respectively. These are shown in Figures 2.7A and 2.7B, displaced vertically for the five different fringe spacings d_G = 1.6, 1.75, 2.12, 2.56, and 2.92 μm. In Figure 2.7A are compared results for $C_{ND}^{(2)}(t_{21})$ (black) to the Gaussian model for single particle diffusion described by $\exp(-k_G^2 D_S t_{21})$ (white). For these calculations a self-diffusion coefficient of $D_S = 3.7 \times 10^{-10}$ cm^2 s^{-1} is used that is consistent with previous measurements of DsRed self-diffusion in 95% glycerol / water solution [3]. For each of the five values of d_G investigated, the time constants of the decays increase with increasing length scale, and the data are well described by the Gaussian model. This is the expected result, since the average separation between DsRed molecules is ~ 1 μm, and molecular interactions are unlikely to cause deviations from random center-of-mass motion. The assumption of statistical independence between the sampled mean center-of-mass displacement $\Delta\bar{x}_N(t_{21})$ and the mean displacement of the depolarization angle $\Delta\bar{\theta}_N^{ae}(t_{21})$ is tested by comparing the results for $C_{AD}^{(2)}(t_{21})$ to model decays, which account for the factorization described by Equation 2.14. For this purpose, a single exponential decay $\exp(-t_{21}/\tau_A)$ is used to represent the average loss of polarization memory described by the anisotropy 2P-TCF $C_A^{(2)}(t_{21})$. Figure 2.7B compares measurements of $C_{AD}^{(2)}(t_{21})$ to the model decay $\exp\left[-\left(k_G^2 D_S + 1/\tau_A\right)t_{21}\right]$, with τ_A = 8 s. Note that the functions $C_{AD}^{(2)}(t_{21})$ decay more rapidly in time than do the functions $C_{ND}^{(2)}(t_{21})$, as the model decays suggest, and that the

agreement between the data and the model curves is very good for all values of d_G. Figure 2.7C shows a comparison between the ratio of the decays shown in Figures 2.7A and 2.7B, $C_{AD}^{(2)}(t_{21})/C_{ND}^{(2)}(t_{21}) = C_A^{(2)}(t_{21})$, to the model function $\exp(-t_{21}/\tau_A)$. The agreement between the experimental results for $C_A^{(2)}(t_{21})$ and the single-exponential decay, for all values of d_G, demonstrates a clear and unambiguous separation between anisotropy and center-of-mass fluctuations. The value obtained for the relaxation time τ_A = 8 s suggests that this is the slowest time scale for internal conformational fluctuations of DsRed. Because the decays of $C_A^{(2)}(t_{21})$ are independent of d_G, these measurements demonstrate a clear and unambiguous separation between the anisotropy and the center-of-mass fluctuations of the DsRed system.

Figure 2.8 shows two-point distribution functions (2P-DFs) of the mean sampled displacement of the center-of-mass $P_N^{(2)}\left[\Delta\bar{x}_N(t_{21})\right]$, and the depolarization angle $P_N^{(2)}\left[\Delta\bar{\theta}_N^{ae}(t_{21})\right]$. The 2P-DFs are constructed from the FICS measurement trajectories $Z_{\mathbf{k}_G}^{ND}(t)$ and $Z_{\mathbf{k}_G}^{AD}(t)$. In each panel, the distributions are vertically displaced for three different values of the time interval t_{21}. The sampled distributions are symmetric and centered about the origin, and their widths increase as a function of t_{21}. In Figure 2.8A, the sampled distribution $P_N^{(2)}\left[\Delta\bar{x}_N(t_{21})\right]$ is compared to the self-part of the van Hove correlation function $G_S(\Delta\bar{x}_N, t_{21}) = (4\pi D t_{21})^{-3/2}\exp(-\Delta\bar{x}_N^2/4D_S t_{21})$ (dashed gray curves), where the value of D_S is the same as that used for the previous comparison between the

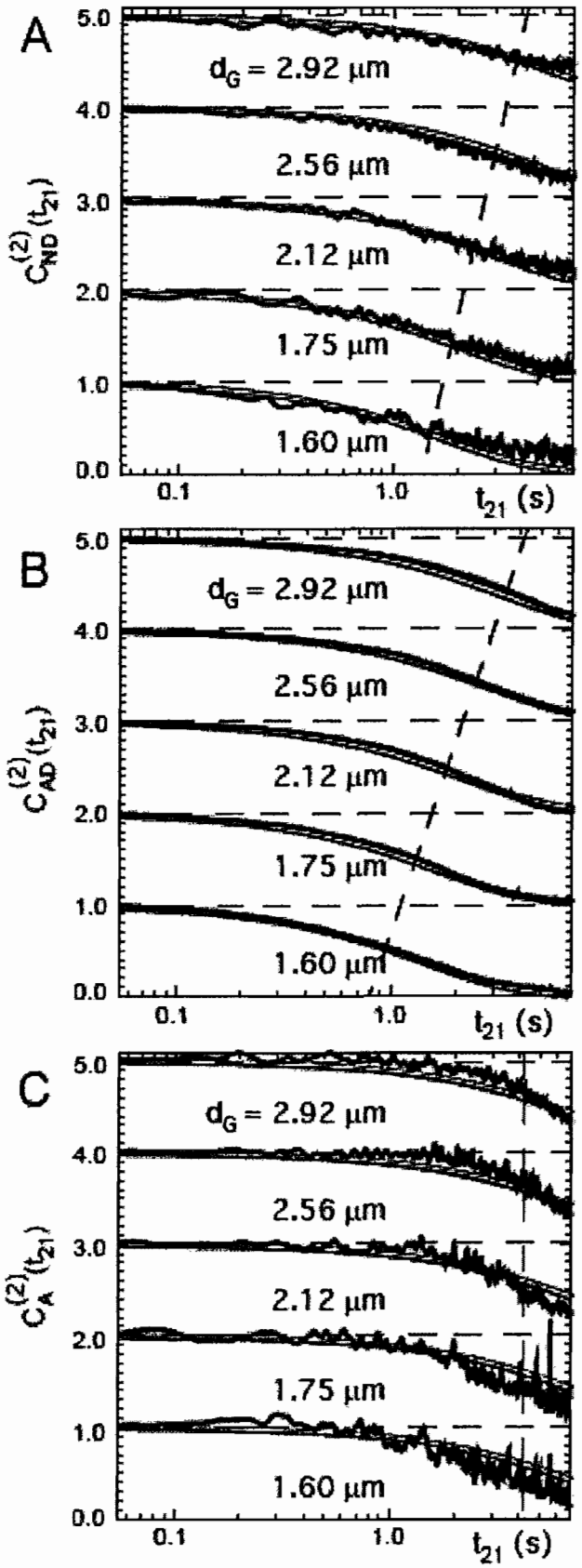

Figure 2.7. d_G-dependent two-point time-correlation functions (2P-TCFs) of the number density and the anisotropy density fluctuations, $C^{(2)}_{ND}(t_{21})$ and $C^{(2)}_{AD}(t_{21})$, respectively. Decays corresponding to different values of the fringe spacing d_G are vertically displaced. Diagonal and vertical dashed lines are guides to the eye to roughly indicate the decay time scale. In panel (A), we compare $C^{(2)}_{ND}(t_{21})$ to the Gaussian model for Fickian diffusion $\exp(-k_G^2 D_S t_{21})$, where $D_S = 3.7 \times 10^{-10}$ cm^2 s^{-1}. In panel (B), we compare $C^{(2)}_{AD}(t_{21})$ to the function $\exp\left[-\left(k_G^2 D_S + 1/\tau_A\right) t_{21}\right]$, where τ_A = 8 s is the average time scale of the anisotropy decay, due to intra-molecular energy transfer. In panel (C), we compare the ratio of the data shown in panels (A) and (B), $C^{(2)}_{A}(t_{21}) = C^{(2)}_{AD}(t_{21})/C^{(2)}_{ND}(t_{21})$, to the model decay $\exp(-t_{21}/\tau_A)$.

number density 2P-TCF and the Gaussian model decays. The agreement between the van Hove function and the 2P-DF provides further support that the Gaussian model is an accurate picture of molecular self-diffusion in the DsRed system. It is important to emphasize that the comparison between theory and measurement at the level of the DFs is a more accurate test of the underlying model than the previous comparison at the level of the 2P-TCFs. This is because the TP-TCFs represent a statistical average over the distribution of sampled displacements, according to $C_{ND}^{(2)}(t_{21}) = \int_{-\infty}^{\infty} e^{-\frac{1}{2}k_G^2 \delta\Delta\bar{x}_N^2(t_{21})} e^{ik_G\Delta\bar{x}_N(t_{21})} \times P_N^{(2)}\left[\Delta\bar{x}_N(t_{21})\right] d\Delta\bar{x}_N(t_{21})$. It is therefore possible to probe dynamical information that is often obscured in conventional measurements by examining the 2P-DFs directly. In Figure 2.8B is shown the 2P-DF of the mean depolarization angle $P_N^{(2)}\left[\Delta\bar{\theta}_N^{ae}(t_{21})\right]$. This distribution is isolated from the joint distribution of the anisotropy density $P_N^{(2)}\left[\Delta\bar{x}_N(t_{21}); \Delta\bar{\theta}_N^{ae}(t_{21})\right]$ by factoring out translational contribution. This distribution is also roughly Gaussian, and its width broadens on time scales less than 70 ms.

Conclusions

The movement and redistribution of intracellular species is an essential part of normal cell function. Such processes involve transport and interactions between myriad biochemical species over a broad range of spatial and temporal scales. Measurements that

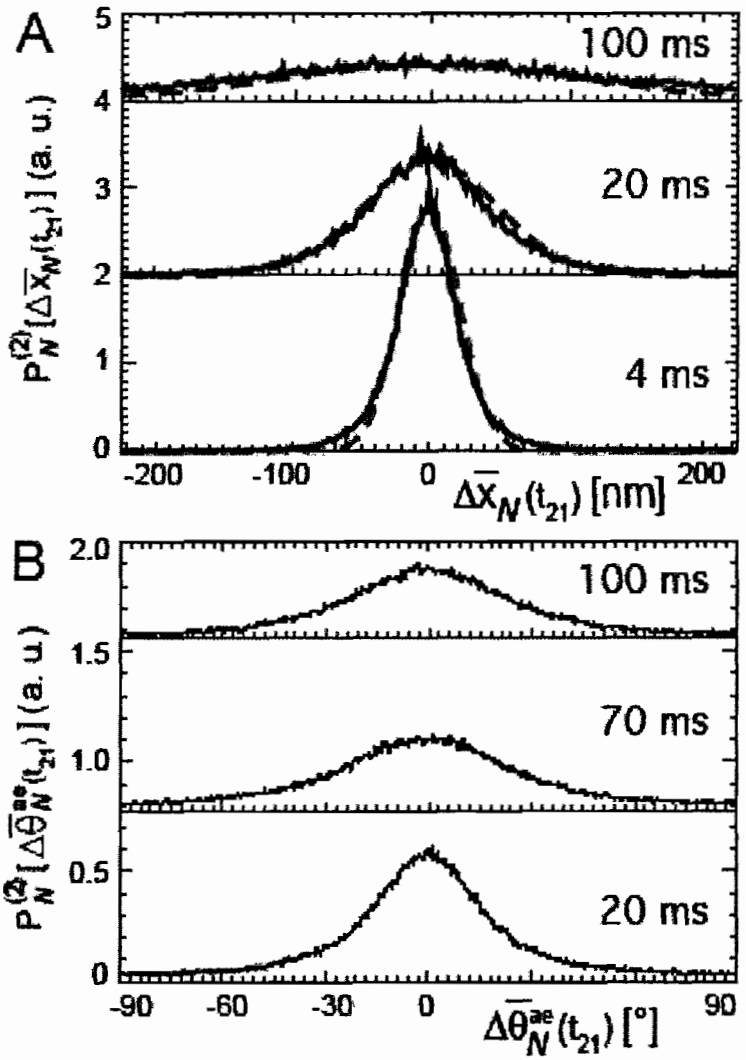

Figure 2.8. Two-point distribution functions (2P-DFs) of (A) the mean sampled center-of-mass displacement $P_N^{(2)}\left[\Delta\bar{x}_N(t_{21})\right]$, and (B) the mean sampled displacement of the depolarization angle $P_N^{(2)}\left[\Delta\bar{\theta}_N^{ae}(t_{21})\right]$. In each panel, we show the distributions vertically displaced for three different time intervals. In panel (A), we compare our measured distribution $P_N^{(2)}\left[\Delta\bar{x}_N(t_{21})\right]$ (black) to the self-part of the van Hove correlation function $G_S(\Delta\bar{x}_N, t_{21}) \propto \exp\left(-\Delta\bar{x}_N^2/4D_S t_{21}\right)$ with $D_S = 3.7 \times 10^{-10}$ cm^2 s^{-1}, which assumes that molecular self-displacements occur by Fickian diffusion (gray dashed curves).

provide information about the microscopic details of intracellular processes can help to resolve mechanisms of biological activity.

Few current methods provide detailed microscopic information about intracellular chemical processes. The low signal limitations of existing methods place constraints on the number of studies that are possible. Fourier imaging correlation spectroscopy (FICS) is a novel fluorescence fluctuation method that achieves enhanced signal levels by spatially integrating over a relatively large sample volume, while retaining microscopic information by imprinting particle center-of-mass coordinates onto an optical signal phase. When employed in a polarization selective optical geometry to suspensions of fluorescent molecules, the FICS approach is suitable to study the internal conformation fluctuations in the presence of molecular diffusion. The phase-selectivity of FICS measurements enables the determination of time correlation functions and probability distributions, which provide detailed information about the time scales and the weighted magnitudes of molecular coordinate displacements, respectively. A straightforward extension of this approach developed in chapter IV involves analyses based on four-point correlation functions and two-dimensional joint probability distributions [13, 25]. These two-dimensional analyses will be useful to decompose the dynamics of heterogeneous systems into their various dynamical components, and to provide in-depth information about the microscopic mechanism of biomolecular conformational transitions.

Although the FICS approach has so far been applied only to fluorescent proteins, it has the potential to be valuable for general studies of conformational transitions in fluorescently labeled proteins and nucleic acid systems. The breadth of information

provided by such measurements would test fundamental models of bio-molecular dynamics, as well as enable new studies of enzymatic function in living cells.

CHAPTER III

ACTIN ASSEMBLY DRIVEN MITOCHONDRIAL DYNAMICS IN MATING *S. CEREVISIAE*

In chapter II the method behind a FICS experiment on yeast cell mitochondria was introduced along with preliminary results demonstrating what sort of impact microfilament organization has on the dynamics of the organelle. Here we interpret these results with the mean square displacement providing the framework of our analysis. By also examining the effects of actin-related mutants, we address possible mechanisms of the anomalous diffusion of mitochondria in healthy cells. Our results are consistent with a model in which mitochondrial motions are mediated by a nucleation and growth mechanism involving filamentous actin assembly. The work with actin mutants act1-V159N and Arc18pΔ was made possible through the generosity of L. Pon.

Background

The intracellular environment is a dynamic, multi-component fluid, with relaxations spanning a broad range of length and time scales. An accurate molecular level

understanding of intracellular transport must account for the myriad chemical species and physical processes at play. In cells, thermally generated inertial forces give rise to stochastic particle displacements, which are characterized by the mean-square-displacement (MSD). For a spatially homogeneous fluid, the MSD scales linearly in time, i.e., $\mathrm{MSD} \propto \tau^{\alpha}$, with $\alpha = 1$ [1]. However, the microscopic heterogeneity of the intracellular environment is thought to result in anomalous particle motion [2-4]. For example, a small protein or larger particle may become 'trapped' or 'caged' during extended periods of intermittent mobility. Such anomalous motion often leads to sub-diffusive scaling of the MSD, with $\alpha < 1$.

A growing body of research has identified both normal and anomalous diffusion of intracellular species. The motions of small proteins in bacteria, for example, appear to be diffusive [5-7]. These findings contrast with observations that the motions of larger mRNA-protein clusters in E. coli, as do the motions of yolk granules in yeast, appear to be sub-diffusive [3, 4]. The apparent differences in the dynamics of various intracellular species and host organisms may be reconciled by accounting for the size of the mobile particles relative to a structural length scale associated with the cytoplasmic environment [8]. In this picture, anomalous diffusion is a measure of the tendency of particles to be hindered by the obstacles comprising the crowded intracellular space.

An alternate picture arises from recognition that the cell is also host to self-assembling cytoskeletal proteins, such as actin, which can produce physical forces as the polymers grow [9]. The assembly of branched actin networks, for example, are an underlying molecular mechanism of cell motility [10]. Should a sub-cellular object

directly experience the fluctuating forces of actin network assembly and disassembly, one might expect it to exhibit anomalous, intermittent motions that are best characterized as sub-diffusive. Thus, an undetermined combination of thermal diffusion, macromolecular crowding, and actin network dynamics can potentially mediate the transport of intracellular species. In this work, we address the question of whether the fluctuating forces due to actin network assembly are germane to the cell environment, and in particular how they affect the motions of a ubiquitous sub-cellular object, the mitochondrion.

Mitochondria are well known for their role in intracellular ATP production, heme and fatty-acid biosynthesis, and programmed cell death [11-13]. They are also known to exhibit complex intracellular motions [14]. Microscopy studies reveal that mitochondria undergo transformations between different morphologies, which occur by a combination of fusion and fission events and membrane redistribution. A prominent feature of mitochondrial dynamics is the continuous shape changes and positional fluctuations of the membrane [15, 16]. For many years, biologists have sought to understand the significance of these motions in terms of the protein machinery responsible for sub-cellular organization [14]. This question addresses key issues of how cells regulate their metabolic states, and how they coordinate the delivery of mtDNA to their progeny. The local redistribution of mitochondria to sites of fluctuating ATP consumption is arguably a means for the cell to override the diffusive barriers of the crowded intracellular space [17]. On the other hand, global transport and segregation of mitochondria to daughter cells is an important feature of mtDNA inheritance [18, 19].

A molecular genetics approach to study cytoskeletal activity is to compare mutant cell lines to their wild-type parents. Because of the availability of yeast genetic mutants, *S. cerevisiae* is a useful organism to probe the mechanism of mitochondrial dynamics. In mammalian cells, mitochondrial motion depends on both microtubules (MTs) and microfilaments (MFs) [16]. The broad distribution of relaxation times observed in mammalian cells suggests a complex regulatory system that involves multiple species of structural proteins [15, 16]. In yeast, it has been demonstrated that the polarized movement of mitochondria from a parent cell to its daughter bud requires only an intact actin cytoskeleton [20-22]. Related studies of budding yeast have revealed a number of mitochondrial membrane and actin associated proteins required for polarized mitochondrial movement. These studies suggest that the polarized mitochondrial transport mechanism might involve an Arp2/3-mediated actin network assembly process [22-24].

In this work, we study the influence of the dynamic intracellular environment on the motion of mitochondria. By comparison to cells with inhibited cytoskeletal activity, we isolate the effects of specific protein components on mitochondrial movement. We examine conditions in which the actin and tubulin cytoskeletons are grossly disrupted (using pharmacological agents), in addition to more subtle interferences induced by mutations (see Table 1). Our previous studies of osteosarcoma cells revealed that mitochondrial movement depends on the normal function of both the actin and tubulin cytoskeletons [16]. Nevertheless, those studies did not establish the relative importance of the two cytoskeletons to the mechanism of mitochondrial motion. It is possible that

local contacts between the actin and tubulin cytoskeletons, present in osteosarcoma cells, could indirectly influence mitochondrial mobility. This issue is clarified through studies of the more primitive yeast cells, in which the concentration of cytoplasmic MTs is much lower than in osteosarcoma cells.

Strain number	Genotype	Source
MYY290	MATa, his3Δ1, leu2Δ0, ura3Δ0	(Smith and Yaffe, 1991)
DDY1493	MATa, act1-V159N::HIS3, his3Δ1, tub2Δ0, ura3Δ0, lue2Δ0	(Belmont and Drubin, 1998)
DDY1495	MATa, ACT1::HIS3, his3Δ1, tub2Δ0, ura3Δ0, lue2Δ0	(Belmont and Drubin, 1998)
BY4741	MATa, his3Δ1, leu2Δ0, ura3Δ0, met15Δ0	(Open Biosystems, Huntsville, AL)
YSC1021-555365	MATa, arc18Δ;;kanMX, his3Δ1, leu2Δ0, ura3Δ0, met15Δ0	(Open Biosystems, Huntsville, AL)

Table 3.1. Strains used in this study.

Our studies employ Fourier imaging correlation spectroscopy (FICS) to observe the length scale dependent dynamics of fluorescently labeled yeast mitochondria. FICS is a high precision, interferometric approach to measure the spatial fluctuations of fluorescent objects over a broad range of temporal scales [15, 16, 25, 26]. Using FICS, we determine the time correlation functions $F(k,\tau)$, which indicate a loss of structural memory measured against an experimentally adjustable length scale d_G (with wavenumber $k = 2\pi/d_G$). The time correlation functions provide the MSD, from which we identify short and long time diffusive regimes, separated by a transient period of sub-diffusive behavior. Both short- and long-time diffusive motions may be related to the microscopic interactions between mitochondria and its local environment.

Results

Mitochondrial Dynamics in Mating S. cerevisiae Are Sub-Diffusive on Intermediate Time Scales and Are Strongly Coupled to Actin. To characterize the dependence of mitochondrial dynamics on cytoskeletal proteins in mating *S. cerevisiae*, we cultured cells to log phase before incubating them in 100 μM alpha factor for a period of two hours. In Figure 3.1, we show fluorescence micrographs of typical specimens. For all of the cases we studied, we observe the "shmoo" protrusion, characteristic of cells arrested in the mating state. For healthy yeast cells, mitochondrial structure is similar to that in higher organisms arrested in G1. We observe a single interconnected network of tubular filaments constituting the reticulum morphology [15, 16] (see Figure 3.1A). Figures 3.1B,

3.1D, and 3.1F show the results of Alexa-phalloidin-542 labeling of actin filaments in fixed cells (see Methods). Figure 3.1B shows that the actin cytoskeleton in healthy cells is extensive and concentrated near the shmoo tip. Prominent features such as actin cables and patches are evident. For cells treated with the microtubule-destabilizing agent Nocodazole, both mitochondrial morphology (Figure 3.1C) and actin filament integrity (Figure 3.1D) appear to be unaffected. In contrast, the actin cytoskeleton of cells treated with Latrunculin-A appears depleted. In this case, the mitochondrial reticulum morphology is also disrupted, resulting in a population of intermediate size mitochondrial compartments (Figure 3.1E). Our phalloidin labeling procedure reveals no trace of f-actin in Latrunculin-A treated cells (Figure 3.1F).

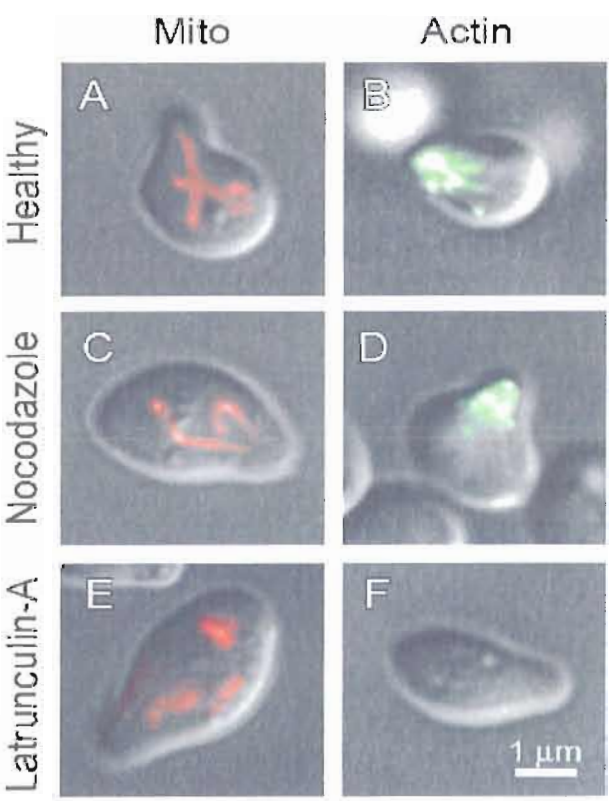

Figure 3.1. Micrographs of fluorescently labeled yeast mitochondria (left column, red) and MFs (right column, green), under different cytoskeletal conditions. (A) & (B) The mitochondria of healthy cells appear in the reticulum morphology with an extensive actin cytotoskeleton. (C) & (D) Treatment with the microtubule destabilizing agent Nocodazole leaves both the reticulum structure and the actin cytoskeleton intact. (E) & (F) Treatment with Latrunculin-A results in the mitochondria breaking up into smaller compartments, and the depletion of actin MFs.

In Figure 3.2, we compare results for mitochondrial fluctuations in healthy cells (MYY290, black curves) to cells treated with MT destabilizing Nocodazole (blue) and to cells treated with MF destabilizing Latrunculin-A (green). We directly compute from our data the density time correlation function $F(k,\tau)$, and we subsequently determine $\ln\left[1/F(k,\tau)\right]$ (see Methods). When presented on a log-log plot, these curves are proportional to the MSD $\left\langle \Delta r^2(\tau)\right\rangle = 6D\tau^{\alpha}$ according to $\gamma \ln k + \ln\left\langle \Delta r^2(\tau)\right\rangle = \gamma \ln k + \ln D + \alpha \ln \tau$. In principle, each curve is the sum of two contributions; a term that is linear with respect to $\ln\tau$ with slope α, and an offset $\gamma \ln k + \ln D$. We focus on the dependence of the temporal scaling exponent α on cytoskeletal integrity. Such scaling is known to reflect local caging interactions in polymer solutions [27]. Figure 3.2 shows four sets of curves (vertically displaced by factors of 10), with each curve corresponding to one of the fringe spacings d_G = 0.6, 0.79, 1.03 and 1.19 μm. We note that these data span three orders of magnitude in time, and that it is possible to discern a characteristic shape. At short times, the curves appear to scale as α = 1, followed by an intermediate sub-diffusive regime with α = 2/3. At long times, the curves crossover to α = 1. For MT inhibited cells, the behavior is very similar to that of healthy cells, indicating that the dynamics of the local environment are unaltered. For cells in which MFs are destabilized, the characteristic shape of the MSD persists; however, the time window during which sub-diffusive behavior occurs is shifted to shorter times. We further note that for MF

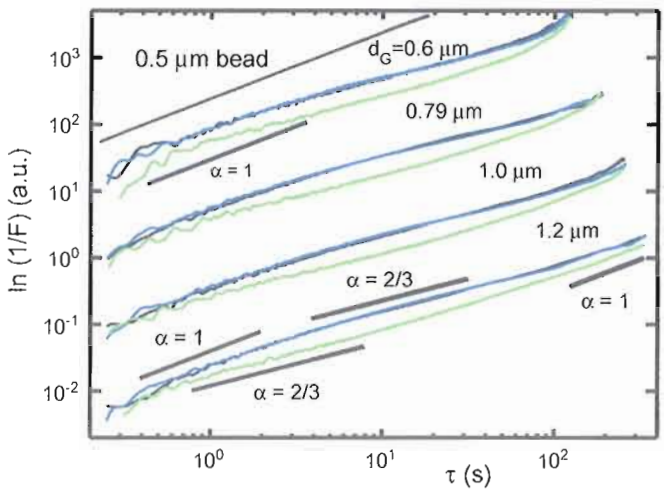

Figure 3.2. $\ln\left[1/F\left(k,\tau\right)\right]$ plots of mitochondrial fluctuations in healthy cells (black curves), cells treated with the f-actin inhibitor Latrunculin-A green curves), and cells treated with the microtubule inhibitor Nocodazole (blue curves). Each set of curves represents measurements performed at a different length scale d_G =0.6 μm, 0.79 μm, 1.03 μm and 1.19 μm. For all of the length scales investigated, cells treated with Latrunculin-A show a pronounced decrease in mitochondrial mobility. FICS data of a 0.5 μm colloid sample in viscous, concentrated sorbitol solution is presented in the top of the figure. Various lines with slopes representing the time scaling parameter α are also provided to guide the eye.

destabilized cells, the magnitude of the MSD is diminished in comparison to healthy cells for all of the length scales investigated. These data show that mitochondrial displacements in yeast are sub-diffusive over a broad range of time scales, and are sensitive to the integrity of the actin MFs, but much less sensitive to MTs. To assess the degree to which mitochondria are able to move around their environment during long (70 sec.) and short (.7-1 sec.) periods of time, we define the effective diffusions as $\tilde{D} = \ln\left[F\left(k,\tau\right)\right]/\tau k^2$ and present these for healthy and Latrunculin-A treated cells in Table 3.2. The effective diffusion coefficients corroborate the significant decrease in movement of Latrunculin-A treated mitotochondria observed in the MSD data.

	Healthy		Latrunculin-A	
Fringe Size (μm)	$\tilde{D}$ (cm^2 sec^{-1}) / 10^{-12} (time:0.7-1sec)	$\tilde{D}$ (cm^2 sec^{-1}) / 10^{-12} (time:70sec)	$\tilde{D}$ (cm^2 sec^{-1}) / 10^{-12} (time:0.7-1sec)	$\tilde{D}$ (cm^2 sec^{-1}) / 10^{-12} (time:70sec)
0.60	7.75	2.49	5.36	1.72
0.78	8.18	2.64	6.13	1.78
1.03	9.41	3.01	7.34	1.91
1.19	8.35	2.97	6.25	1.97

Table 3.2. Effective diffusion coefficients of mitochondria in healthy cells and cells treated with Latrunculin-A

The Magnitude of Mitochondrial Displacements Are Enhanced in the Actin Mutation ActV159N and Suppressed in the Deletion Mutation Arc18pΔ of the Arp2/3 Complex.

Our observations implicating the actin cytoskeleton in mitochondrial motion led us to compare the behavior of wild-type cells to cells containing mutations of proteins participating in actin assembly (see Methods and Table 3.1). In Figure 3.3, we compare results from the actin mutant strain act1-V159N (light gray) to those of its wild-type parent (black), which were measured at the elevated temperature of 36°C. Similar to drug-treated cells, the MSD for mutant cells exhibit nearly the same characteristic shape showing short and long time diffusive regimes, separated by an intermediate sub-diffusive regime. The act1-V159N strain is a temperature sensitive mutation, whose cell culture growth rate is suppressed at the elevated temperature of 36°C. At room temperature (22°C), the growth rate of the mutant strain appears normal, and is indistinguishable from its wild-type parent (data not shown). At the elevated temperature,

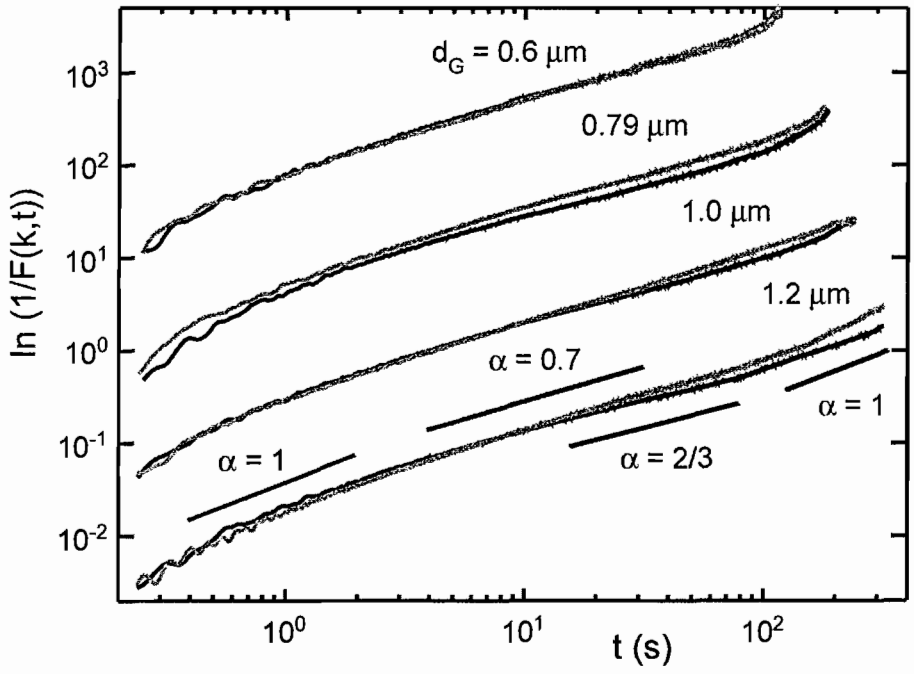

Figure 3.3. Comparison between $\ln\left[1/F(k,\tau)\right]$ plots of mitochondrial fluctuations for the temperature-sensitive actin mutant strain act1-V159N (DDY1493, gray curves), and its wild-type parent ACT1 (DDY1495, black curves), measured at the non-permissive temperature 36° C. Each set of curves corresponds to the length scale indicated. On the longer length-scalses 0.79 μm, 1.03 μm and 1.19 μm, there is a significant increase in the mobility of act1-V159N mitochondria, in comparison to wild-type cells.

we observe a distinct separation and enhancement of the dynamics for act1-V159N, in comparison to wild-type mitochondria at long times and for $d_G \geq 0.79$ μm. This separation appears to vanish when we decrease the sample temperature to 22°C (data not shown). Table 3.3 shows that the effective diffusion for mitochondria at short and long times for the $d_G = 0.79$ μm length scale experiment is marginally higher in the mutant than the wild-type.

	Wild-type		act1-V159N	
Fringe Size (μm)	$\tilde{D}$ (cm^2 sec^{-1}) / 10^{-12} (time:0.7-1sec)	$\tilde{D}$ (cm^2 sec^{-1}) / 10^{-12} (time:70sec)	$\tilde{D}$ (cm^2 sec^{-1}) / 10^{-12} (time:0.7-1sec)	$\tilde{D}$ (cm^2 sec^{-1}) / 10^{-12} (time:70sec)
0.60	7.05	2.70	7.32	2.57
0.78	6.73	2.34	7.48	2.97
1.03	7.84	2.78	7.73	3.41
1.19	7.00	2.31	6.13	2.90

Table 3.3. Effective diffusion coefficients of mitochondria in wild-type parent DDY-1495 cells and act1-V159N mutant DDY-1493.

Unlike our results for the drug treated cells, the act1-V159N cells show no evident shift of time scale over which sub-diffusive behavior occurs. We point out that our *in vivo* observations of enhanced mitochondrial motion for the mutant act1-V159N are consistent with the actin polymerization model, since similar results are reported for *in vitro* studies of actin polymerization involving the act1-v159n protein [28]. Wen et al. observed enhanced polymerization rates of yeast act1-v159n protein in the presence of the actin filament nucleation complex Arp2/3.

Because our findings implicate actin polymerization as a driving force of mitochondrial motion, we next asked how regulatory complexes of f-actin might influence these same processes. The Arp2/3 complex is a regulator of actin polymerization and dendritic network growth [10, 29]. We therefore chose the Arp2/3 complex as the next candidate to investigate the effects of actin cytoskeletal mutants on mitochondrial motion. We selected the deletion mutation Arc18pΔ to the ARC18 gene, which expresses a constituent protein of the Arp2/3 complex [30]. Cells with this mutation appear to grow in culture at a reduced rate, in comparison to cells of the wild-

type parent strain. In Figure 3.4, we compare our results for the mutant Arc18pΔ cells (light gray) to those of the wild-type parent ARC18 (black).

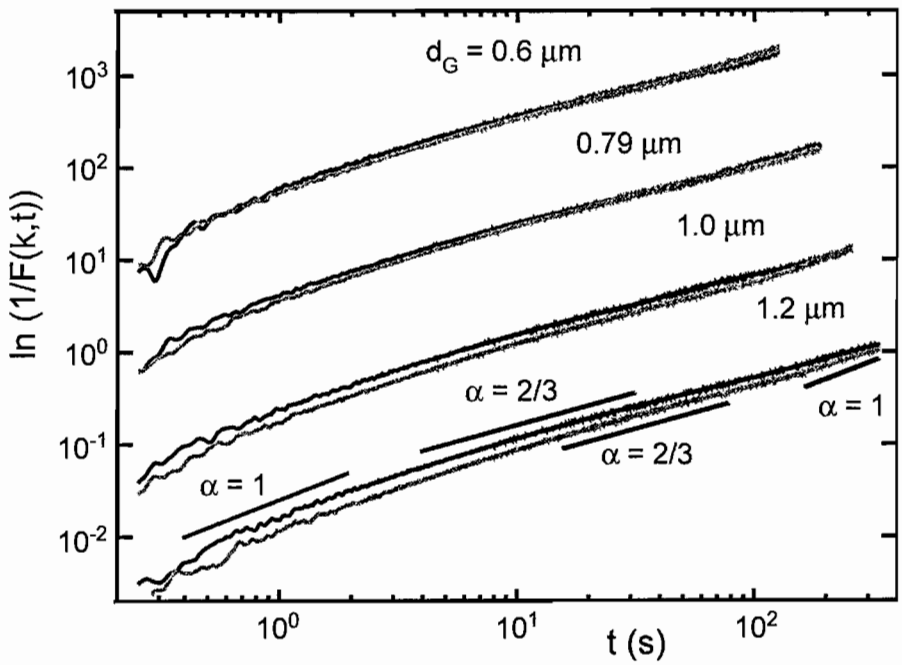

Figure 3.4. $\ln\left[1/F(k,\tau)\right]$ plots of mitochondrial fluctuations for the deletion mutant strain Arc18pΔ (gray curves) and its wild-type parent BY4741 (ARC18, black curves). Each set of curves corresponds to the length scale indicated. For the largest two length scales (1.03 μm and 1.19 μm)), the $\ln\left[1/F(k,\tau)\right]$ curves are lower for the mutant striain than the corresponding wild-type cell curves. There is also a small but discernible difference at shorter time scales for the $\ln\left[1/F(k,\tau)\right]$ curves at 0.79 μm where the Arc18pΔ mitochondria are less mobile than the wild-type mitochondria.

For the smallest length scale investigated (d_G = 0.6 μm), the mutant and wild-type parent strains behave nearly identically. However, for the largest three length scales (d_G =

0.79 μm, 1.03 μm and 1.19 μm), the mutant Arc18pΔ cells exhibit smaller magnitude displacements at short times, in comparison to the wild-type parent. This decrease in the dynamics is confirmed by the effective diffusion for short and long times observed for length scales greater than $d_G = 0.79$ μm, which are listed in Table 3.4. Similar to our findings for the act1-V159N cells, the shapes of the MSD curves are the same as those for the parent cells.

	Wild-type		Arc18pΔ	
Fringe Size (μm)	$\tilde{D}$ (cm^2 sec^{-1}) / 10^{-12} (time:0.7-1sec)	$\tilde{D}$ (cm^2 sec^{-1}) / 10^{-12} (time:70sec)	$\tilde{D}$ (cm^2 sec^{-1}) / 10^{-12} (time:0.7-1sec)	$\tilde{D}$ (cm^2 sec^{-1}) / 10^{-12} (time:70sec)
0.60	10.4	2.56	9.20	2.72
0.78	12.2	3.06	10.6	2.83
1.03	12.0	3.13	9.19	2.85
1.19	11.6	3.32	8.16	2.70

Table 3.4. Effective diffusion coefficients of mitochondria in wild-type parent Arc18p and Arc18pΔ cells.

Discussion

This work examines the influence of cytoskeletal function on mitochondrial dynamics in mating *S. cerevisiae*. Research on dividing yeast cells has shown that the inheritance of mitochondria in the daughter bud is unaffected by the loss of MTs, although mutations directed at the stability and function of the actin cytoskeleton limit the polarized movement of mitochondria from the mother to the daughter cell [20-24].

We find that mitochondria of mating yeast cells undergo anomalous sub-diffusive movements, similar to those of dividing yeast cells [18]. We have extended our study of mitochondrial dynamics to this stage of the cell cycle to expand on the underlying mechanism behind the motion of the organelle. Our method of recording and analyzing the dynamics of mitochondria using FICS is sensitive to very small displacements across many decades in time, and is therefore useful to address the question of which sub-cellular components play a role in the cytoskeleton-related movements of mitochondria [16].

By exposing *S. cerevisiae* of mating type 'a' to the 'α' factor pheromone of the opposite mating type, yeast cells were induced from the G1 stage of the cell cycle to the mating phase. We find that mitochondrial dynamics in Nocodazole treated cells are nearly identical to healthy cells (Figure 3.2). The MSD exhibits three regimes of temporal scaling behavior characterized by a sub-diffusive regime (α = 2/3), which bridges short and long time periods of diffusion (α = 1). Agpar et al. identified a similar three time-regime behavior for the MSD of microspheres suspended in f-actin networks [31, 32]. Treatment of yeast cells with Latrunculin-A, which destabilizes actin MFs by sequestering actin monomer, leads to suppression of mitochondrial motions for each of the four length scales we studied (d_G = 0.6 μm - 1.19 μm).

For an understanding of the time scaling shift from diffusive to sub-diffusive and then back to diffusive we offer two possible models. In the case of f-actin "caging", the mitochondria would exhibit diffusive behavior until it bumped into an actin filament confining the organelle to its cage (Figure 3.5, A). After a period of sub-diffusive

behavior due to the interactions between mitochondria and the f-actin cage, the mitochondria would return to a diffusive behavior on the time-scale that it takes for the f-actin cage to relax and rearrange. The studies on yeast mitochondrial segregation during mitosis also provide a suitable model to explain the shift in time scaling [23]. In the event that actin polymerization contributes a force to the directional displacement of mitochondria, then the arrest of such a polymerization force would occur on the time-scale where α transitions from diffusive to sub-diffusive and the time-scale for the initiation of a polymerization event leading to a displacement would correspond to the later transition from sub-diffusive to diffusive (Figure 3.5, C).

In theoretical explanations for mean square displacement behavior of caged particles in polymers, it was found necessary to account for a polymer depletion layer around the particles [33, 34] A decrease in the length of polymers decreases the size of the polymer depletion zone, effectively lowering the distance the particle may travel before encountering the wall in its polymer cage [35]. For Mitochondria this translates to less movement in an environment of shorter f-actin (Figure 3.5, B) and may be accounted for through an earlier transition to a sub-diffusive regime in Latrunculin-A treated cells. As an alternative to looking at the transition of the scaling parameter α, we turn to a short time (0.7-1 sec.) and long time (70 sec) effective diffusion coefficient calculated directly from the intermediate scattering function, $F\left(k,\tau\right)$. In accordance with a greater confinement due to a smaller depletion zone, the mitochondria in Latrunculin-A treated cells have a lower effective diffusion at short times (Table 3.2). At long times we

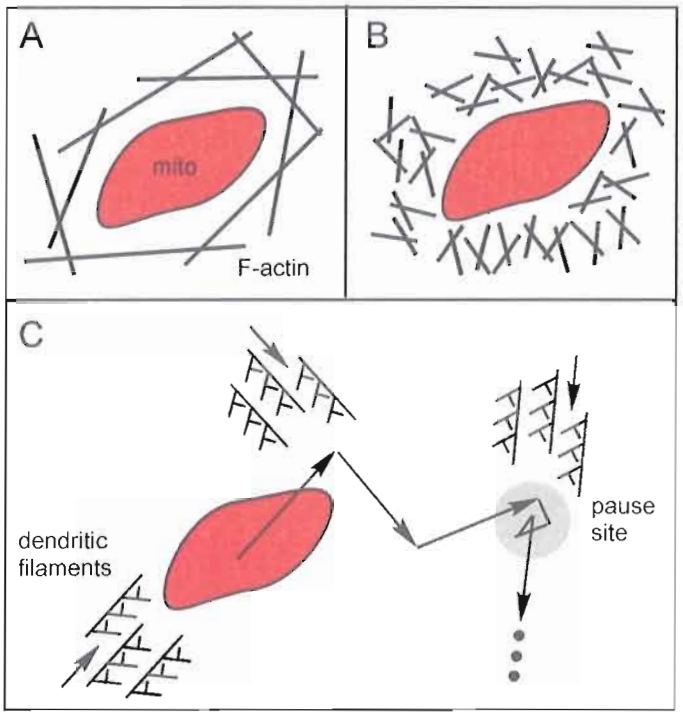

Figure 3.5. Putative models of actin-mitochondria interaction. The f-actin surrounding mitochondria cages the organelle but also contributes to a depletion zone, which is larger in cells with a normal cytoskeleton (A) than in cells that were treated with an actin destabilizing drug Latrunculin-A (B). At long times the mitochondria in panel (B), will experience a greater effective diffusion as compared to the one in (A) because the f-actin will relax on a shorter time-scale. Panel (C) portrays the arrest of polymerization events as the key contributor to the short-timescale dynamics of mitochondria, and the long pauses on intermediate time-scales are only then interrupted by the initiation of new polymerization events, which return the dynamics to diffusive at longer times.

anticipate the effective diffusion of Latrunculin-A treated mitochondria to increase relative to wild-type since the time it takes for the f-actin environment to relax should be shorter. However, this is not the case since the long time effective diffusion of mitochondria in Latrunculin-A treated cells is lower than the corresponding wild-type effective diffusion (Table 3.2). Turning to the actin polymerization force model, we predict that the addition of Latrunculin-A should increase the arrest of polymerization

forces and reduce the initiation of new polymerization events. The corresponding decrease of both long and short time effective diffusion coefficients corroborates this in Table 3.2. Our results are consistent with the observations of other workers who studied budding yeast cells, who connected the activity of the actin polymerization to mitochondrial motion directed along the mother-bud axis [20-23].

Actin polymerization is known to be an effective force generator in processes ranging from the extension of lamellipodia to the propulsion of bacteria in host cell cytoplasm [10, 29]. By comparing the dynamics of mitochondria in actin mutant cells to wild-type cells, we directly test this microscopic model against the f-actin cage model. We selected the actin mutant act1-V159N to perform our first assay, since it is known that this mutation has an increased *in vitro* rate of actin polymerization and f-actin persistence length in the presence of Arp2/3 [28, 36]. For the three largest of the four length-scales (d_G = 0.79 μm, 1.03 μm, 1.19 μm, Figure 3.3), the MSD plots of the mutant cells shift to positions that are higher than the corresponding wild-type curves. It should be noted that unlike the lateral shift of the temporal scaling value as observed in cells treated with MF destablizer Laturnculin-A, there is no corresponding shift in temporal scaling of act1-V159N mutants as compared to wild-type. The actin mutation is thus limited in its ability to dramatically change the dynamic-mechanical interaction between mitochondria and the cytoskeleton. An analysis of the effective diffusion at both short and long times allows us to proceed with a test of the two actin-mitochondria interaction models. For the mutant we expect the f-actin cage model to increase the effective diffusion at short times relative to the wild-type because an increased persistence length

should increase the volume of the depletion zone, and the long-time effective diffusion should decrease for the mutant since the f-actin would exist in a more stable state and rearrange on a slower time scale. When we turn to the actin polymerization force model, the anticipated short time effective diffusion would also increase on short times because the rate of arrest would not be as high in the mutant, but, on the contrary to the caging model, the initiation rate of actin polymerization forces in the mutant would increase the long-time effective diffusion of the mutant. In Table 3.3 we provide effective diffusions of mitochondria for the act1-V159N mutant and wild-type at long and short times. On the length scale with the most significant separation between wild-type and mutant MSD displacement data (Figure 3.3, $d_G = 0.79$ μm) our resultant effective diffusion values are consistent with those expected for the actin polymerization model. When we examine the temperature sensitive act1-V159N strain at room temperature (22°C), the mitochondrial dynamics are indistinguishable from those of the wild-type strain (data not shown). This control experiment confirms that our observations at elevated temperature are correlated to the act1-V159N mutation.

Our act1-V159N results prompted us to perform a second study to compare the dynamics in cells of an Arp2/3 mutant to those of its wild-type parent. As an Arp2/3 mutant, we chose a subunit knockout, Arc18pΔ, which is less detrimental to cell growth than other Arp2/3 mutants. The Arc18pΔ strain may also permit residual amounts of the Arp2/3 complex to form, and although there are actin polarization defects in the budding yeast cell, there is evidence of some actin patch formation [30]. The effect of this Arp2/3 mutation is to increase the relaxation time scales in comparison to wild-type, for the

length scales d_G = 0.79 μm, 1.03 μm and 1.19 μm (Figure 3.4). Bearing in mind that the Arc18pΔ strain maintains some features that depend on Arp2/3 functionality, we interpret this decrease in the rate of mitochondrial displacements in terms of a partial loss of Arp2/3 function. Returning once more to the actin-interaction models, we look at the long- and short-time effective diffusions of this mutant relative to its wild-type for some clarification as to which model is a better fit. In the f-actin cage model we expect to find a lower short-time effective diffusion for the mutant while the long-time effective diffusion should increase as compared to the wild-type. This is anticipated because the mutant would influence the length of f-actin structures, which decreases the depletion zone, and the decreased filament size should also shorten the time-scales of f-actin rearrangement. The impact of the Arc18pΔ mutant on effective diffusion as transmitted through the actin polymerization force model would decrease both long and short time effective diffusions since the rate of actin polymerization arrest would increase and the rate of new actin polymerization initiation would be lower when compared to wild-type. The findings in Table 3.4 agree more closely with the actin polymerization force model because both effective diffusions in the mutant show a decrease from the wild-type values.

The agreement between the predictions made about effective diffusion values for the actin polymerization force model and the short and long time effective diffusions derived from our data confirm that this model is a better description of the dynamic interaction between mitochondria and the actin cytoskeleton. In Table 3.5 we present an overview of how the f-actin cage model and actin polymerization model performed in our

comparison of expected and observed changes to the effective diffusion for all experiments.

	Depletion Zone Model		**Dendritic Assembly Model**	
Actin inhibitor	$\tilde{D}^S$ - interaction with f-actin cage	$\tilde{D}^L$ - relaxation of f-actin cage	$\tilde{D}^S$ - arrest of dendritic filament	$\tilde{D}^L$ - initiation of dendritic filament
Lat-A				
expected	Decrease	Increase	Decrease	Decrease
observed	Consistent	Inconsistent	Consistent	Consistent
act1-v159n				
expected	Increase	Decrease	Increase	Increase
observed	Consistent	Inconsistent	Consistent	Consistent
Arc18pΔ				
expected	Decrease	Increase	Decrease	Decrease
observed	Consistent	Inconsistent	Consistent	Consistent

Table 3.5. Overview of actin-mitochondria interaction model. Effective diffusions for short times, $\tilde{D}^S$, are defined between 0.7-1.0 seconds and effective diffusions for long times, $\tilde{D}^L$, are defined at 70 seconds.

Whereas the actin filament destabilizing drug Latrunculin-A can have a significant impact on actin dynamics and rearrangement of the cytoskeleton, we also looked to actin mutants for evidence of how actin dynamics affect movement of the mitochondria within the context of a more functional cytoskeleton. For both actin polymerization mutants, act1-V159N and Arc18pΔ, we observe an increasing departure

from normal mitochondrial dynamics as the experimentally probed length scale d_G is increased. For the act1-V159N strain, the rates of mitochondrial motion *increase* relative to wild-type for $d_G = 0.79$ μm, 1.03 μm and 1.19 μm (Figure 3.3), while for the Arc18pΔ strain, the rates *decrease* relative to wild-type on shorter time scales for $d_G = 0.79$ μm 1.03 μm and 1.19 μm (Figure 3.4). These results suggest that the mitochondrial transport mechanism depends on the coordinated process of actin polymerization, and involves macroscopic actin filament growth. The similarity between mutant and wild-type cell dynamics at the shortest length-scales investigated indicates a crossing over from an f-actin network nucleation to growth phase, with a critical nucleation size approximately equal to the cross-over length scale ($d_G \sim 0.79$ μm). This interpretation is consistent with previous studies of osteosarcoma cells, where local segments of mitochondria were observed to undergo "hopping" motions at this same length scale during sub-second time intervals [15]. In the context of a nucleation and growth picture, we can view the behavior of the mutant strains in terms of the collective stability of the actin filament network. For example, in the Arc18pΔ cells a small pool of functional Arp2/3 might carry out the initial steps of the actin polymerization. However, after the formation of a critical nucleus of filaments, the mutant cells may no longer support network growth over larger distances at the wild-type levels. Similarly, it is possible that the defective functionality in both mutants become operative only after sufficient actin filament growth has occurred. In each scenario, the difference in the dynamics becomes apparent as larger length-scales are traversed.

Concluding Remarks. The methodology presented in the current work allows for a quantitative analysis of the dynamics of mitochondria in mating yeast. All of the TCFs obtained from our studies are multi-exponential. Since the mean-square displacement is proportional to $\ln\left[1/F(k,\tau)\right]$, where $F(k,\tau)$ is the TCF, we have quantified the dynamic behavior of mitochondria in terms of this function. In contrast to the large differences observed between the mitochondrial dynamics of healthy cells and cells treated with Latrunculin-A, there are much smaller differences between actin mutant cells and their wild-type parents. The actin polymerization defects introduced in the mutant strains do not completely abolish actin cytoskeletal activity. While our results indicate that f-actin "caging" effects have a smaller impact on the mitochondrial transport mechanism as compared to actin polymerization, they do not eliminate the possibility that other modes of force generation are also involved. A more complete picture will follow from further studies that investigate the roles of linear actin cable flow, an Arp2/3 independent process, and mitochondrial associations with actin cables.

The current analysis of local mitochondrial fluctuations underscores the notion that a dynamically heterogeneous process governs the motions of this organelle. Such behavior cannot be fully understood from structural information alone. By generating two-point TCFs from FICS measurements collected on Latrunculin-A treated cells and actin polymerization mutants and presenting this data in terms proportional to the MSD, it is possible to distinguish between subtle changes in the sub-diffusive processes that drive mitochondrial movements. More detailed dynamic information may follow from analyses of FICS measurements that account for higher-order correlated motions. For

example, a four-point correlation analysis should reveal the time- and length-scales over which successive mitochondrial movements are coupled. Such approaches may prove useful to the general problem of detecting the effects of agents that disrupt normal cytoskeletal function.

Methods

Yeast Strains and Fluorescent Labeling of Mitochondria. In Table 3.1, we list the strains of *S. cerevisiae* that we used in this study. We selected MATa strains for their sensitivity to alpha factor, which shifts these cells into the mating phase of the cell cycle. To visualize mitochondria, we transformed the cells with pRS316, containing DsRed.T1 fused to the COX4 leader sequence. We cultured cells to log phase in SD media, before treating them with 100 μM alpha factor for two hours. For our microtubule depletion experiments, we treated samples with Nocodazole at 30 μg/mL, followed by incubation for an additional 30-40 minutes. For our microfilament depletion measurements, we treated samples with Latrunculin-A at 200 μM for a 10-minute incubation period. In preparing our samples, we mounted them onto a thin 3% agarose pad using SD media and 10 μM alpha factor. We sealed the samples using valap to fuse the edges of a coverslip to the glass slide. To visualize MTs or actin microfilments, we performed antibody staining with rat anti-α-tubulin (YOL 1/2 from clontech) or Alexa-phalloidin-542, following a 3.7% paraformaldehyde fixative treatment [37]. We conducted our studies of the effects of cytoskeletal inhibiting drugs on mitochondrial motility at 22°C; the mutant act1-

V159N (DDY 1493) and its parent (DDY1495) at 36°C; and the mutant Arc18pΔ and its wild-type parent BY4741 at 22°C.

Quantitative Characterization of Yeast Mitochondrial Dynamics by Fourier Imaging Correlation Spectroscopy (FICS). To quantify the cytoskeletal-specific motions of yeast mitochondria, we conducted FICS experiments under conditions in which key cytoskeletal components were either removed using pharmaceutical agents, or were inhibited in mutant strains. Our measurements span a wide range of distances (0.6 – 1.2 μm) and times ($10^{-1} - 3 \times 10^{2}$ s) to characterize these motions. FICS is a phase-selective approach to measure mitochondrial filament fluctuations [16, 25]. The sample is placed at the focal plane of a fluorescence microscope where an excitation grating is generated by intersecting two vertically polarized laser beams. A modulated fluorescence signal is detected from the spatial overlap of the grating and a fluctuating density of labeled mitochondrial filaments. The laser beam waist at the sample (40 μm) is wide enough to encompass ~ 15 – 30 yeast cells, while the fringe spacing d_G is adjustable between 0.5 – 1.2 μm. The wave vector $\mathbf{k} = \left(2\pi/d_{\mathrm{G}}\right)\hat{\mathbf{i}}$ specifies the spatial frequency and orientation of the grating, where $\hat{\mathbf{i}}$ is a unit vector pointing in the direction of the *x*-axis. The local filament density is described by $\delta n(\mathbf{r},t) = \sum_{i=1}^{N} A_i \delta\left[\mathbf{r} - \mathbf{r}_i(t)\right] - N\bar{A}/V$, where $\mathbf{r}_i$ is the center-of-mass position of the *i*th segment, A_i is its fluorescence intensity, V is the sample volume, and $\bar{A}$ is the mean segment intensity. The phase of the grating ϕ is

modulated at the frequency 50 000 Hz, so that the fringes are swept at a much greater speed than an average filament can move.

By phase-synchronous detection of the modulated fluorescence, we determine the complex signal $\hat{N}_{\mathbf{k}}(t) = N^{-1/2}\sum_{i=1}^{N} A_i \exp i\left[\mathbf{k}\cdot\mathbf{r}_i(t)\right]$ [25, 26]. This signal is the Fourier transform of the sampled mitochondrial density distribution, defined at the wave-vector of the excitation grating. As the mitochondrial filament positions fluctuate, the resultant signal monitored by our experiment evolves in time.

In a typical experiment, we collect ~ 524 000 data points at an acquisition frequency of 256 Hz, over a period of ~ 35 minutes. To quantify the time-dependence of $\hat{N}_{\mathbf{k}}(t)$, we calculate the two-point time correlation function (TCF) $\left\langle \hat{N}^*_{\mathbf{k}}(0)\hat{N}_{\mathbf{k}}(\tau)\right\rangle = \lim_{T\to\infty}\frac{1}{T}\int_0^T \hat{N}^*_{\mathbf{k}}(t')\hat{N}_{\mathbf{k}}(\tau+t')dt'$, where the angle brackets indicate the integration over time, and τ is the interval separating successive measurements. These measurements were repeated between 10 – 15 times, compared for consistency, and averaged together. The TCF decays on a time scale associated with the movement of filaments across distances characteristic of the optical fringe spacing d_G. For a dilute system of non-interacting Brownian particles, the TCF is expected to decay as a single exponential $\exp(-\tau/\tau_0)$, with $\tau_0 = \left(k^2 D_0\right)^{-1}$ the average time required for a particle to diffuse the distance d_G with diffusion constant D_0 [16]. We expect deviations from diffusive behavior to reflect the non-random interactions of mitochondrial segments with cytoskeletal elements, in addition to the influence of other intracellular species. To account for these deviations, we adopt the general form for the TCF:

$\exp\left\{-\frac{1}{6}k^{\gamma}\left\langle\Delta r^2(\tau)\right\rangle\right\}$, where the mean-square-displacement $\left\langle\Delta r^2(\tau)\right\rangle = 6D\tau^{\alpha}$, D is a generalized diffusion coefficient, and γ and α are spatial and temporal scaling exponents, respectively. The parameter $L = \gamma/\alpha$ specifies the nature of the dynamics. For L = 2, the dynamics are termed diffusive, while sub-diffusive and super-diffusive dynamics are characterized by L > 2 and L < 2, respectively.

CHAPTER IV

KINETIC PATHWAYS OF SWITCHING OPTICAL CONFORMATIONS IN DSRED BY 2D FOURIER IMAGING CORRELATION SPECTROSCOPY

The two people who collected the bulk of the PM-FICS experimental data on DsRed are M. Fink and K. Adair. This chapter was possible through their diligence and the collaborative effort with G. Lott on interpreting these data.

Having already established in chapter II that polarization-modulated FICS (PM-FICS) is a method able to separate a signal due to internal conformational changes from the part that stems from translational dynamics, this chapter builds on the experimental data recovered from DsRed dynamics by generating a new form of 2D optical spectroscopy. This tetrameric protein has the overall effect of depolarizing light as energy transfer processes occur between the four chromophores residing in DsRed, and as the four chromophores switch between different spectral states, there are consequent changes

to the degree of depolarization. This chapter explores the topography of 2D spectra defined by the fluctuations in DsRed depolarization.

Background

A remarkable feature of proteins and nucleic acids is their unique ability to undergo cooperative rearrangements in structure as part of mechanisms to regulate biological activity. Rather than exist as a single, stable conformation, biological macromolecules often exhibit a broad, heterogeneous distribution of sub-states in thermal equilibrium [1, 2]. Activation and inter-conversion between sub-states can span many decades over time [3]. Such systems exhibit complex spectra of relaxations, with principle time scales determined by transformations between sub-states, and exchange kinetics between different transition pathways [4].

The kinetics of conformational transitions and chemical exchange can be studied by two-dimensional (2D) NMR spectroscopy [4]. Transitions between conformations of biological macromolecules are reflected by the magnitudes of diagonal and off-diagonal peaks in 2D NMR spectra. In recent years, chemical exchange spectroscopy has been applied at infrared and visible frequencies [5]. 2D optical methods can investigate the inter-conversion between populations of chemical species that are spectroscopically non-equivalent. Such 2D optical experiments measure equilibrium chemical kinetics on the time scales of the excited state lifetimes of vibrational or electronic transitions.

In the current work, we show how polarization modulated Fourier imaging correlation spectroscopy (PM-FICS) can probe the pathways of optical switching conformations of the fluorescent protein complex, DsRed, over a broad range of time scales much longer than the excited state lifetime (10^{-3} – 10^{2} s). The PM-FICS method, and its application to DsRed, is described previously in chapter II. Similar to 2D optical and NMR methods, PM-FICS provides a phase-dependent optical signal that determines four-point time-correlation functions and the associated 2D spectra. Moreover, the information obtained from DsRed is sufficient to construct joint probability distributions of time-dependent conformational coordinates.

From a kinetic perspective, the DsRed protein is a dynamically complex heterogeneous system. Unlike monomeric variants of the green fluorescent protein (GFP) [6], DsRed is an obligate tetramer of FP subunits [7]. FPs are single chains of ~ 230 amino acid residues, which form an 11-stranded β-barrel with dimensions ~ 3 nm × 4 nm. An α-helix inside the barrel contains the sequence of three residues that form the p-hydroxy-benzylidene-imidazolidinone chromophore. In DsRed, the π-π^* electron system of the chromophore is chemically and irreversibly extended to include an acylimine substituent, adjacent to the imidazolidinone [8, 9]. This so-called maturation process occurs over the course of several days and can be followed by a gradual gain in red photo-luminescence accompanied by a loss of green emission [8, 10]. Nevertheless, the maturation reaction does not run to completion, even after prolonged aging, so that a given DsRed molecule likely contains at least one 'immature' green chromophore [8, 11-

13]. The red chromophore itself undergoes switching transitions, or 'flickering', between optical conformations of different emission wavelengths and intensities, and on time scales ranging between milliseconds and tens-of-seconds [14-17].

Although many studies have focused on the reversible, light induced pathways between 'bright' and 'dark' conformations [11, 14-17], thermally driven transitions between ground states are also possible [13, 16]. Detailed spectroscopic studies reveal that the red chromophore can reversibly interconvert, either through excited-state or ground-state pathways, between two brightly fluorescent red conformations (called 'red' and 'far-red'), and a relatively dim 'green' conformation [12, 13]. The energetic barriers mediating these transitions are on the order of $\sim 1000\ cm^{-1}$ (or $12\ kJ\ mol^{-1} \simeq 5 \times k_B T$ at ambient temperatures). Although the physical nature of the inter-conversion processes remains unclear, possible mechanisms include isomerization of the protein-chromophore hydrogen-bonded network, cis-trans photo-isomerization, and ground state bond rotation [16, 18].

For our current purposes, we invoke a simplified model to interpret the conformational dynamics that influence excited state energy transfer between adjacent chromophores in the DsRed complex. Figure 4.1 depicts the DsRed molecule as four cylinders (arbitrarily labeled 1 – 4) with principle axes oriented approximately as in the crystal structure [7]. Crystallographic data suggest that there are three possible relationships between any pair of adjacent chromophores, given by the relative transition dipole orientations ($\theta^{24} = 41°$, $\theta^{23} = 47°$, and $\theta^{34} = 21°$) and the inter-dipole distances

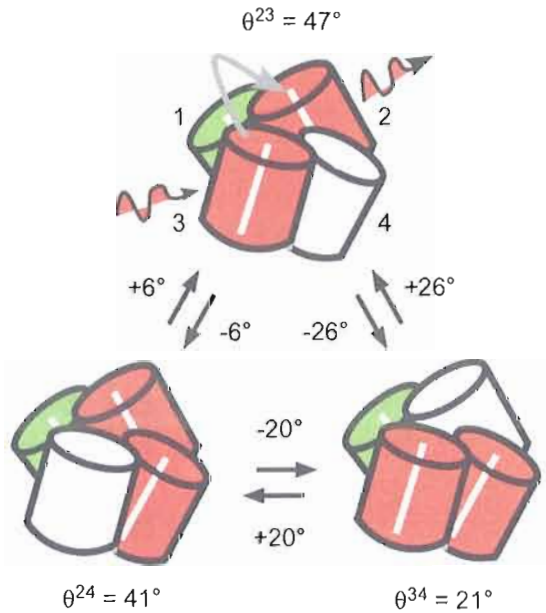

Figure 4.1. Optical conformational transitions of the 'mature' red chromophores in DsRed. DsRed is a tetrameric complex of cylindrically shaped fluorescent protein subunits, with relative orientations approximated in the figure. Each subunit has at its center an optical chromophore that can occupy one of two chemical states, corresponding to green or red emission. The green chromophores (shaded green) do not undergo chemical conversion to the red state on the time scales of our measurements. Red chromophores can inter-convert on millisecond time scales between two highly luminescent "bright" states (shaded red), and one "dark" state (shaded gray). From the crystallographic structure of DsRed, the relative angles θ^{ae} between adjacent absorption and emission transition dipole moments are known, and identified according to the numbering system shown on the top species. Polarization- and spectrally-selective excitation of the red chromophore subunits, mediated by electronic excitation transfer between coupled chromophores occupying adjacent sites, results in discrete transitions in the fluorescence depolarization angle $\Delta\theta^{ae}$.

(r^{24} = 43Å, r^{23} = 38Å, and r^{34} = 22Å). By symmetry, the relationships between paired transition dipoles 2-4, 2-3, and 3-4 are the same as those between 1-3, 1-4, and 1-2, respectively [7].

As previously mentioned, most DsRed tetramers contain at least one immature green chromophore, which does not mature to red over the course of a PM-FICS measurement (~ 10 minutes). Of the sites that have matured to red (with absorption maximum $\lambda_{max} \sim 563$ nm), these undergo reversible inter-conversion to the far-red conformation ($\lambda_{max} \sim 577$ nm), or to the weakly fluorescent green conformation ($\lambda_{max} \sim 484$ nm), on time scales of tens-of-milliseconds and longer. Figure 4.1 depicts a DsRed molecule with a single static (immature) green site at position 1 (shaded green), and three dynamically inter-converting red sites at positions 2 – 4. In the experiments presented below, the red optical transitions ($\lambda_{ex} \sim 532$ nm) are selectively excited, and the integrated emission from both red and far-red states is detected. Both red and far-red conformations are considered bright states (shaded red in Figure 4.1), while green states of the mature chromophore are dark (shaded gray). Thus, the immature green site at position 1 is pinned, while the red sites at positions 2 – 4 undergo reversible switching between bright and dark states. Because the distances and orientations between resonant optical transition dipoles are relatively small, an excited red chromophore can transfer its energy to one of its unexcited red or far-red neighbors by an energy transfer mechanism. When two sites in the DsRed complex are thus optically coupled, the emission polarization rotates by the angle θ^{ae}, which subtends the absorption dipole moment of the initially excited chromophore and the emission dipole moment of the emitting chromophore [14, 17]. Figure 4.1 illustrates three possible pair-wise couplings between bright chromophore sites (for molecules with one site pinned), and the associated

depolarization angles. Also indicated are the six possible angular displacements $\Delta\theta^{ae}$ associated with conformational transitions between the three optically coupled states. Similar pair-wise couplings and transitions are possible for a molecule with all of its sites red (zero sites pinned). However, for a molecule with two or more sites pinned, transitions between distinct pair-wise coupled conformations are not possible, and such species are not expected to contribute to the fluctuating emission signals.

The model depicted in Figure 4.1 is consistent with available experimental data for DsRed. However, little is known about the details of such thermally activated switching transitions, such as whether they occur at random or in a cooperative manner due to interactions between adjacent FP subunits. For example, a cooperative mechanism could involve a series of optical conformations, dynamically connected along multiple kinetic pathways. The following work demonstrates how 2D PM-FICS can determine such information about the optical transitions of multi-colored FPs by monitoring the coordinate fluctuations of a finite population of molecules.

Experimental Methods

PM-FICS Observables. The equilibrium coordinate fluctuations of a finite population of DsRed molecules in 95% glycerol / water solution were monitored by the PM-FICS method, as described in chapter II. The measurement observables are the number density $Z_{k_G}^{ND}(t) \propto \left\langle \exp i\left[k_G x(t)\right]\right\rangle$, and the anisotropy density $Z_{k_G}^{AD}(t)$

$\propto \left\langle \exp i\left[k_G x(t) - 2\theta^{ae}(t)\right]\right\rangle$, where the angle brackets indicate a sum over the $\sim 10^6$ molecules in the illuminated sample volume. In these expressions, $x(t)$ and $\theta^{ae}(t)$ are time-dependent position and conformation coordinates, respectively. We interpret these signals using the first order cumulant approximation (discussed in chapter II).

Four-Point Time Correlation Functions. Four-point time correlation functions (TCF) for the number density and anisotropy density fluctuations were constructed from products of four sequential data points:

$$C_{ND}^{(4)}(t_{43},t_{32},t_{21}) \equiv \left\langle Z_{k_G}^{ND*}(0) Z_{k_G}^{ND}(t_{21}) Z_{k_G}^{ND}(t_{32}+t_{21}) Z_{k_G}^{ND*}(t_{43}+t_{32}+t_{21})\right\rangle \tag{4.1}$$

and

$$C_{AD}^{(4)}(t_{43},t_{32},t_{21}) \equiv \left\langle Z_{k_G}^{AD*}(0) Z_{k_G}^{AD}(t_{21}) Z_{k_G}^{AD}(t_{32}+t_{21}) Z_{k_G}^{AD*}(t_{43}+t_{32}+t_{21})\right\rangle . \tag{4.2}$$

Equations 4.1 and 4.2 define the time intervals $t_{43}(=t_4 - t_3)$, t_{32}, and t_{21} with $t_4 \geq t_3 \geq t_2 \geq t_1 \geq 0$. In the first-order cumulant approximation, Equations 4.1 and 4.2 can be written

$$C_{ND}^{(4)}(t_{43},t_{32},t_{21}) = \left\langle \exp\left[-\tfrac{1}{2} k_G^2 \delta\Delta\bar{x}_N^2(t_{21})\right]\right\rangle \left\langle \exp\left[-\tfrac{1}{2} k_G^2 \delta\Delta\bar{x}_N^2(t_{43})\right]\right\rangle \tag{4.3}$$

$$\times\left\langle \exp ik_{\mathrm{G}}\left[\Delta\bar{x}_N(t_{43})-\Delta\bar{x}_N(t_{21})\right]\right\rangle$$

and

$$C_{AD}^{(4)}(t_{43},t_{32},t_{21})=C_{ND}^{(4)}(t_{43},t_{32},t_{21})C_{A}^{(4)}(t_{43},t_{32},t_{21}), \tag{4.4}$$

where

$$C_{A}^{(4)}(t_{43},t_{32},t_{21})=\left\langle \exp\left[-2\delta\Delta\bar{\theta}_N^{ae2}(t_{21})\right]\right\rangle\left\langle \exp\left[-2\delta\Delta\bar{\theta}_N^{ae2}(t_{43})\right]\right\rangle$$

$$\times\left\langle \exp i2\left[\Delta\bar{\theta}_N^{ae}(t_{43})-\Delta\bar{\theta}_N^{ae}(t_{21})\right]\right\rangle. \tag{4.5}$$

Equation 4.3 defines the time-ordered displacements of the mean center-of-mass, $\Delta\bar{x}_N(t_{21})\left[=\bar{x}_N(t_2)-\bar{x}_N(t_1)\right]$ and $\Delta\bar{x}_N(t_{43})$, which occur during successive time intervals t_{21} and t_{43}, respectively. Similarly, Eq. (4.5) defines the time-ordered displacements of the mean depolarization angle, $\Delta\bar{\theta}_N^{ae}(t_{21})$ and $\Delta\bar{\theta}_N^{ae}(t_{43})$. Equation 4.4 suggests that the anisotropy TCF can be determined from the ratio $C_{A}^{(4)}(t_{43},t_{32},t_{21})=C_{AD}^{(4)}(t_{43},t_{32},t_{21})/C_{ND}^{(4)}(t_{43},t_{32},t_{21})$. These four-point TCFs have similar mathematical forms to those employed in two-dimensional optical and magnetic resonance spectroscopy [19]. Four-point TCFs contain information about correlations of events that occur during the intervals t_{43} and t_{21}, and decay on time scales for which the magnitudes of the collective phase displacements deviate by an amount $\sim \pi/4$. Such correlations diminish with increasing waiting period t_{32}, so that they appear indistinguishable from the products of functionally independent two-point TCFs. It is

therefore useful to focus on the t_{32} -dependence of the difference correlation functions, $C^{(4)}(t_{43},t_{32},t_{21}) - C^{(2)}(t_{43})C^{(2)}(t_{21})$.

Two-Dimensional Spectral Densities. It is convenient to represent the four-point TCFs in the frequency domain, through their partial Fourier transform, with respect to t_{43} and t_{21}

$$S^{(4)}(\nu_{43},t_{32},\nu_{21}) = \int_0^\infty dt_{43} \int_0^\infty dt_{21} \left[C^{(4)}(t_{43},t_{32},t_{21}) - C^{(2)}(t_{43})C^{(2)}(t_{21})\right] e^{i\nu_{21}t_{21} + i\nu_{43}t_{43}} . \tag{4.6}$$

The 2D spectral density is given by the absolute value $\left|S^{(4)}(\nu_{43},t_{32},\nu_{21})\right|$, plotted in the $\nu_{21} - \nu_{43}$ plane. The 2D spectral density is related to the joint probability that the system undergoes two successive coordinate displacements at the transition rates ν_{21} and ν_{43}, separated in time by the interval t_{32}. Such 2D spectra are similar to those obtained by magnetic resonance and optical techniques, and can provide information about the rates of chemical processes.

Two-Dimensional Distribution Functions. Information about weights and magnitudes of correlated displacements can be obtained from four-point distribution functions (DFs). We define $P^{(4)}\left[\Delta\bar{x}_N(t_{43});\Delta\bar{x}_N(t_{21})\right]$ as the joint probability density of sequentially sampling N molecules whose mean center-of-mass undergo two successive

displacements, $\Delta\bar{x}_N(t_{21})$ and $\Delta\bar{x}_N(t_{43})$, during the intervals t_{21} and t_{43}, respectively. We construct the joint distributions by sampling four-point products of the form

$$Z_{k_G}^{ND*}(0)Z_{k_G}^{ND}(t_{21})\,Z_{k_G}^{ND}(t_{32}+t_{21})Z_{k_G}^{ND*}(t_{43}+t_{32}+t_{21})$$

$$=\exp\left[-\tfrac{1}{2}k_G^2\delta\Delta\bar{x}_N^2(t_{21})\right]\exp\left[-\tfrac{1}{2}k_G^2\delta\Delta\bar{x}_N^2(t_{43})\right]\times\exp ik_G\left[\Delta\bar{x}_N(t_{43})-\Delta\bar{x}_N(t_{21})\right].$$

Such products are used to calculate 2D histograms of the joint probability to observe mean center-of-mass displacements during consecutive time intervals. As discussed in chapter II, if the center-of-mass displacements are uncorrelated, then joint distributions can be factored into a product of two-point DFs, i.e. $P^{(2)}\left[\Delta\bar{x}_N(t_{43})\right]P^{(2)}\left[\Delta\bar{x}_N(t_{21})\right]$. For such Brownian systems of diffusing molecules, the joint distribution is expected to be a two-dimensional Gaussian centered about the coordinate $\Delta\bar{x}_N(t_{43})=\Delta\bar{x}_N(t_{21})=0$.

2D distributions are similarly defined for displacements of the mean depolarization angle. $P^{(4)}\left[\Delta\bar{\theta}_N^{ae}(t_{43});\Delta\bar{\theta}_N^{ae}(t_{21})\right]$ is the joint distribution associated with consecutive displacements of conformation, which is constructed from four-point products of the anisotropy density $Z_{k_G}^{AD*}(0)Z_{k_G}^{AD}(t_{21})\,Z_{k_G}^{AD}(t_{32}+t_{21})Z_{k_G}^{AD*}(t_{43}+t_{32}+t_{21})=$

$Z_{k_G}^{ND*}(0)Z_{k_G}^{ND}(t_{21})\,Z_{k_G}^{ND}(t_{32}+t_{21})\,Z_{k_G}^{ND*}(t_{43}+t_{32}+t_{21})$

$Z^{A*}(0)Z^{A}(t_{21})\,Z^{A}(t_{32}+t_{21})\,Z^{A*}(t_{43}+t_{32}+t_{21})$. It is possible to divide the above expression by the contributions from the number density to isolate the anisotropy effects alone, i.e. $Z^{A*}(0)Z^{A}(t_{21})\,Z^{A}(t_{32}+t_{21})Z^{A*}(t_{43}+t_{32}+t_{21})$

$$=\exp\left[-2\delta\Delta\bar{\theta}_N^{ae2}(t_{21})\right]\exp\left[-2\delta\Delta\bar{\theta}_N^{ae2}(t_{43})\right]\times\exp i2\left[\Delta\bar{\theta}_N^{ae}(t_{43})-\Delta\bar{\theta}_N^{ae}(t_{21})\right].$$

As we discuss below, such four-point DFs contain detailed information about correlated changes in the conformation of coupled dipoles of the DsRed complex.

Results and Discussion

In Figure 4.2, we present results for the 2D spectral density and the joint DF of the mean center-of-mass displacements. In Figure 4.2A is shown the logarithm of $\left|S_{ND}^{(4)}(\nu_{21},t_{32},\nu_{43})\right|$ in the $\nu_{21}-\nu_{43}$ plane, for t_{32} = 10 ms. Because the TCFs for DsRed translational motion decay exponentially, the Fourier transform-related spectral density [see Eq. (6)] is Lorentzian. For $t_{32} \leq$ 20 ms, a minor feature is observed along the diagonal line $\nu_{21} = \nu_{43}$, indicating correlated motion on these relatively short time scales. For $t_{32} >$ 20 ms, the feature along the diagonal disappears (data not shown). In Figure 4.2B is shown the joint distribution $P_N^{(4)}\left[\Delta\bar{x}_N(t_{21});\Delta\bar{x}_N(t_{43})\right]$ evaluated at $t_{21} = t_{32} = t_{43} =$ 10 ms. For all values of t_{32} investigated, the joint DF appears as a two-dimensional Gaussian consistent with Brownian motion. These results support the view that cooperative center-of-mass displacements do not play a significant role in DsRed dynamics on the time scales of the current measurements.

Having established an accurate picture of the center-of-mass dynamics for DsRed, it is possible to apply the aforementioned factorization procedure to determine the 2D spectrum of anisotropy fluctuations. In Figure 4.3 is shown the logarithm of the two-

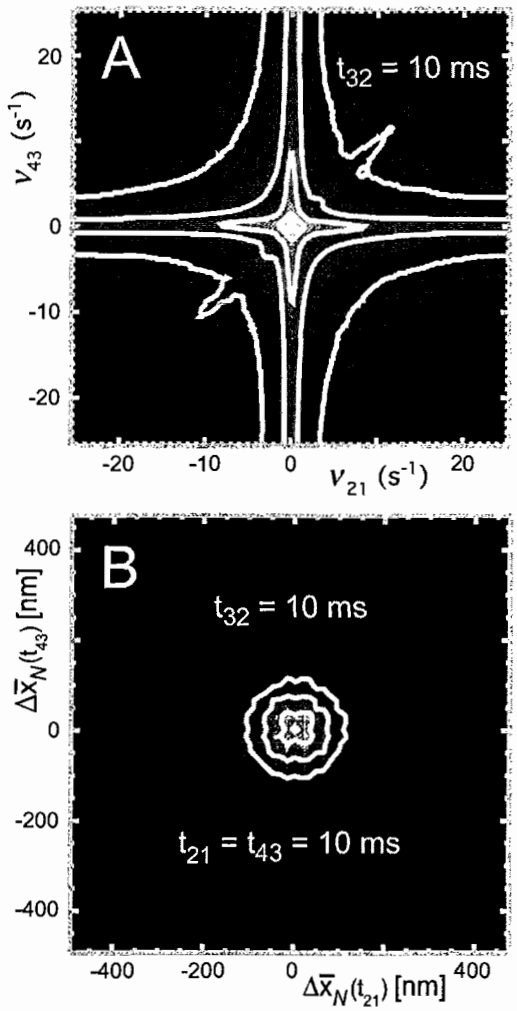

Figure 4.2. Contour diagrams of the two-dimensional spectral density and joint distribution function of center-of-mass displacements. In panel (A) is shown the logarithm of $\left|S_{ND}^{(4)}(\nu_{21},t_{32},\nu_{43})\right|$ versus ν_{21} and ν_{43} for a single value of the waiting period t_{32} = 10 ms. The lineshape is nearly Lorentzian, centered at the peak value $\nu_{21}=\nu_{43}=0$. In panel (B) is shown the joint distribution $P_N^{(4)}\left[\Delta\bar{x}_N(t_{21}),t_{32},\Delta\bar{x}_N(t_{43})\right]$ for the values $t_{21}=t_{32}=t_{43}$ = 10 ms. The 2D distribution is approximately Gaussian, and centered about the origin with $\Delta\bar{x}_N(t_{21})=\Delta\bar{x}_N(t_{43})=0$.

dimensional spectral density $\left|S_A^{(4)}(\nu_{21},t_{32},\nu_{43})\right|$ as a contour diagram in the $\nu_{21}-\nu_{43}$ plane, with t_{32} = 20 ms. Features that appear on the line diagonal to the spectrum ($\nu_{21}=\nu_{43}$) indicate sampled populations that maintain their rate of conformational transitions over the duration of the waiting period. Features that lie off the diagonal line, i.e. $\nu_{21}\neq\nu_{43}$, represent populations that undergo transitions between distinct regions of the spectrum during the waiting period. In Figure 4.3, the magnitude of the spectrum evaluated at the diagonal line is projected onto the horizontal and vertical axes. The sampled populations

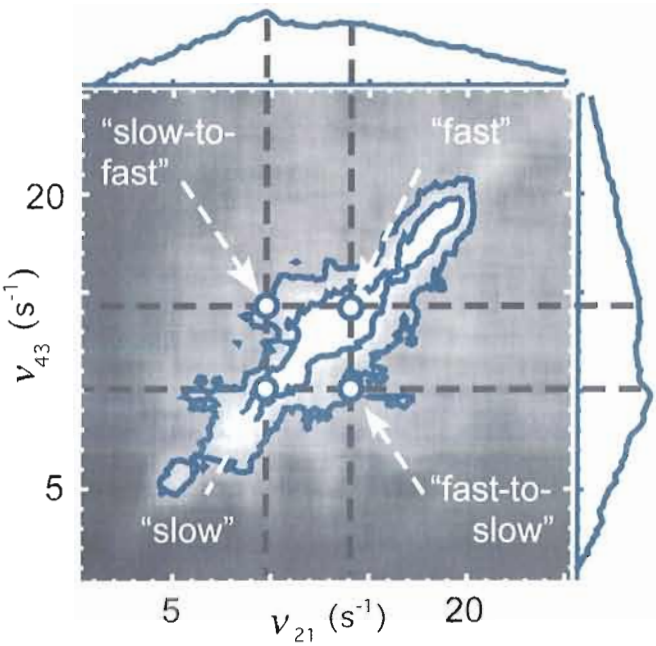

Figure 4.3. Logarithm of the two-dimensional spectral density of the mean depolarization angles $\left|S_A^{(4)}(\nu_{21}, t_{32}, \nu_{43})\right|$, for waiting period t_{32} = 20 ms. Features along the diagonal line (labeled "fast" and "slow") indicate the distribution of conformational transition rates, while off-diagonal features indicate molecular populations that "exchange" between conformational transition rates. Along the horizontal and vertical axes is projected the magnitude of the spectrum, evaluated at the diagonal $\nu_{21} = \nu_{43}$. Contours are shown at 0.5 and 0.25 times the peak height.

are broadly distributed among transition rates ranging from 0 – 25 Hz, and are roughly partitioned into two peaks centered at ~ 10 and 14 Hz. In Figure 4.3, these peaks are labeled "slow" and "fast" and are indicated by vertical and horizontal dashed lines. At the intersections of the dashed lines are diagonal features associated with "slow" and "fast" populations. Off-diagonal features are labeled "slow-to-fast" and "fast-to-slow," to indicate molecular sub-populations that make transitions between the two spectral regions. Because the 2D spectrum is narrow in the direction of the anti-diagonal ($\nu_{21} = -\nu_{43}$), the sampled populations do not readily exchange between fast and slow spectral regions on the time scale of ~ 20 ms.

We next determine joint DFs that contribute to the spectral line shape. In Figures 4.4A – 4.4D are shown contour diagrams of $P^{(4)}\left[\Delta\bar{\theta}_N^{ae}(t_{43});\Delta\bar{\theta}_N^{ae}(t_{21})\right]$ corresponding to each of the four labeled points in the 2D spectrum shown in Figure 4.3. Features in the joint DF can establish the existence of "pathways" between adjacent conformational transitions. For each of the DFs shown in Figure 4.4, the values of the intervals are t_{32} = 20 ms, and t_{21} , t_{43} $\in\{70\text{ ms}, 100\text{ ms}\}$, which were chosen to correspond to the labeled points in the spectral density (Figure 4.3). Along the horizontal and vertical axes are shown the projected magnitudes, which span the range $\pm$ 30° . These DFs were constructed from histograms of ~ 35,000 four-point products. The procedure was repeated to insure reproducibility of independent data sets, and the results were averaged together to produce the DFs shown in Figure 4.4.

For the two DFs representing diagonal features of the spectral density (labeled "fast" and "slow"), both exhibit mirror plane symmetry with respect to the diagonal line [$\Delta\bar{\theta}_N^{ae}(t_{21}) \simeq \Delta\bar{\theta}_N^{ae}(t_{43})$]. For the two DFs representing off-diagonal features (labeled "slow-to-fast" and "fast-to-slow"), each exhibits the projections of the "fast" and "slow" DFs onto one another. The joint DFs exhibit numerous peaks and shoulders, which undoubtedly reflect the conformational transitions of a complex heterogeneous system. In our current analysis, we focus on a subset of these peaks (indicated by vertical and horizontal dashed lines in Figure 4.4). For the DF representing "slow" displacements (Figure 4.4C), there are peaks centered at the coordinates $\left[\Delta\bar{\theta}_N^{ae}(t_{21}), \Delta\bar{\theta}_N^{ae}(t_{43})\right]$ =

$(-6^\circ, -6^\circ)$, $(+2^\circ, -6^\circ)$ and $(-6^\circ, +2^\circ)$. For the distribution representing "fast" displacements (Figure 4.4B), there are peaks at the coordinates

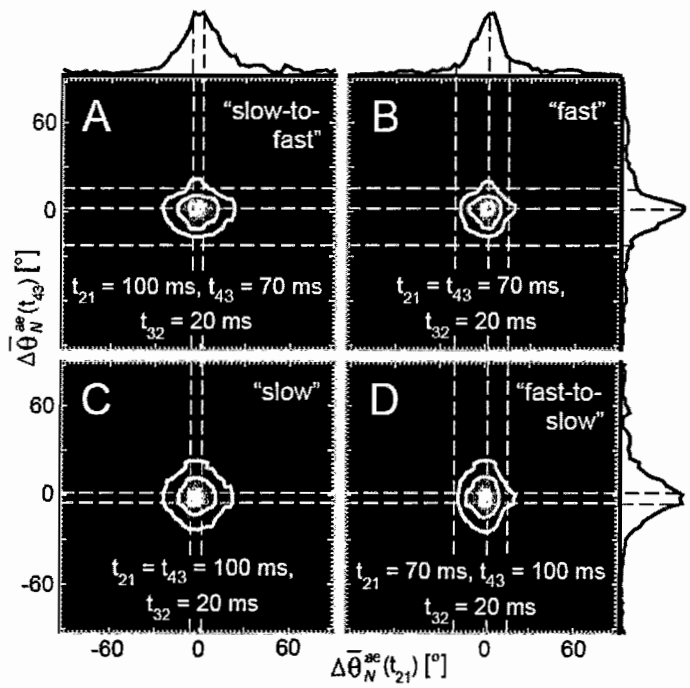

Figure 4.4. (A – D) Joint distributions of the sampled mean displacements of depolarization angles $P^{(4)}\left[\Delta\bar{\theta}_N^{ae}(t_{43}); \Delta\bar{\theta}_N^{ae}(t_{21})\right]$, where the waiting period $t_{32} = 20$ ms, and t_{21}, $t_{43} \in \{70\text{ ms}, 100\text{ ms}\}$, as shown. Selected features in the joint distributions (indicated by horizontal and vertical dashed gray lines) reflect temporally correlated transitions that participate in "fast" (~ 70 ms) and "slow" (~ 100 ms) conformational transition pathways. The magnitudes of the distributions are projected onto horizontal and vertical axes. Contours are shown at 0.9, 0.5, and 0.25 times the peak height.

$(+2^\circ, +2^\circ)$, $(+16^\circ, +16^\circ)$, $(+2^\circ, +16^\circ)$, $(+2^\circ, -22^\circ)$, $(+16^\circ, +2^\circ)$ and $(-22^\circ, +2^\circ)$.

These peaks indicate correlated events, in which a change in molecular conformation of a given magnitude is temporally correlated to that of another. The diagonal symmetry of

the "fast" and "slow" DFs suggests that for the relatively short waiting period of t_{32} = 20 ms, there is no temporal bias to indicate which of the two correlated events precedes the other.

The above results suggest that there are two significant optical conformation pathways in DsRed; (i) a "slow" pathway connecting at least two sequential steps, which involve the angular displacements $\Delta\bar{\theta}_N^{ae}$ = +2° and –6°; and (ii) a "fast" pathway connecting at least three sequential steps, which involve the displacements $\Delta\bar{\theta}_N^{ae}$ = +2°, +16°, and –22°. As discussed above, the coordinate pairings given by the joint DFs indicate the adjacencies between sequential steps in a given pathway. For example, the "fast" pathway appears to contain adjacent conformational transitions with $\Delta\bar{\theta}_N^{ae}$ = –22° and +2°, since the points $(+2^\circ, -22^\circ)$ and $(-22^\circ, +2^\circ)$ are present in the joint DF shown in Figure 4.4B. On the other hand, the "fast" pathway does not contain adjacent transitions with $\Delta\bar{\theta}_N^{ae}$ = –22° and +16°, because the joint distribution has no significant magnitude at the points $(+16^\circ, -22^\circ)$ and $(-22^\circ, +16^\circ)$. The distributions representing off-diagonal features in the spectral density (Figures 4.4A and 4.4D) contain information about exchange processes between the fast and slow pathways. For the distribution representing "slow-to-fast" exchange (Figure 4.4A), features are present at the coordinates $(+2^\circ, +2^\circ)$, $(+2^\circ, +16^\circ)$, $(+2^\circ, -22^\circ)$, $(-6^\circ, +2^\circ)$, $(-6^\circ, -22^\circ)$ and $(-6^\circ, +16^\circ)$. For the distribution representing "fast-to-slow" exchange (Figure 4.4D),

features are present at the coordinates $(+2^{\circ}, +2^{\circ})$, $(+2^{\circ}, -6^{\circ})$, $(+16^{\circ}, +2^{\circ})$, $(+16^{\circ}, -6^{\circ})$, $(-22^{\circ}, +2^{\circ})$ and $(-22^{\circ}, -6^{\circ})$. Features present in the exchange distributions indicate bridging steps between "fast" and "slow" kinetic pathways.

Information about the time scale for exchange between "fast" and "slow" kinetic pathways is obtained from the t_{32}-dependence of the 2D spectrum. In Figure 4.5A is shown the logarithm of $\left|S_A^{(4)}(\nu_{21}, t_{32}, \nu_{43})\right|$ for sequentially increasing values of the waiting period: t_{32} = 200 ms, 2 s, 5 s and 10 s. As the value of t_{32} is increased, the spectral density broadens in the transverse (off-diagonal) direction on the time scale of a few seconds. This transverse broadening indicates that sub-populations of molecules in the "fast" pathway undergo exchange with molecular populations in the "slow" pathway. The average time scale for the exchange is roughly the same as the τ_A = 8 s relaxation time for the anisotropy two-point TCF, reported in chapter II. Nevertheless, the behavior of the joint DFs indicates that the elementary steps of the exchange processes occur on sub-second time scales. In Figure 4.5B, are shown two sets of the joint distributions, corresponding to t_{32} = 2 s and 5 s. These DFs exhibit features at the same coordinates as those observed for the t_{32} = 20 ms DFs (indicated by dashed lines). As the waiting period is increased, there is a gradual loss of diagonal symmetry for "fast" and "slow" DFs (sub-panels B and C, respectively), such that they broaden in the direction of the vertical axis. As discussed further below, this loss of diagonal symmetry corresponds to the introduction of a temporal bias that indicates which of the two correlated transitions

precedes the other. Furthermore, the loss of diagonal symmetry suggests a tendency for molecular population to flow from "fast" to the "slow" pathways during the waiting period.

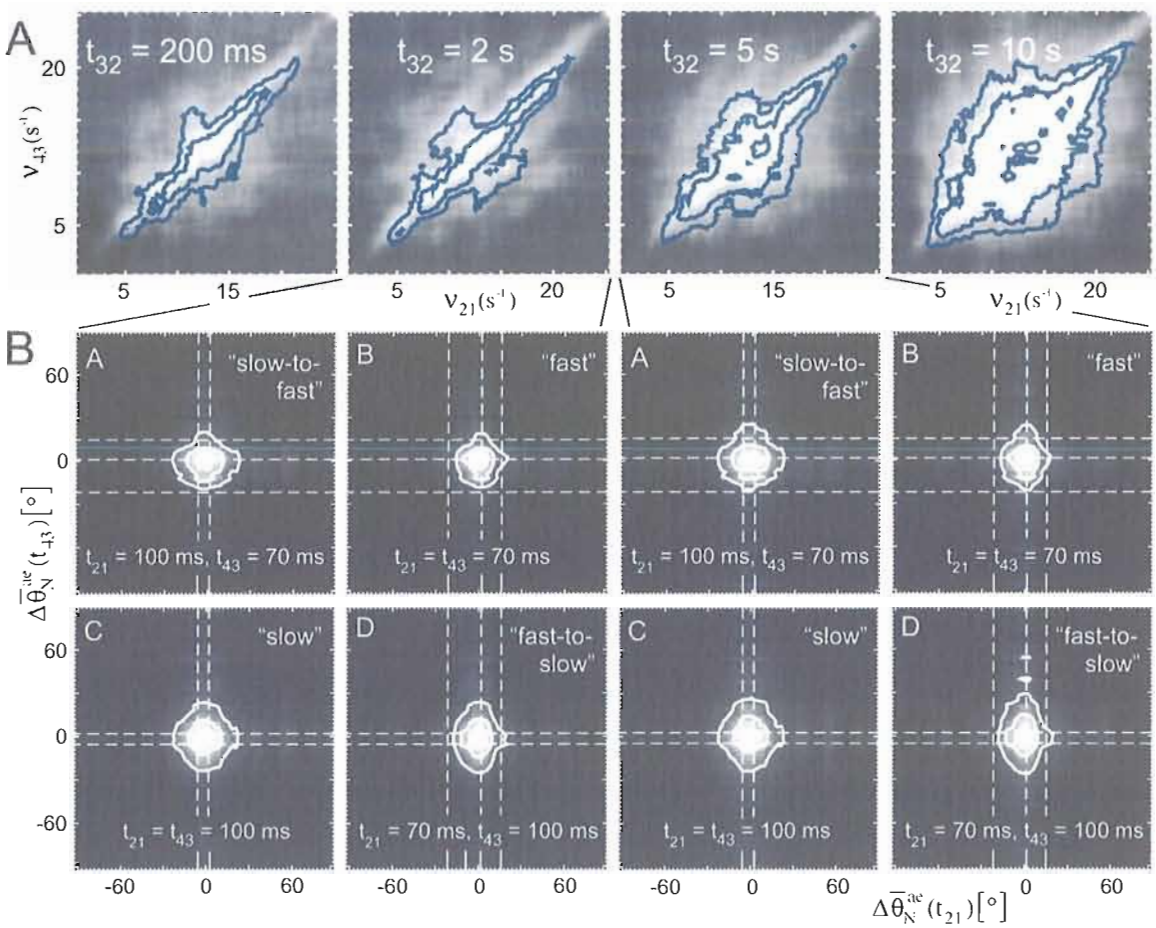

Figure 4.5. (A) Logarithm of the two-dimensional spectral density of the sampled mean depolarization angles $\left|S_A^{(4)}(\nu_{21},t_{32},\nu_{43})\right|$, for t_{32} = 200 ms, 2 s, 5 s, and 10s. The transverse broadening indicates that the average exchange time scale of the anisotropy fluctuations is approximately the same as the mean relaxation time τ_A = 8 s. (B) Joint distributions $P^{(4)}\left[\Delta\bar{\theta}_N^{ae}(t_{43});\Delta\bar{\theta}_N^{ae}(t_{21})\right]$, with t_{32} = 2 s and 5 s.

Conclusions

Millisecond conformational dynamics of freely diffusing DsRed was studied using a four-point analysis of PM-FICS trajectories. The 2D spectrum of conformational transitions, $\left|S_A^{(4)}(\nu_{21},t_{32},\nu_{43})\right|$, is roughly partitioned into "fast" and "slow" kinetic pathways. The slow anisotropy relaxation time $\tau_A = 8$ s is characteristic of exchange between "fast" and "slow" molecular sub-populations. Detailed information about the pathways connecting adjacent conformational transitions is contained by the joint distributions, $P^{(4)}\left[\Delta\bar{\theta}_N^{ae}(t_{43});\Delta\bar{\theta}_N^{ae}(t_{21})\right]$. For waiting periods much shorter than the exchange time ($t_{32} \ll \tau_A$), there is a clear separation between molecular sub-populations participating in each of the two pathways. For the "fast" sub-population, the angular displacements $\Delta\bar{\theta}^{ae} = +2^\circ$, $+16^\circ$, and -22° are observed, with adjacent pairings $+2^\circ \leftrightarrow +16^\circ$ and $+2^\circ \leftrightarrow -22^\circ$. For the "slow" sub-population, the paired displacements $\Delta\bar{\theta}^{ae} = +2^\circ$ and -6° are observed.

Our results can be combined with the model presented in Figure 4.1 for the possible depolarization angles of DsRed optical conformations. We propose the mechanism illustrated in Figure 4.6 to partially account for our observations of the conformational transition pathways. The system is assumed to be at equilibrium, with average steady-state concentrations of species maintained by balanced differential rates

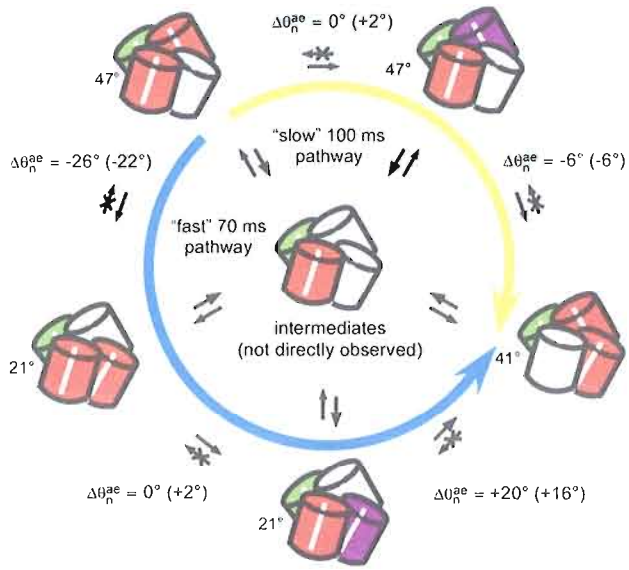

Figure 4.6. Possible model for the conformational transition pathways observed in DsRed. The structural and color conventions are the same as adopted in Figure 4.1, except that the "far-red" chromophore state is indicated by purple shading. The measured displacements in the depolarization angle are shown in parentheses next to the expected values from the crystallographic data. The molecule undergoes temporally correlated (cooperative) transitions between different optically coupled conformations. There are distinct "fast" and "slow" transition pathways, operating on the 70 and 100 ms time scales, respectively (indicated by the blue and gold arrows). Intermediates lacking dipolar coupling, such as the one generically depicted at the center of the diagram, connects adjacent species. Exchange processes involve correlations between transitions that occur on separate pathways, and occur on the mean time scale of 8 s.

of inter-conversion. Based on the crystal structure of DsRed [7], three conformations are possible for which the coupled dipoles have relative orientations $\theta_n^{ae} = 47^\circ$, 41°, and 21° (see Figure 4.1). Spectral shifts at individual chromophore sites result in conformational transitions. The "fast" pathway, indicated by the blue arrow, consists of three temporally correlated steps: $-22^\circ \rightarrow +2^\circ \rightarrow +16^\circ$. The "slow" pathway, indicated by the gold arrow, consists of two temporally correlated steps: $+2^\circ \rightarrow -6^\circ$. For each step is indicated the observed (in parentheses) and the expected angular displacements accompanying the conversion between species. In both transition pathways, observations of the angular displacement $\Delta\bar{\theta}^{ae} = +2^\circ$ are assigned to conformational transitions in

which a red site is converted into a far-red site (purple). The similarities between optical properties of the red and far-red states likely correspond to a very small change in the transition dipole moment orientation. It is also hypothesized that intermediates lacking dipolar coupling, such as the one generically depicted at the center of the diagram, connects adjacent species. While there is a directional bias implied by the proposed mechanism, the time ordering of events is interchangeable. A conformational transition upstream in the pathway is correlated to an adjacent downstream transition. Nevertheless, for $t_{32} \ll \tau_A$, the time ordering of events is not established. That is, an upstream transition is as likely to occur before a downstream transition, as it is likely to occur after one. Features in the exchange distributions indicate correlations between transitions on separate pathways. Therefore, molecules participating in one reactive pathway can participate in the other pathway at a later time. For $t_{32} \ll \tau_A$, the exchange processes are symmetric; for each exchange process involving transfer of molecular population from the "fast" to the "slow" pathway, there is an equally weighted exchange process in the opposite direction.

As the waiting period is increased to values exceeding the mean relaxation time, the loss of diagonal symmetry of the "fast" and "slow" joint distributions $P^{(4)}\left[\Delta\bar{\theta}_N^{ae}(t_{43}); \Delta\bar{\theta}_N^{ae}(t_{21})\right]$ (see Figure 4.5B) indicates the introduction of temporal bias. For $t_{32} \geq \tau_A$, downstream transitions tend to occur with greater probability after the waiting period. Corresponding inverse processes, in which downstream events occur prior to upstream events, receive less weight. Furthermore, the broadening of the

exchange distributions occurs in an asymmetric manner. While the "fast-to-slow" distribution appears to elongate in the direction of the $\Delta\bar{\theta}_N^{ae}(t_{43})$ axis, the "slow-to-fast" distribution does so to a lesser extent. This indicates that exchange processes between "fast" and "slow" pathways are more heavily biased in the "fast-to-slow" direction.

In this work, we have demonstrated a new 2D optical approach to study the kinetics of equilibrium conformational transitions of biological macromolecules, over a wide range of time scales (10^{-3} – 10^{2} s). PM-FICS was applied to simultaneously monitor molecular center-of-mass and anisotropy fluctuations. When applied to the system of DsRed molecules undergoing free diffusion, the approach allowed us to isolate the effects of optical switching conformational transitions. The phase-selectivity of PM-FICS measurements enables the calculation of 2D distributions and spectral densities. Similar to established 2D spectroscopic methods, the 2D spectral density determined by PM-FICS is useful to decompose the kinetics of a dynamically heterogeneous system, such as DsRed, into its separate components. A unique feature of PM-FICS is its ability to determine joint probability distributions of coordinate displacements, which contain detailed information about the pathways connecting sequential conformational transitions.

The PM-FICS method shares common attributes with 2D optical spectroscopy, single-molecule spectroscopy, and fluorescence fluctuation spectroscopy. The detailed information provided by PM-FICS measurements should be useful to address broad ranging problems in the fields of protein and nucleic acid dynamics, as well as other areas

in complex systems. In the current work, the well-defined structure of the DsRed molecule made this an appealing candidate to demonstrate the potential of the approach. The ability to perform such measurements on proteins and nucleic acids of general interest, in solution and in cell compartments, could enable future studies of *in vivo* enzymatic function.

CHAPTER V

CONCLUSION

Innovations in fluorescence microscopy and methods making it possible to discreetly label subcellular components with fluorescent probes were major turning points in biology. As the aspiration to look deeper into the cell and unlock its myriad secrets pushes the frontier of new technology into unexpected directions, methods in fluorescence experimentation remain as one of the focal points where new techniques evolve and develop. This dissertation presents Fourier imaging correlation spectroscopy (FICS) and polarization-modulated FICS (PM-FICS) as fluorescence methods suitable for the study of microscopic subcellular compartments such as mitochondria and conformational switching in multi-chromophore complexes, respectively. In what follows are presented a summary of the findings in this dissertation and an outlook as to how FICS and PM-FICS may be further developed as tools to study biological phenomena.

Summary

At the center of any fluorescence spectroscopic endeavor is improving the ratio of signal to noise collected at the detector. By explicitly isolating a single Fourier component and exploiting the phase-selectivity of FICS, the observable dynamic range can be dramatically increased by several orders of magnitude over conventional direct imaging techniques (i.e. CCD microscopy). As a consequence to this improvement in the signal to noise, fast dynamics inaccessible to high speed cameras may be captured with FICS, and even slow dynamics benefit from the higher S/N ratio since lower excitation intensities minimize photobleaching as well as reduce the production of photoreactive radicals within the cell. In addition to its application as a method for studying translational dynamics, FICS was modified to include a polarization grating in PM-FICS for the purpose of studying the internal conformational dynamics of larger multi-chromophore molecules.

The FICS experiments on the dynamics of mitochondria in yeast cells were a natural extension of the FICS work conducted in human osteosarcoma cells. The purpose of both sets of experiments was to establish the relationship of mitochondrial dynamics to the cytoskeleton. Because of their genetic pliability, yeast cells were a logical choice as a model organism for the continuing project on mitochondria. When FICS derived mean square displacements of mitochondria in cytoskeletal mutant cells are compared to wild-type cells, a strong dependence of yeast mitochondrial dynamics on the organization and function of the actin cytoskeleton is observed. This work demonstrated the successful

implementation of FICS to study how a subtle cytoskeletal mutation affects intracellular dynamics.

Modification of FICS to include a polarization grating led to the development of PM-FICS and a window into the internal dynamics of single molecules. Because the PM-FICS signal of single molecules may be separated into terms that result from their collective translational displacements and fluctuations in their optical anisotropies, PM-FICS experiments on DsRed were able to resolve time-dependent switching between different Forster resonance energy transfer pairs. The strong agreement between changes to the mean optical anisotropy of DsRed and crystallography data on the angular tilt of its putative energy transfer pairs prompted the construction of a basic model to account for observations in this time-dependent behavior. Analysis of the PM-FICS data on DsRed was completed with higher order, 4-point correlation functions and by sampling the corresponding mean dipole orientation angle signal to generate probability distributions. These 2D optical tools proved to be critical to our findings on the optical conformation changes of DsRed.

Outlook

FICS and PM-FICS are very promising tools for the contemporary biologist seeking to gain a microscopic understanding of intracellular function. These two methods were developed to contend with the rising challenge of collecting sufficient signal from small samples without sacrificing dynamic range, perturbing the microscopic

environment by introducing photoreactive radicals or relying extensively on models to interpret the data. Whilst the PM-FICS experiment was performed on DsRed as an *in vitro* experiment, the success of FICS with yeast cells holds the promise that future work on single molecules in the cellular environment can be achieved.

For the time being there are still numerous questions that remain unanswered in the study of mitochondrial dynamics and the cytoskeleton. Further FICS experiments with myosin mutants could test the argument that actin polymerization is the only major factor contributing to yeast mitochondrial motility. Moreover, one could envision FICS as a sensitive screening tool to assess the relative effect of various mutations on the motility of not just the mitochondria but numerous other organelles in the eukaryotic cell. This broadened scope of study could identify which mutations might have a general impact on the dynamics of all intracellular compartments and which ones promote a specific influence.

As an ultimate goal, it would be very satisfying to see PM-FICS developed as a tool for intracellular *in vivo* work; however, its advantages also make it particularly suitable for *in vitro* research. Since PM-FICS is able to follow dynamics arising from relative position changes in energy transfer pairs, the study of molecular conformation fluctuations can be made accessible through the covalent attachment of fluorescent probes. The changes in the anisotropy component of a PM-FICS signal in such an experiment would then be attributed to the conformational changes in the tagged molecule. An example of a prominent area in biological research well suited to this application would be the interaction dynamics of DNA and its associated proteins.

Depending on the placement of the two fluorescent probes, dynamics between different conformational states of the DNA when bound or not bound by protein could be studied in this manner.

FICS and PM-FICS have been tested and established as tools to investigate various microscopic systems in biological and non-biological contexts. As the study of the cell develops to a scrutiny of smaller components and fluorescence measurements become arduous as the signal to noise levels drop to lower and lower levels, FICS and PM-FICS offer a new sub-ensemble approach to assay the complex translational and conformational dynamics of intracellular components.

BIBLIOGRAPHY

Chapter I

1. Grassman, T.J., M.K. Knowles, and A.H. Marcus, *Structure and dynamics of fluorescently labeled complex fluids by fourier imaging correlation spectroscopy.* Phys Rev E Stat Phys Plasmas Fluids Relat Interdiscip Topics, 2000. **62**(6 Pt B): p. 8245-57.

2. Dixit, R. and R. Cyr, *Cell damage and reactive oxygen species production induced by fluorescence microscopy: effect on mitosis and guidelines for non-invasive fluorescence microscopy.* Plant J, 2003. **36**(2): p. 280-90.

3. Hopt, A. and E. Neher, *Highly nonlinear photodamage in two-photon fluorescence microscopy.* Biophys J, 2001. **80**(4): p. 2029-36.

4. Berland, K.M., *Fluorescence correlation spectroscopy: new methods for detecting molecular associations.* Biophys J, 1997. **72**(4): p. 1487-8.

5. Thompson, N.L., A.M. Lieto, and N.W. Allen, *Recent advances in fluorescence correlation spectroscopy.* Curr Opin Struct Biol, 2002. **12**(5): p. 634-41.

6. Bonsma, S., et al., *Green and red fluorescent proteins: photo- and thermally induced dynamics probed by site-selective spectroscopy and hole burning.* Chemphyschem, 2005. **6**(5): p. 838-49.

7. Hendrix, J., et al., *Dark states in monomeric red fluorescent proteins studied by fluorescence correlation and single molecule spectroscopy.* Biophys J, 2008.**94**(10): p. 4103-13.

8. Hansen, J.P. and I.R. McDonald, *Theory of Simple Liquids*. third ed. 2006, London: Academic Press.

9. Berne, B.J. and R. Pecora, *Dynamic Light Scattering: With Applications to Chemistry, Biology, and Physics*. 2000, Mineola: Dover.

10. Knowles, M.K., et al., *Cytoskeletal-assisted dynamics of the mitochondrial reticulum in living cells.* Proc Natl Acad Sci U S A, 2002. **99**(23): p. 14772-7.

11. Golding, I. and E.C. Cox, *Physical nature of bacterial cytoplasm.* Phys Rev Lett, 2006. **96**(9): p. 098102.

12. Tolic-Norrelykke, I.M., et al., Anomalous diffusion in living yeast cells. Phys Rev Lett, 2004. 93(7): p. 078102.

Chapter II

1. Weiss, S., *Measuring conformational dynamics of biomolecules by single molecule fluorescence spectroscopy.* Nat. Struct. Biol., 2000. **7**: p. 724-729.

2. Haustein, E., P. Schwille, *Single-molecule spectroscopic methods.* Curr. Opin. Struct. Biol., 2004. **14**: p. 531-540.

3. Fink, M.C., K. V. Adair, M. G. Guenza, A. H. Marcus, *Translational diffusion of fluorescent proteins by molecular Fourier imaging correlation spectroscopy.* Biophys. J. , 2006. **91**: p. 3482-3498.

4. Fink, M.C. and A.H. Marcus, *Simultaneous measurement of fluorescence anisotropy and translational fluctuations by polarization-modulated MFICS.* Philosophical Magazine, 2008. **88**: p. 3947-3951.

5. Knowles, M.K., et al., *Cytoskeletal-assisted dynamics of the mitochondrial reticulum in living cells.* Proc. Nat. Acad. Sci., 2002. **99**(23): p. 14772-14777.

6. Grassman, T.J., M.K. Knowles, and A.H. Marcus, *Structure and dynamics of fluorescently labeled complex fluids by Fourier imaging correlation spectroscopy.* Phys. Rev. E, 2000. **62**(6): p. 8245-8257.

7. Knowles, M.K., T.J. Grassman, and A.H. Marcus, *Measurement of the dynamic structure function of fluorescently labeled complex fluids by Fourier imaging correlation spectroscopy.* Phys. Rev. Lett., 2000. **85**(13): p. 2837-2840.

8. Knowles, M.K., A. R. Honerkamp-Smith, A. H. Marcus, *Direct measurement of relative and collective diffusion in a dilute binary colloidal suspension.* J. Chem. Phys., 2005. **122**: p. 234909-1-13.

9. Margineantu, D., R.A. Capaldi, and A.H. Marcus, *Dynamics of the mitochondrial reticulum in live cells using Fourier imaging correlation spectroscopy and digital video microscopy.* Biophys. J., 2000. **79**: p. 1833-1849.

10. Knowles, M.K., D. Margineantu, R. A. Capaldi, A. H. Marcus, *Translational dynamics of fluorescently labeled species by Fourier imaging correlation spectroscopy*, in *Liquid Dynamics: Experiment, Simulation and Theory*, J.T. Fourkas, Editor. 2002, American Chemical Society: Washington D. C. p. 58-70.

11. Nitzan, A., *Chemical Dynamics in Condensed Phases.* 2006, Oxford: Oxford University Press.

12. Cantor, C.R., P. R. Schimmel, *Biophysical Chemistry Part II: Techniques for the study of biological structure and function.* Biophysical Chemistry, ed. P.C. Vapnek. Vol. 2. 1980, New York: Freeman.

13. Lott, G.A., et al., *I. Conformational Dynamics of Biological Macromolecules by Polarization-Modulated Fourier Imaging Correlation Spectroscopy.* J Phys Chem B, 2009.

14. Berne, B.J., R. Pecora, *Dynamic Light Scattering.* 2000, Mineoloa, NY: Dover.

15. Margineantu, D., R. A. Capaldi, A. H. Marcus, *Dynamics of the mitochondrial reticulum in live cells using Fourier imaging correlation spectroscopy and digital video microscopy.* Biophys. J., 2000. **79**: p. 1833-1849.

16. Pringle, J.R., et al., *Immunofluorescence methods for yeast.* Methods Enzymol, 1991. **194**: p. 565-602.

17. Knowles, M.K., et al., *Cytoskeletal-assisted dynamics of the mitochondrial reticulum in living cells.* Proc Natl Acad Sci U S A, 2002. **99**(23): p. 14772-7.

18. Giepmans, B.N.G., S. R. Adams, M. H. Ellisman, R. Y. Tsien, *The fluorescent toolbox for assessing protein location and function.* Science, 2006. **312**: p. 217-224.

19. Field, S.F., M. Y. Bulina, I. V. Kelmanson, J. P. Bielawski, M. V. Matz, *Adaptive evolution of multicolored fluorescent proteins in reef-building corals.* J. Mol. Evol., 2006. **62**: p. 332-339.

20. Shaner, N.C., R. E. Campbell, P. A. Steinbach, B. N. G. Giepmans, A. E. Palmer, R. Y. Tsien, *Improved monomeric red, orange, and yellow fluorescent proteins derived from Discosoma sp. red fluorescent protein.* . Nat. Biotechnol., 2004. **22**: p. 1567-1572.

21. Wall, M.A., M. Socolich, R. Ranaganathan, *The structural basis for red fluorescence in the tetrameric GFP homolog DsRed.* Nat. Struct. Biol., 2000. **7**: p. 1133-1138.

22. Heikal, A.A., S. T. Hess, G. S. Baird, R. Y. Tsien, W. W. Webb, *Molecular spectroscopy and dynamics of intrinsically fluorescent proteins: coral red (dsRed) and yellow (Citrine).* Proc. Nat. Acad. Sci., 2000. **97**: p. 11996-12001.

23. Schenk, A., S. Ivanchenko, C. Rocker, J. Wiedenmann, and G. U. Nienhaus, *Photodynamics of red fluorescent proteins studied by fluorescence correlation spectroscopy.* Biophys. J., 2004. **86**: p. 384-394.

24. Malvezzi-Campeggi, F., M. Jahnz, K. G. Heinze, P. Dittrich, P. Schwille, *Light-induced flickering of DsRed provides evidence for distinct and interconvertible fluorescence states.* Biophys. J., 2001. **81**: p. 1776-1785.

25. Senning, E.N., et al., *II. Kinetic Pathways of Switching Optical Conformations in DsRed by 2D Fourier Imaging Correlation Spectroscopy.* J Phys Chem B, 2009. **113**(19): p. 6854-60.

Chapter III

1. van Zanten, J.H., K. P. Rufener, *Brownian motion in a single relaxation time Maxwell fluid.* Phys. Rev. E, 2000. **62**(4): p. 5389-5396.

2. Caspi, A., R. Granek, M. Elbaum, *Diffusion and directed motions in cellular transport.* Phys. Rev. E, 2002. **66**: p. 011916.

3. Golding, I. and E.C. Cox, *Physical nature of bacterial cytoplasm.* Phys Rev Lett, 2006. **96**(9): p. 098102.

4. Tolic-Norrelykke, I.M., et al., *Anomalous diffusion in living yeast cells.* Phys Rev Lett, 2004. **93**(7): p. 078102.

5. Cluzel, P., M. Surette, and S. Leibler, *An ultrasensitive bacterial motor revealed by monitoring signaling proteins in single cells.* Science, 2000. **287**(5458): p. 1652-5.

6. Elf, J., G.W. Li, and X.S. Xie, *Probing transcription factor dynamics at the single-molecule level in a living cell.* Science, 2007. **316**(5828): p. 1191-4.

7. Elowitz, M.B., et al., *Protein mobility in the cytoplasm of Escherichia coli.* J Bacteriol, 1999. **181**(1): p. 197-203.

8. Banks, D.S. and C. Fradin, *Anomalous diffusion of proteins due to molecular crowding.* Biophys J, 2005. **89**(5): p. 2960-71.

9. Mizuno, D.C.T., C. F. Schmidt, F. C. MacKintosh, *Nonequilibrium mechanics of active cytoskeletal networks.* Science, 2007. **315**: p. 370-373.

10. Pollard, T.D., G. G. Borisy, *Cellular motility driven by assembly and disassembly of actin filaments.* Cell, 2003. **112**: p. 453-465.

11. Ponka, P., *Tissue-specific regulation of iron metabolism and heme synthesis: distinct control mechanisms in erythroid cells.* Blood, 1997. **89**(1): p. 1-25.

12. Witkowski, A., A.K. Joshi, and S. Smith, *Coupling of the de novo fatty acid biosynthesis and lipoylation pathways in mammalian mitochondria.* J Biol Chem, 2007. **282**(19): p. 14178-85.

13. Green, D.R. and J.C. Reed, *Mitochondria and apoptosis.* Science, 1998. **281**(5381): p. 1309-12.

14. Bereiter-Hahn, J. and M. Voth, *Dynamics of mitochondria in living cells: shape changes, dislocations, fusion, and fission of mitochondria.* Microsc Res Tech, 1994. **27**(3): p. 198-219.

15. Margineantu, D., R. A. Capaldi, A. H. Marcus, *Dynamics of the mitochondrial reticulum in live cells using Fourier imaging correlation spectroscopy and digital video microscopy.* Biophys. J., 2000. **79**: p. 1833-1849.

16. Knowles, M.K., et al., *Cytoskeletal-assisted dynamics of the mitochondrial reticulum in living cells.* Proc Natl Acad Sci U S A, 2002. **99**(23): p. 14772-7.

17. Hollenbeck, P.J. and W.M. Saxton, *The axonal transport of mitochondria.* J Cell Sci, 2005. **118**(Pt 23): p. 5411-9.

18. Nunnari, J., et al., *Mitochondrial transmission during mating in Saccharomyces cerevisiae is determined by mitochondrial fusion and fission and the intramitochondrial segregation of mitochondrial DNA.* Mol Biol Cell, 1997. **8**(7): p. 1233-42.

19. Yaffe, M.P., *The machinery of mitochondrial inheritance and behavior.* Science, 1999. **283**(5407): p. 1493-7.

20. Huffaker, T.C., J.H. Thomas, and D. Botstein, *Diverse effects of beta-tubulin mutations on microtubule formation and function.* J Cell Biol, 1988. **106**(6): p. 1997-2010.

21. Jacobs, C.W., et al., *Functions of microtubules in the Saccharomyces cerevisiae cell cycle.* J Cell Biol, 1988. **107**(4): p. 1409-26.

22. Simon, V.R., T.C. Swayne, and L.A. Pon, *Actin-dependent mitochondrial motility in mitotic yeast and cell-free systems: identification of a motor activity on the mitochondrial surface.* J Cell Biol, 1995. **130**(2): p. 345-54.

23. Boldogh, I.R., et al., *Arp2/3 complex and actin dynamics are required for actin-based mitochondrial motility in yeast.* Proc Natl Acad Sci U S A, 2001. **98**(6): p. 3162-7.

24. Boldogh, I.R., et al., *A type V myosin (Myo2p) and a Rab-like G-protein (Ypt11p) are required for retention of newly inherited mitochondria in yeast cells during cell division.* Mol Biol Cell, 2004. **15**(9): p. 3994-4002.

25. Grassman, T.J., M.K. Knowles, and A.H. Marcus, *Structure and dynamics of fluorescently labeled complex fluids by fourier imaging correlation spectroscopy.* Phys Rev E Stat Phys Plasmas Fluids Relat Interdiscip Topics, 2000. **62**(6 Pt B): p. 8245-57.

26. Knowles, M.K., T. J. Grassman, A. H. Marcus, *Measurement of the dynamics structure function of fluorescently labeled complex fluids by Fourier imaging correlation spectroscopy.* Phys. Rev. Lett., 2000. **85**: p. 2837-2840.

27. Xu, J., V. Viasnoff, D. Wurtz, *Compliance of actin filament networks measured by particle-tracking micorheology and diffusing wave spectroscopy.* Rheol. Acta, 1998. **37**: p. 387-398.

28. Wen, K.K. and P.A. Rubenstein, *Acceleration of yeast actin polymerization by yeast Arp2/3 complex does not require an Arp2/3-activating protein.* J Biol Chem, 2005. **280**(25): p. 24168-74.

29. Pantaloni, D., C. Le Clainche, M.-F. Carlier, *Mechanism of actin-based motility.* Science, 2001. **292**: p. 1502-1506.

30. Winter, D.C., E.Y. Choe, and R. Li, *Genetic dissection of the budding yeast Arp2/3 complex: a comparison of the in vivo and structural roles of individual subunits.* Proc Natl Acad Sci U S A, 1999. **96**(13): p. 7288-93.

31. Apgar, J., et al., *Multiple-particle tracking measurements of heterogeneities in solutions of actin filaments and actin bundles.* Biophys J, 2000. **79**(2): p. 1095-106.

32. Sprakel, J., et al., *Brownian particles in transient polymer networks.* Phys Rev E Stat Nonlin Soft Matter Phys, 2008. **77**(6 Pt 1): p. 061502.

33. Chen, D.T., et al., *Rheological microscopy: local mechanical properties from microrheology.* Phys Rev Lett, 2003. **90**(10): p. 108301.

34. Levine, A.J. and T.C. Lubensky, *Two-point microrheology and the electrostatic analogy.* Phys Rev E Stat Nonlin Soft Matter Phys, 2002. **65**(1 Pt 1): p. 011501.

35. van der Gucht, J., et al., *Brownian particles in supramolecular polymer solutions.* Phys Rev E Stat Nonlin Soft Matter Phys, 2003. **67**(5 Pt 1): p. 051106.

36. Belmont, L.D., et al., *A change in actin conformation associated with filament instability after Pi release.* Proc Natl Acad Sci U S A, 1999. **96**(1): p. 29-34.

37. Pringle, J.R., et al., *Immunofluorescence methods for yeast.* Methods Enzymol, 1991. **194**: p. 565-602.

Chapter IV

1. Frauenfelder, H., S. G. Sligar, P. G. Wolynes, *The energy landscapes and motions of proteins*. Science, 1991. **254**: p. 1598-1603.

2. Miyashita, O., J. N. Onuchic, P. G. Wolynes, *Nonlinear elasticity, proteinquakes, and the energy landscapes of functional transitions in proteins*. Proc. Nat. Acad. Sci., 2003. **100**: p. 12570-12575.

3. Henzler-Wildman, K.A., M. Lei, V. Thai, S. J. Kerns, M. Karplus, D. Kern, *A heirarchy of timescales in protein dynamics is linked to enzyme catalysis*. Nature, 2007. **450**: p. 913-918.

4. Boehr, D.B., H. J. Dyson, P. E. Wright, *An NMR perspective on enzyme dynamics*. Chem. Rev., 2006. **106**: p. 3055-3079.

5. Hochstrasser, R.M., *Two-dimensional spectroscopy at the infrared and optical frequencies*. Proc. Nat. Acad. Sci., 2007. **104**: p. 14190-14196.

6. Shaner, N.C., R. E. Campbell, P. A. Steinbach, B. N. G. Giepmans, A. E. Palmer, R. Y. Tsien, *Improved monomeric red, orange, and yellow fluorescent proteins derived from Discosoma sp. red fluorescent protein*. . Nat. Biotechnol., 2004. **22**: p. 1567-1572.

7. Wall, M.A., M. Socolich, R. Ranaganathan, *The structural basis for red fluorescence in the tetrameric GFP homolog DsRed*. Nat. Struct. Biol., 2000. **7**: p. 1133-1138.

8. Gross, L.A., G. S. Baird, R. C. Hoffman, K. K. Baldridge, and R. Y. Tsien, *The structure of the chromophore within DsRed, a red fluorescent protein from coral*. Proc. Nat. Acad. Sci., 2000. **97**: p. 11990-11995.

9. Yarbrough, D., R. M. Wachter, K. Kallio, M. V. Matz, and S. J. Remington, *Refined crystal structure of DsRed, a red fluorescent protein from coral, at 2.0-A resolution*. Proc. Nat. Acad. Sci., 2001. **98**: p. 462-467.

10. Baird, G.S., D. A. Zacharias, and R. Y. Tsien, *Biochemistry, mutagenesis, and oligomerization of DsRed, a red fluorescent protein from coral*. Proc. Nat. Acad. Sci., 2000. **97**: p. 11984-11989.

11. Garcia-Parajo, M.F., M. Koopman, E. M. H. P. van Dijk, V. Subramaniam, N. F. van Hulst, *The nature of fluorescence emission in the red fluorescent protein DsRed, revealed by single-molecule detection*. Proc. Nat. Acad. Sci., 2001. **98**: p. 14392-14397.

12. Bonsma, S., J. Gallus, F. Konz, R. Purchase, S. Volker, *Light-induced conformational changes and energy transfer in red fluorescent protein*. J. Luminesc., 2004. **107**: p. 203-212.

13. Bonsma, S., R. Purchase, S. Jezowski, J. Gallus, F. Konz, S. Volker, *Green and red fluorescnt proteins: photo- and thermally induced dynamics probed by site-selective spectroscopy and hole burning*. ChemPhysChem, 2005. **6**: p. 838-849.

14. Heikal, A.A., S. T. Hess, G. S. Baird, R. Y. Tsien, W. W. Webb, *Molecular spectroscopy and dynamics of intrinsically fluorescent proteins: coral red (dsRed) and yellow (Citrine)*. Proc. Nat. Acad. Sci., 2000. **97**: p. 11996-12001.

15. Malvezzi-Campeggi, F., M. Jahnz, K. G. Heinze, P. Dittrich, P. Schwille, *Light-induced flickering of DsRed provides evidence for distinct and interconvertible fluorescence states*. Biophys. J., 2001. **81**: p. 1776-1785.

16. Schenk, A., S. Ivanchenko, C. Rocker, J. Wiedenmann, and G. U. Nienhaus, *Photodynamics of red fluorescent proteins studied by fluorescence correlation spectroscopy*. Biophys. J., 2004. **86**: p. 384-394.

17. Lounis, B., J. Deich, F. I. Rosell, S. G. Boxer, W. E. Moerner, *Photophysics of DsRed, a red fluorescent protein, from the ensemble to the single-molecule level*. J. Phys. Chem. B, 2001. **105**: p. 5048-5054.

18. Hendrix, J., C. Flors, P. Dedecker, J. Hofkens, and Y. Engelborghs, *Dark states in moneric red fluorescent proteins studied by fluorescence correlation and single molecule spectroscopy* Biophys. J., 2008. **94**: p. 4103-4113.

19. Mukamel, S., *Principles of Nonlinear Optical Spectroscopy*. Oxford Series in Optical Imaging Sciences. 1995, Oxford: Oxford University Press.